

3D structures and dispersion in shallow fluid layers

Citation for published version (APA):

Akkermans, R. A. D. (2010). *3D structures and dispersion in shallow fluid layers*. [Phd Thesis 1 (Research TU/e / Graduation TU/e), Applied Physics and Science Education]. Technische Universiteit Eindhoven.
<https://doi.org/10.6100/IR675782>

DOI:

[10.6100/IR675782](https://doi.org/10.6100/IR675782)

Document status and date:

Published: 01/01/2010

Document Version:

Publisher's PDF, also known as Version of Record (includes final page, issue and volume numbers)

Please check the document version of this publication:

- A submitted manuscript is the version of the article upon submission and before peer-review. There can be important differences between the submitted version and the official published version of record. People interested in the research are advised to contact the author for the final version of the publication, or visit the DOI to the publisher's website.
- The final author version and the galley proof are versions of the publication after peer review.
- The final published version features the final layout of the paper including the volume, issue and page numbers.

[Link to publication](#)

General rights

Copyright and moral rights for the publications made accessible in the public portal are retained by the authors and/or other copyright owners and it is a condition of accessing publications that users recognise and abide by the legal requirements associated with these rights.

- Users may download and print one copy of any publication from the public portal for the purpose of private study or research.
- You may not further distribute the material or use it for any profit-making activity or commercial gain
- You may freely distribute the URL identifying the publication in the public portal.

If the publication is distributed under the terms of Article 25fa of the Dutch Copyright Act, indicated by the "Taverne" license above, please follow below link for the End User Agreement:

www.tue.nl/taverne

Take down policy

If you believe that this document breaches copyright please contact us at:

openaccess@tue.nl

providing details and we will investigate your claim.

3D STRUCTURES AND DISPERSION
IN SHALLOW FLUID LAYERS

Copyright © 2010 R.A.D. Akkermans
Printed by Gildeprint Drukkerijen – The Netherlands

A catalogue record is available from the Eindhoven University of
Technology Library

Akkermans, Rinie Adrianus Dejan

3D Structures and dispersion in shallow fluid layers / by Rinie Adrianus
Dejan Akkermans. – Eindhoven: Technische Universiteit Eindhoven, 2010.
– Proefschrift.

ISBN 978-90-386-2283-5

NUR 926

Trefwoorden: ondiepe stromingen / dipolaire wervels / quasi-twee-dimensionale
turbulentie / laboratorium experimenten / directe numerieke simulaties

Subject headings: shallow flows / dipolar vortices / quasi-two-dimensional
turbulence / laboratory experiments / direct numerical simulations

3D STRUCTURES AND DISPERSION
IN SHALLOW FLUID LAYERS

PROEFSCHRIFT

ter verkrijging van de graad van doctor aan de
Technische Universiteit Eindhoven, op gezag van de
rector magnificus, prof.dr.ir. C.J. van Duijn, voor een
commissie aangewezen door het College voor
Promoties in het openbaar te verdedigen
op maandag 28 juni 2010 om 16.00 uur

door

Rinie Adrianus Dejan Akkermans

geboren te Etten-Leur

Dit proefschrift is goedgekeurd door de promotoren:

prof.dr.ir. G.J.F. van Heijst

en

prof.dr. H.J.H. Clercx

Copromotor:

dr.ir. L.P.J. Kamp

This work is part of the research programme no. 36 “Two-Dimensional Turbulence” of the “Stichting voor Fundamenteel Onderzoek der Materie (FOM)”, which is financially supported by the “Nederlandse Organisatie voor Wetenschappelijk Onderzoek (NWO)”.



Посвећено Божини Дошљак

Contents

1	Introduction	1
1.1	Two-dimensional turbulence	2
1.1.1	From three to two spatial dimensions	2
1.1.2	Numerical simulations of 2D turbulence	6
1.2	Experimental realisations of 2D turbulence	8
1.2.1	General overview of experiments in thin fluid layers	8
1.2.2	Electromagnetically-driven shallow fluid layers	9
1.2.3	Three-dimensionality in shallow-fluid experiments	11
1.3	Aim and outline of this thesis	12
2	Experimental and numerical techniques	15
2.1	Measurement technique	15
2.1.1	Introduction	15
2.1.2	Particle image velocimetry	18
2.1.3	Stereoscopic particle image velocimetry	19
2.2	Experimental setup	24
2.2.1	Dipolar vortex in a single-fluid layer	25
2.2.2	Dipole in a two-layer fluid	27
2.2.3	Linear array of vortices	29
2.3	Numerical method	32
2.3.1	Numerical setup single-layer dipole	32
2.3.2	Numerical settings two-layer simulations	35
2.3.3	Numerical setup line of vortices	37
2.3.4	Passive tracer transport	39
3	The dipolar vortex in a shallow fluid layer	41
3.1	Introduction	42
3.2	Details of experiments and simulations	44

3.3	Experimental and numerical results	45
3.3.1	The generation and evolution of the dipolar vortex	45
3.3.2	The structure of the dipole: stagnation points and horizontal vorticity rolls	53
3.3.3	Alternative initial and boundary conditions	56
3.3.4	Quantifying two-dimensionality of the shallow flow	60
3.4	Conclusions and Discussion	67
4	The dipole in two-layer fluids	69
4.1	Introduction	70
4.2	Details of experiments and simulations	71
4.3	Experimental and numerical results	72
4.3.1	The 3D flow evolution of a dipole in a two-layer fluid	73
4.3.2	Development of the frontal circulation	76
4.3.3	The 3D structure of the dipole with decreasing upper fluid layer depth	78
4.3.4	Degree of two-dimensionality of shallow dipoles	81
4.3.5	Tracer transport at the free surface	84
4.4	Conclusions and Discussion	85
5	Linear array of vortices	87
5.1	Introduction	88
5.2	Details of laboratory experiments and numerical simulations	89
5.3	Flow structure of the linear array of vortices	91
5.3.1	Weak forcing without wall: Case I	91
5.3.2	Strong forcing without wall: Case III	95
5.3.3	Strong forcing with wall: Case IIIw	100
5.3.4	Influence of the lateral wall: averaged kinetic energy	104
5.3.5	Degree of two-dimensionality for the linear array of vortices	106
5.4	Tracer transport by a linear array of vortices	108
5.4.1	Dispersion at low Reynolds number; case I	108
5.4.2	Influence of 3D motion; case III	109
5.4.3	Influence of the lateral wall; case IIIw	114
5.5	Conclusions	120
6	Conclusions	123
A	Experiments on linear array of vortices	129

Bibliography	135
Summary	145
Samenvatting	147
Promotiecommissie	149
Dankwoord	151
Curriculum vitae	153

CHAPTER 1

Introduction

Often, when reducing the number of spatial dimensions in a dynamical system the involved mathematics is reduced while preserving the qualitative dynamical behaviour of the system. In turbulence, this is not the case. In three-dimensional (3D) turbulence energy tends to be (on average) transferred to smaller scales, where the kinetic energy is then removed by viscous dissipation at the smallest scales of the flow. This break-up of large-scale structures into smaller and smaller ones was first suggested by Richardson, and is now known as the energy cascade (see, e.g., [50]). In two-dimensional (2D) turbulence the opposite is observed: the energy is transferred from the injection scale towards the larger scales, i.e., formation of larger structures is expected. The phenomenology of 2D turbulence is therefore strikingly different than its 3D counterpart.

There are several mechanisms that promote 2D behaviour of fluid motion, such as background rotation, density stratification, or geometrical confinement. Rotation promotes two-dimensional flow, in the sense that the velocity must be independent of the direction parallel to the background rotation (Taylor-Proudman theorem). Density stratification introduces a stabilising effect that promotes horizontal, so-called pancake-like structures. Geometrical confinement suppresses motion in one spatial dimension. As a consequence, the fluid motion is predominantly planar. Examples of situations where all of these three effects are simultaneously present are the Earth's atmosphere and oceans.

This introductory chapter begins with the background of 2D turbulence

and introduces briefly some theoretical results of 2D turbulence. Numerical simulations aimed at validating theoretical results on 2D turbulence are discussed. Hereafter, laboratory studies on 2D or quasi-2D turbulence are presented with particular attention to experiments utilising geometrical confinement. Finally, the aim of this thesis is formulated and an outline is given.

1.1 Two-dimensional turbulence

In this subsection a concise introduction to some theoretical descriptions on 2D turbulence are given, together with a brief overview of numerical studies on turbulence in two-dimensions.

1.1.1 From three to two spatial dimensions

Most flows in nature are three-dimensional and turbulent. The evolution of an incompressible, homogeneous fluid is described by the Navier-Stokes equation for Newtonian fluids [50], i.e.,

$$\frac{\partial \mathbf{v}}{\partial t} + (\mathbf{v} \cdot \nabla) \mathbf{v} = -\frac{1}{\rho} \nabla p + \nu \nabla^2 \mathbf{v} + \frac{1}{\rho} \mathbf{f}, \quad (1.1)$$

and

$$\nabla \cdot \mathbf{v} = 0, \quad (1.2)$$

where \mathbf{v} is the 3D velocity vector, p the pressure, ν the viscosity, ρ is the mass density, and \mathbf{f} any external body force. For the time being, an infinite domain is considered. Later this assumption is reconsidered.

An indication of the complexity of the flow is given by the Reynolds number defined as $\text{Re} = \mathcal{U}\mathcal{L}/\nu$, where \mathcal{U} and \mathcal{L} are a typical velocity and length scale, respectively. The Reynolds number is a measure of the relative importance of advection to viscous dissipation. For low Reynolds numbers [$\text{Re}=\mathcal{O}(1)$] the flow is dominated by viscous effects, i.e., the fluid motion is laminar. When increasing the Reynolds number the flow becomes more complex and eventually the fluid motion exhibits an unpredictable, turbulent nature. This turbulent state is characterized by the presence of a large range of length and time scales.

An important result on 3D turbulence was derived by Kolmogorov in

1941 regarding the scaling of the inertial range (see, e.g., [33]). He assumed that the energy spectrum in the inertial range is determined by the rate of energy transfer and the wavenumber k . The energy transfer rate is the change in time of the total kinetic energy E (equal to $\frac{1}{2} \int_{\mathcal{D}} \mathbf{v}^2 dA$). The wavenumber is proportional to the inverse of the length scale ℓ , i.e., $k \sim \ell^{-1}$. Kolmogorov assumed that in 3D turbulence the constant spectral energy flux is balanced by the dissipation rate of kinetic energy per unit mass ϵ . On dimensional grounds it can easily be shown that this implies

$$E(k) = C_0 \epsilon^{2/3} k^{-5/3} \quad \text{for } k_f < k < k_d, \quad (1.3)$$

where C_0 is the Kolmogorov constant, k_f the forcing wavenumber, and k_d the dissipation wavenumber. The range for which this scaling holds is called the inertial range. This five-thirds law is an important result of turbulence theory, and is illustrated in Fig. 1.1(a). Energy is injected at the forcing

a) b)

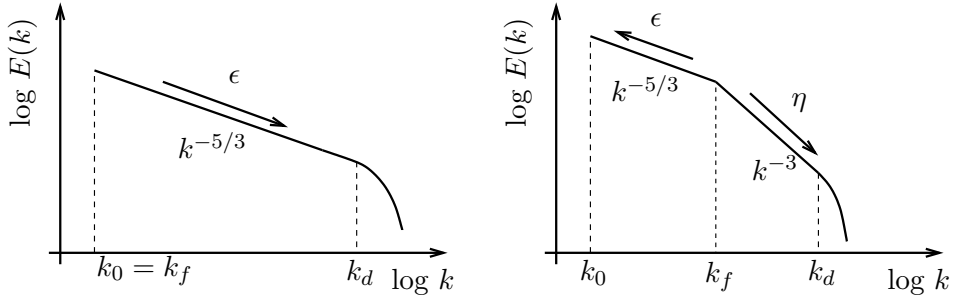


Figure 1.1 – (a) Schematic of the direct energy cascade in three-dimensional turbulence. Energy is injected at wavenumber k_f and subsequently transported at rate ϵ to larger wavenumbers, with k_d the dissipation wavenumber. (b) Dual cascade of energy and enstrophy in two-dimensional turbulence. The injected energy is transported to smaller wavenumbers and enstrophy is transported to larger wavenumbers at rate η , where it is eventually removed by viscous dissipation at wavenumber k_d .

wavenumber k_f and is transported to larger wave numbers (i.e., small length scales), where it is removed by viscous dissipation. A continuous feeding of energy is required to maintain the flow in a turbulent state. This inertial range scaling has been confirmed in many 3D turbulence experiments and numerical simulations (see, e.g., [33] and references therein).

The pronounced difference between 2D and 3D turbulence is most convincingly illustrated by considering the vorticity equation, where vorticity

$\boldsymbol{\omega}$ is defined as the curl of the velocity field (i.e., $\nabla \times \mathbf{v}$). Taking the curl of Eq. (1.1) and applying several vector identities, the 3D vorticity equation for barotropic flow follows:

$$\frac{\partial \boldsymbol{\omega}}{\partial t} + (\mathbf{v} \cdot \nabla) \boldsymbol{\omega} - (\boldsymbol{\omega} \cdot \nabla) \mathbf{v} = \nu \nabla^2 \boldsymbol{\omega} + \nabla \times \mathbf{f}. \quad (1.4)$$

The third term on the left-hand side represents the stretching and tilting of vorticity present in 3D flows. In 2D flows, the vorticity vector is normal to the plane of motion and can be represented by a scalar quantity, i.e., $\boldsymbol{\omega} = (0, 0, \omega)$. Then, by invoking the Taylor-Proudman theorem, the term representing stretching and tilting of vorticity is absent. This absence causes 2D turbulence to behave strikingly different from 3D turbulence.

In a similar way as Kolmogorov, Kraichnan [49] obtained the shape of the energy spectrum for 2D turbulence, based on the assumption that now both energy and enstrophy are conserved. If it is assumed that the energy and enstrophy are injected at a certain wavenumber k_f , an inverse energy cascade develops that transfers energy towards larger scales. In this inverse energy cascade it is assumed that the transfer of enstrophy is negligible. On dimensional grounds one derives

$$E(k) = C_2 \epsilon^{2/3} k^{-5/3} \quad \text{for } k < k_f, \quad (1.5)$$

where C_2 is the Kraichnan-Kolmogorov constant. At the same time, a direct cascade of enstrophy develops where the energy transfer is negligible and the spectrum can be scaled with the down-scale enstrophy transfer rate η

$$E(k) = C_3 \eta^{2/3} k^{-3} \quad \text{for } k_f < k < k_d, \quad (1.6)$$

where k_d represents the wavenumber that corresponds with the smallest scales of motion. A schematic of the dual-cascade picture in 2D turbulence is given in Fig. 1.1(b). The energy is transferred towards progressively larger scales or lower wavenumbers, whereas the enstrophy is characterised by a down-scale transfer to higher wavenumbers until viscous dissipation becomes dominant.

One striking difference between 3D turbulence and its 2D counterpart, is the formation and persistence of large-scale structures in the latter. This self-organisation can be explained with the schematic shown in Fig. 1.1. In 3D turbulent flows energy is injected and transported (by means of vortex stretching and tilting) to the small scales, where it is dissipated eventually. In 2D turbulence, the injected energy is transported to larger scales (small

wavenumbers) and the formation of larger structures is anticipated. Viscosity acts predominantly at the small scales, therefore these large-scale structures hardly experience dissipation and are able to persist for long times, i.e., many eddy turnover times. Actually, the formation of such large-scale structures was already predicted on theoretical grounds by Onsager [64] and Fjørtoft [30]. This self-organisation is illustrated in Fig. 1.2, showing numerically obtained vorticity snapshots of a 2D decaying turbulence simulation. The flow is initialised with 100 vortices on a regular grid, and hereafter

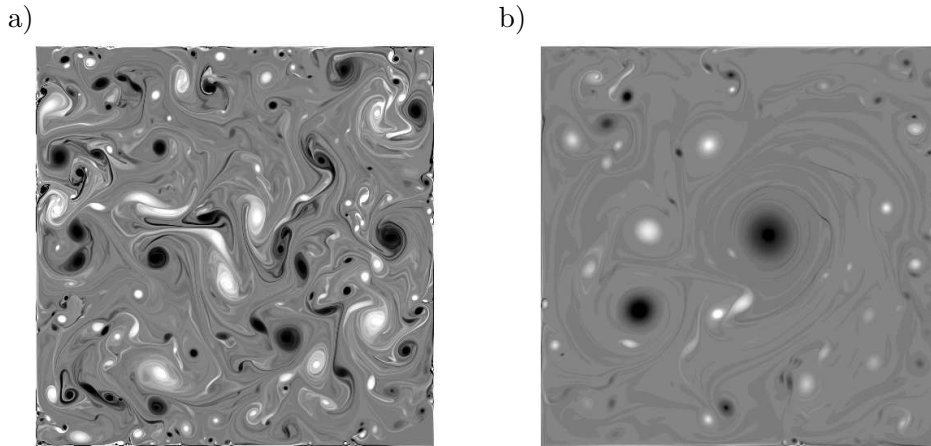


Figure 1.2 – Vorticity snapshots of a 2D turbulence simulation (a) just after onset of simulation and (b) after many turnover times showing self-organisation. White (black) corresponds to negative (positive) vorticity values. The flow is initialised with a 10×10 array of vortices at onset of the simulation. Courtesy of G.H. Keetels [44].

the flow is left to decay. In Fig. 1.2(a) many small vortices and vorticity filaments are observed at the early stage of the evolution. These vortices start to interact: formation of dipolar vortices which start to propagate and merging of like-signed vortices into larger ones are seen. Eventually, long after the onset of the simulation, large-scale structures can be appreciated resulting from this self-organisation process as depicted in Fig. 1.2(b).

For some reasons one might object to the term “2D turbulence”. This is particularly true when one considers vortex stretching and tilting as essential ingredients of turbulence. The energy cascade as described by Richardson, i.e., the break-up of large-scale structures into smaller and smaller ones, is driven by this vortex stretching and tilting process, which is an essentially 3D mechanism. Therefore, turbulence based on the mechanism

described above can thus not exist in two spatial dimensions. Next to this argument, we know that 2D flows do not exist in the real world. The concept of 2D turbulence gives nevertheless insight in situations where the growth of three-dimensional disturbances is prevented, such as in large-scale geophysical flows [55]. Figure 1.3 displays a satellite image of stratocumulus



Figure 1.3 – Satellite image of the formation of a von Kármán vortex street in the wake of Jan Mayen island on June 6, 2001. The mean flow direction is from left to right and is visualised by the clouds. Image is from NASA’s Earth Observatory and spans approximately 360 by 160 km.

clouds near an island (Jan Mayen island, 650 km northeast of Iceland). The flow (in the picture from left to right) is impeded by an obstacle, i.e., a volcano of 2.2 km height. In the wake of this island the formation of large-scale vortices is seen as visualised by the clouds, in the form of a so-called von Kármán vortex street. Of course, this is a situation where the rotation of the Earth, density stratification and geometrical confinement all play a role in two-dimensionalising the flow.

1.1.2 Numerical simulations of 2D turbulence

Numerical simulations have been used to test the scaling exponents of 2D turbulence as predicted by Kraichnan. A concise overview of these attempts follows, as well as the utilisation of periodic boundary conditions in Fourier spectral codes. For a recent and detailed review on 2D turbulence simulations, the reader is referred to Clercx and van Heijst [19].

The first direct numerical simulations of forced 2D turbulence were performed by Lilly [53] in 1969, aimed at confirming the existence of the dual-cascade picture predicted by Kraichnan [49]. These simulations were

performed with a Fourier spectral code on a square domain and periodic boundary conditions were employed. Although the resolution of these numerical simulation was rather low (i.e., consisting of just 64^2 grid points), the results did hint at the presence of the dual cascade.

Almost twenty years later, Frisch and Sulem [34] obtained a clear inertial range scaling of the inverse energy cascade with a resolution of 256^2 grid points. Later this scaling was confirmed by Smith and Yakhot [82], who increased the resolution even more, obtaining a clear scaling over 2 decades. Furthermore, they observed the formation of a large-scale structure similar to a Bose–Einstein condensate, as predicted by Kraichnan.

Only recently, Boffetta [7] reported on the simultaneous presence of the inverse energy and enstrophy cascades in forced 2D turbulence simulations. He also used a Fourier spectral code with periodic boundary conditions. This dual-cascade scenario is in agreement with the predictions by Kraichnan [49].

The use of Fourier spectral codes dictates the utilisation of periodic boundary conditions. Periodic boundary conditions mean that what flows out at one side, enters the domain at the opposite side (or vice versa). It was assumed that such a periodic domain represents, to some extent, the flow on an infinite domain (e.g., large-scale atmospheric flow of the Earth) where finite-size effects and the presence of boundaries are avoided. However, simulations on bounded 2D turbulence have revealed the influence of the (no-slip) domain boundaries on the flow evolution in both decaying and forced 2D turbulence [19, 93]. The 2D vortices interact with the no-slip wall, which leads to the formation of thin boundary layers that detach from the lateral wall and roll up to form small vortices containing high-amplitude vorticity. Another example of the influence of a lateral no-slip wall is the spontaneous spin-up of the flow which has been observed for decaying 2D turbulence confined to non-circular domains [95].

In 2D turbulence the injected energy is transported to the larger scales. Newtonian viscosity predominantly removes energy at the smallest scales of the flow. As a result of the inverse energy cascade the energy will thus pile-up at the length scale comparable to the domain size. Different forms of the dissipation have been proposed to provide an energy sink at the largest scale. Together with the usual Newtonian dissipation $\nu \nabla^2 \mathbf{v}$ a linear friction term is added to the 2D Navier-Stokes equations that is nonselective with respect to length scales. The physical motivation for the use of linear friction is that it represents a lowest order parameterisations of bottom

friction, which is inevitable in laboratory experiments.

1.2 Experimental realisations of 2D turbulence

Besides the numerically sought confirmation of the characteristics of 2D turbulence, corroboration has also been sought by laboratory experiments. These laboratory experiments can be categorised by the way in which two-dimensionality is enforced, i.e, background rotation, density stratification, or geometrical confinement. Often, these mechanisms are studied separately to investigate the individual effects on the two-dimensionality of the flow. In this section, mainly laboratory experiments where geometrical confinement is utilised to promote 2D flow behaviour are discussed. The shallow fluid layer setup, which is employed in the investigation reported in this thesis, fits in this framework.

1.2.1 General overview of experiments in thin fluid layers

One of the first experimental investigations on 2D turbulence was performed by Sommeria [84]. The setup he used was a thin layer of mercury, where besides the geometrical confinement, 3D motions were also suppressed by a sufficiently strong vertical magnetic field. This additional suppression of 3D motion can be characterised by the Hartmann number Ha which is a measure for the relative importance of magnetic to viscous forces. In such flows (i.e., with $Ha \gg 1$), the Lorentz force acts in a similar way as the Coriolis force in (strongly) rotating flows. In the experiments by Sommeria, an inverse energy cascade was found spanning about half a decade, as well as the formation of large-scale structures, which are both characteristics of 2D turbulence.

In the early 90s of the last century, characteristics of 2D turbulence were more convincingly validated with soap film experiments [22]. Film thicknesses of approximately $10\mu m$ can easily be obtained, corresponding to an extremely small aspect ratio (as compared to the horizontal length scales). However, soap film experiments suffer from subtle effects such as the influence of air drag and thickness variations influencing the 2D flow behaviour (see, e.g., [45]). Couder [22] towed a grid of cylinders through the soap film, and the decaying turbulent flow field showed merging of like-singled vortices (self-organisation). In fact, it were (decaying) turbulence

experiments in soap films that validated for the first time the predicted enstrophy cascade scaling exponent, see [46]. Later, the simultaneous inverse energy and direct enstrophy cascades were confirmed in similar soap film experiments regarding forced turbulence [13, 61, 76]. For a detailed review concerning (forced and decaying) soap film experiments, the reader is referred to Kellay and Goldburg [45].

Several methods to set the fluid into motion have been used in experiments. Directly injecting fluid in the container (see, e.g., [54, 85]), rotating solid flaps (see, e.g., [1]), or towing a rake of cylinders through the fluid (see, e.g., [59, 89]) have been used to initialize the flow. Electromagnetic forcing, i.e., application of the Lorentz force resulting from the interaction of a magnetic field (that permeates a fluid) and a current density (through the fluid), can be used to generate fluid motion. Note that the use of electromagnetic forcing to drive the fluid was already suggested by Gak and Rik in 1967 [35]. This electromagnetic forcing will be discussed in more detail in the next section. The reader is referred to van Heijst and Clercx [92] for a detailed overview on vortex generation techniques.

1.2.2 Electromagnetically-driven shallow fluid layers

In the late 1970s, a generic experimental setup to study 2D turbulence was introduced by Dolzhansii and co-workers (see, e.g., [12]), generally referred to as electromagnetically-driven shallow-fluid layer experiments. Here, two-dimensionality is assumed to be promoted only by the limited vertical dimension as compared to the horizontal length scales. The fluid is conveniently set into motion by the Lorentz force that results from the interaction of an electric current forced through an electrolyte and magnetic fields that originate from permanent magnets placed underneath the electrolyte. Note that the electromagnetic forcing is used to set the fluid in motion, not to two-dimensionalise the flow (i.e., in these electrolyte solutions the so-called Hartmann number $Ha \ll 1$). For a review on the experimental attempts to investigate 2D turbulence the reader is referred to Tabeling [87].

With this shallow fluid layer setup several characteristics of 2D turbulence were confirmed. Tabeling and co-workers performed the first of such experiments on decaying 2D turbulence [88]. They investigated the validity of the scaling predictions proposed by Carnevale *et al.* [14] on how the vortex density, radius, vorticity extremum, and enstrophy should behave

when the flow is 2D and turbulent.

From 2D numerical simulations it was already known that the boundedness of the flow domain affects the evolution of the flow, due to vorticity production at a lateral no-slip wall and spontaneous spin-up of the flow on non-circular domains (see, e.g., [95]). Besides this horizontal confinement, laboratory setups are also limited in the vertical direction by a free surface and a no-slip bottom. Often, it is assumed that this setup yields flows that behave in a quasi-2D fashion, i.e., a horizontal motion with a Poiseuille-like profile in the vertical direction (see, e.g., [20, 38, 67]). This assumption allows one to replace the 3D diffusion term $\nu \nabla^2 \mathbf{v}$ by the 2D diffusion $\nu \nabla^2 \mathbf{v}_{2D}$ supplemented by a linear friction term $\alpha \mathbf{v}_{2D}$, where α denotes the bottom friction coefficient (see, e.g., [26]). Note that the linear friction term is nonselective with respect to length scales, and is therefore able to act as an energy sink at large scales in numerical simulations (as opposed to the Newtonian viscosity, which predominantly removes energy at the small scales).

A way to minimise the influence of bottom friction on the measurement domain is to use a stably stratified two-layer setup instead of a single-layer setup. The rationale behind the two-layer setup is that the measurement layer (the top layer) is now shielded from the solid bottom by an extra layer (the bottom layer) and therefore reduces the influence of the no-slip bottom on the flow evolution in the measurement layer. The first reported study utilising such a two-layer configuration was by Tabeling and co-workers [60], again aimed at validating the scaling theory by Carnevale *et al.* [14]. The inverse energy cascade was measured by Paret *et al.* [68] in such a setup with two-layers, followed by the claim to have also measured the direct enstrophy cascade [66]. The effect of bottom friction on the k^{-3} scaling of the enstrophy cascade was investigated by Boffetta *et al.* [10], and they found a correction based on the bottom friction coefficient. This correction on the k^{-3} spectrum was later confirmed by Wells *et al.* [96] with 2D numerical simulations.

A slightly different version of the above mentioned two-layer setup is now commonly used. Here, the bottom layer is a dielectric fluid, immiscible with water (see, e.g., [73, 81, 103]). This enables in principle to achieve higher Reynolds numbers without destroying the stratification. With this modified setup, condensation in 2D turbulence [103], suppression of turbulence by mean flows [81], and pair dispersion in 2D turbulence have been studied [73].

1.2.3 Three-dimensionality in shallow-fluid experiments

Until recently, the assumption of 2D flow behaviour in shallow fluid layer experiments was based on hand-waving arguments and has not been tested directly. Based on the continuity of the velocity field it is expected that the magnitude of the vertical motion is proportional to the magnitude of the horizontal velocity multiplied by the aspect ratio. One of the few exceptions to this is the study of Paret *et al.* [67], in which momentum exchange between different layers inside the fluid was considered for this purpose. They conclude that the flow in a two-layer setup can be regarded as 2D. However, this conclusion was based on a single experiment of which the value of the Reynolds number is not mentioned.

Lin *et al.* [54] studied a single dipolar vortex in a homogeneous shallow fluid layer, generated by an impulsively started jet. They found a horizontal vortex structure, just in front of the primary dipolar vortex. This prevalent structure was seen to contain vorticity exceeding the primary vorticity by a factor of approximately two. The emergence of this structure was later confirmed by Sous *et al.* [85,86] in similarly generated dipoles (laminar and turbulent) for a homogeneous fluid layer, and by Akkermans *et al.* [2,3] in electromagnetically generated shallow flows (see also chapter 3 of this thesis). Sous *et al.* [85,86] relate the frontal circulation to the no-slip bottom and state that this frontal circulation is not present in a two-fluid layer setup based on their qualitative observations. Recent studies, however, have revealed that this frontal circulation is also present in the two-layer configuration [4] (see chapter 4 of this thesis).

Obviously, the presence of a solid bottom plays an important role in the evolution of the shallow fluid layer flow. Also, the way the flow is generated is important, e.g., impulsively started jet vs. electromagnetic forcing. For instance, the Lorentz force has a vertical component and its effect on the flow evolution is not yet clear. Only recently, accurate modelling of the Lorentz force (i.e., by using the full 3D magnetic field) as in the experimental situation have appeared in publications [2,3,51,74]. It was concluded that 3D simulations are required to accurately simulate the 3D electromagnetic forcing, even if the flow remains quasi-2D in terms of the energy distribution over the horizontal and vertical velocity components.

Furthermore, modelling bottom friction as a linear friction term has been questioned recently [2,3,51].

1.3 Aim and outline of this thesis

The objective of the study reported in this thesis is a deeper understanding of the influence of boundary and initial conditions on the development of 3D motion inside shallow fluid layers. Such thin-layer experiments are often used to validate theoretical and numerical results on 2D turbulence. However, in experimental realisations deviations from two-dimensionality are inevitable due to, e.g., the finite vertical dimension, presence of rigid boundaries such as lateral no-slip walls or the no-slip bottom, or the way the flow is set into motion. For this purpose, one of the most elementary vortex structures in 2D turbulence, an electromagnetically generated dipolar vortex is studied in a single- and two-layer configuration, both experimentally and numerically. The two-layer configuration was assumed to be an improvement over the single-layer setup in the sense that the flow evolution is less influenced by bottom friction.

Stereoscopic particle image velocimetry (SPIV) is used to experimentally measure the flow field inside the fluid layer. With this technique, all three velocity components are directly measured inside the fluid, offering direct information concerning the two- or three-dimensionality of the flow. Furthermore, fully 3D direct numerical simulations of the Navier-Stokes equations are performed, enabling the possibility of a comparison with the experiments, and, more important, allowing to investigate different initial and boundary conditions, which may be even impossible to realise in the laboratory experiment.

The third experimental configuration that is considered is a linear array of vortices situated close to a lateral wall. As opposed to the previously described single dipole in a one- or two-layer configuration, now particularly vortex-wall interactions are investigated. To some extent, this mimics the experimental configuration of 2D turbulence near rigid side walls. Furthermore, a numerical investigation into the influence of the 3D flow field and a lateral wall on passive tracer transport in this configuration is performed.

In the second chapter of this thesis the experimental and numerical tools are described. Chapter 3 presents the results of the dipolar vortex in a shallow layer of fluid. The influence of some obvious sources of 3D motion, such as free-surface deformations, bottom friction, and initialisation of the flow are discussed. Hereafter, in chapter 4 the extension to a two-fluid layer

setup is made, both experimentally and numerically. Chapter 5 focuses on the 3D motions in a continuously forced linear array of vortices near a lateral wall, as well as the possible influence of the three-dimensionality on particle dispersion. Finally, the main conclusions are summarized in chapter 6.

CHAPTER 2

Experimental and numerical techniques

This chapter describes the tools used to obtain the experimental and numerical results presented in Chapters 3 to 5. The first section describes the measurement technique, starting with introducing general concepts of stereoscopic particle image velocimetry. Then, particle image velocimetry (PIV) is briefly discussed. Subsequently, the used measurement technique, i.e., stereoscopic particle image velocimetry (SPIV) is described as this is an extension of the working principle of PIV. In the second section the laboratory setup is explained together with the performed experiments. In the last section the numerical method is discussed.

2.1 Measurement technique

2.1.1 Introduction

Stereoscopic particle image velocimetry is a popular measurement technique for the investigation of three-dimensional (3D) flows since it can resolve all three components (3C) of the velocity field on a two-dimensional (2D) plane. A SPIV setup typically consists of a light source illuminating particles that are added to the flow. The scattered light from these particles is recorded with two digital cameras. The displacements (and velocities) are then subsequently determined by evaluation of these digital image recordings. SPIV is well-suited for application to complex flows (e.g., turbulent flows) as it is a non-intrusive, whole-field technique that allows instantana-

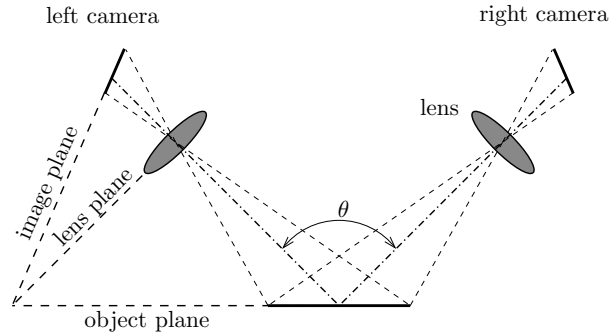


Figure 2.1 – Schematic illustrating the angular displacement method and Scheimpflug condition (i.e., image, lens, and object plane coincide on a single line). The stereoscopic angle θ is the angle between the two optical axes.

neous velocity field measurements.

The two cameras are arranged in the so-called angular displacement setup of which a schematic is shown in Fig. 2.1. The angular displacement method [70] is mostly employed nowadays as it generally provides higher measurement accuracy for the third (out-of-plane) velocity component [104], as opposed to the lateral translation method [71]. However, a consequence of this is that the object and lens plane are not parallel anymore. To maintain in-focus imaging, the image plane must be additionally tilted according to the Scheimpflug criterion, stating that image, lens, and object plane should coincide on a single line (see Fig. 2.1).

In order to correctly reconstruct a single 3C vector from two distinct two-component (2C) vectors derived from different cameras, it is important that both 2C vectors result from cross-correlation of the same physical interrogation volume. Therefore, one of the most important parts of the SPIV analysis involves establishing an accurate relationship between tracer particles in physical object space and their projections in image space (CCD array of the cameras). This transformation is expressed mathematically in terms of mapping functions, and various choices can be made, e.g., perspective equations (camera pinhole model) [31, 102], single-plane polynomial functions [52, 100], or full-volume polynomial functions [83]. In the latter case, the required coefficients can be determined by straightforward calibration procedures that often consist of recording a well-defined grid pattern at several out-of-plane positions resolving the light sheet volume. The advantage of the empirical approach based on polynomial mapping functions,

also referred to as in-situ calibration [52], is its straightforward numerical implementation, yet able to correct (depending on the polynomial order) for various optical distortions resulting from perspective projection, lens aberrations, and index of refraction changes that are not due to turbulence or sharp optical interfaces. Doing so, all relevant parameters are accounted for without any knowledge of the system parameters (such as focal length, lens plane position, etc.) which are often difficult to determine with sufficient accuracy. A disadvantage of the empirical approach is the inevitable misalignment between the calibration plane on the one hand, and the measurement plane defined by the light sheet on the other hand, which is often referred to as “light sheet misalignment” (LSM) [102]. Recently proposed misalignment corrections, however, adjust the original mapping functions based on mutual comparison of simultaneous particle recordings of distinct cameras [23, 78, 101].

An important competitor of SPIV methods is 3D particle tracking velocimetry (PTV), a measurement technique in which individual particle positions in 3D physical space are accurately determined by calculating the intersections of perspective rays associated with each recognised particle image (see e.g., [57, 65, 79]). Particle positions derived from subsequent camera images can be matched in order to reconstruct particle trajectories and the velocity along such trajectories, and 3D PTV is therefore extremely suitable for Lagrangian measurements in fluid flows, in contrast with SPIV. Reconstruction of the perspective rays requires calibration methods similar to those used for SPIV, and although a line intersection is fully determined by two perspective rays, often more than two such rays are desired in order to minimise errors due to “particle hiding”. Modern 3D PTV techniques such as the ones cited above, therefore use three to four cameras. In SPIV, however, particle hiding is negligible as the imaged volume consists of a sheet, so that two cameras are sufficient to calculate reliable intersections.

In the “Vortex Dynamics and Turbulence” group at Eindhoven University of Technology there are several measurement techniques available, e.g., (S)PIV and (3D)PTV. As the goal is to study the 3D structures in shallow fluid layers, only SPIV and 3D-PTV are considered as suitable techniques as they provide information of all three velocity components on a certain domain. The major advantage of 3D-PTV with respect to SPIV is that it is a genuine 3D method, providing information of the 3D velocity in the entire measurement volume. However, this is strictly not necessary and SPIV (all three velocity components on a 2D plane) is more than sufficient for shallow

fluid-layer flows. Furthermore, in principle a higher spatial resolution can be attained with SPIV as compared to 3D-PTV. For these reasons, SPIV has been chosen as the measurement technique.

2.1.2 Particle image velocimetry

Particle image velocimetry is an indirect measurement technique that provides in-plane velocity components on a spatial domain, through the motion of seeding particles. Of course, for this measurement to be useful these particles must follow the flow faithfully. The measurement domain is defined by the light source used to illuminate the seeding particles in the flow. A digital camera, perpendicular to the plane defined by the light source, records the particles at two instance of time, i.e., at t and $t + \Delta t$. These two particle images (I_t and $I_{t+\Delta t}$) are subdivided into interrogation windows. The displacement between the two corresponding windows is then determined with the use of cross-correlation. The cross-correlation is similar in nature to the convolution of two functions and therefore computationally expensive. For this reason, the cross-correlation is computed in the Fourier space. As there is only information on discrete integer values from the digital measurement images (i.e., pixels), an improvement is obtained by using sub-pixel interpolation. The maximum in the Signal-to-Noise map gives the statistically most probable displacement between the two interrogation windows. For all windows of the measurement image this process is repeated so that the displacement vectors are determined for the complete domain. As the time between the two particle images Δt is known, the velocity can be computed with the relation $\mathbf{v} = \Delta \mathbf{x} / \Delta t$ (where \mathbf{v} and $\Delta \mathbf{x}$ are the in-plane velocity and displacement, respectively).

Clearly, an important aspect of PIV is the use of seeding particles as the flow is measured indirectly through the particle motion. This puts certain restrictions to the particle material and diameter (the particle is assumed to be spherical). The particles should be small enough to follow the flow faithfully but large enough to sufficiently scatter light and avoid “peak-locking” [71].

How well these particles follow the flow is characterized by the Stokes number $St = \tau_p / \tau_f$, where $\tau_p = d_p^2 \rho_p / 18 \mu_f$ is the particle response time to acceleration and τ_f the characteristic time scale of the flow (d_p and ρ_p represent the particle diameter and density, μ_f denotes the dynamic viscosity of the fluid). For a Stokes number $St \ll 1$ these seeding particles follow

the flow passively; the motion of the particles, which is measured, is then representative for the fluid motion (see Sect. 2.2.1 for details).

2.1.3 Stereoscopic particle image velocimetry

By adding a second camera, where the two cameras view the region of interest from different angles, SPIV is able to retrieve all three velocity components. In fact, this depth-perception is similar to human vision [69]. The developed SPIV techniqueⁱ consists of a calibration procedure (including a misalignment correction), measurement image evaluation, and finally a 3C reconstruction. The description of the measurement technique in this subsection is based on an internal report [91].

Mapping functions and in-situ calibration

Stereoscopy enables one to reconstruct a single 3C displacement vector from two 2C displacement vectors. The 2C displacement vectors are obtained from two separate PIV calculations, which in the present algorithm are performed in physical space. This requires prior back-projection of the original images to physical space, which is referred to as dewarping.

The back-projection is implemented using mapping functions. The different camera viewing angles, characteristic for the angular displacement method, result in a perspective distortion that differs for each camera. Therefore, mapping functions must be determined for the two individual cameras. Assuming the light sheet coincides with the plane $Z = Z_0 = \text{constant}$, these mapping functions are given by

$$\mathcal{M}_L : \mathbf{x}_L \rightarrow \mathbf{X}_0, \quad \mathcal{M}_R : \mathbf{x}_R \rightarrow \mathbf{X}_0, \quad (2.1)$$

with subscripts ‘ L ’ and ‘ R ’ referring to the Left and Right camera, respectively. Functions \mathcal{M}_L and \mathcal{M}_R map the image space coordinates $\mathbf{x}_L \equiv (x, y)_L$ and $\mathbf{x}_R \equiv (x, y)_R$, respectively, to the corresponding physical space coordinate $\mathbf{X}_0 \equiv (X, Y, Z_0)$. For reasons outlined in Sect 2.1.1, multi-plane polynomial expressions are used for functions \mathcal{M}_L and \mathcal{M}_R .

ⁱL.J.A. van Bokhoven is acknowledged for his contribution to the development of the here presented SPIV measurement technique. The description of the measurement technique in this Section is based on an internal report [91]: L.J.A. van Bokhoven, R.A.D. Akkermans, H.J.H. Clercx, G.J.F. van Heijst, Triangulation based stereoscopic PIV with misalignment correction, Technical Report R-1746-D, TU/e, 2009.

The reader is referred to [47] for a detailed description of the multi-plane polynomial expressions and its application.

The polynomial coefficients of transformation (2.1) are determined by a straightforward in-situ calibration, with the aid of calibration images (see Fig. 2.2). A well-defined grid pattern is used for the calibration, i.e., an

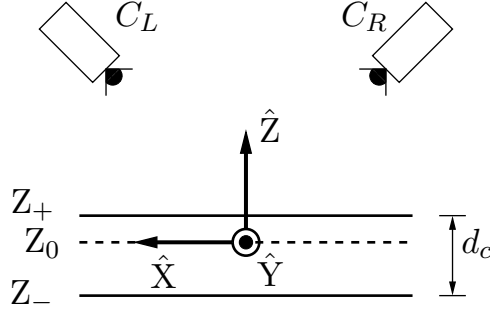


Figure 2.2 – Schematic of the calibration procedure (side view). The calibration grid is first recorded at Z_- . Subsequently, it is uniformly shifted over d_c in the \hat{Z} -direction to Z_+ . Hereafter, a second recording is made.

equidistant pattern (in X - and Y -direction) of white dots on a black background. Typically, this grid consists of more than 100 dots, three of which are larger and define the origin and the \hat{X} - and \hat{Y} -axes. The \hat{Z} -axis is taken according to the right-hand-rule. Note that this coordinate system is used “inside” the SPIV technique and does not necessarily coincide with the coordinate system used to present the results in the following chapters. The calibration grid pattern is then recorded at parallel planes Z_- and $Z_+ = Z_- + d_c$, with d_c the distance between the two planes. Subsequent image analysis allows one to construct discrete mapping functions for both calibration planes. Assuming that the light sheet coincides with the plane Z_0 ($Z_- \leq Z_0 \leq Z_+$), the continuous mapping functions \mathcal{M}_L and \mathcal{M}_R for plane Z_0 can be easily computed from the discrete mapping functions for planes Z_- and Z_+ using linear interpolation and least-squares fitting procedure.

Besides determining the coefficients of the mapping functions \mathcal{M}_L and \mathcal{M}_R , in-situ calibration is also required to reconstruct the perspective rays that are essential for the light sheet misalignment correction (LSMC) and 3C reconstruction. Furthermore, in-situ calibration allows easy computation of the common area, defined as the physical space recorded by both cameras. Clearly, in-situ calibration plays a crucial role in the present SPIV

algorithm.

Finally, back-projection of deformed images also requires a suitable interpolation scheme. Recent performance assessments by [5], and [48] have shown that the accuracy of a PIV algorithm in terms of systematic and total errors is strongly influenced by the type of interpolation scheme used for this reconstruction. Based on the outcome of these studies a cubic B-spline interpolation scheme is used, which is a good compromise between speed and accuracy.

Light sheet misalignment correction

As already mentioned in Sect. 2.1.1, a disadvantage of the empirical approach is the inevitable misalignment between the calibration plane and the measurement plane defined by the light sheet. In practice, a well-aligned light sheet will still be both tilted and shifted with respect to plane Z_0 so that the assumption made in the previous Section is invalid (i.e., a perfect alignment of measurement and calibration plane). This type of misalignment will lead to erroneous 3C vectors since the 2C PIV vectors of the left and right cameras are no longer obtained from the same physical interrogation volume.

Fortunately, this type of misalignment can be corrected for by using the so-called disparity map and a procedure that is referred to as triangulation [101]. A disparity map follows from cross-correlating simultaneous particle recordings of the left and right camera. Each disparity vector represents the (X, Y) -displacement that maximises the correlation between the corresponding interrogation windows of the dewarped images, and thus quantifies the degree of misalignment. For instance, zero disparity reflects the case of a light sheet that is perfectly aligned with the calibration plane Z_0 . The disparity map was already used by [102] to correct the position at which the corresponding 2C vectors for the left and right camera are calculated. A more advanced approach for the case of normal lenses with Scheimpflug adapters involved recomputing a corrected mapping function from the disparity map, also referred to as self-calibration [32,101]. The misalignment correction presented below is actually identical to that of [101], and uses mapping functions based on empirical multi-plane polynomials.

The main ingredient of the misalignment correction is to construct a relationship between the camera image spaces and the tilted light plane in physical space. This transformation can be expressed in terms of the

following mapping functions

$$\mathcal{M}_L^s : \mathbf{x}_L \rightarrow \mathbf{X}^s, \quad \mathcal{M}_R^s : \mathbf{x}_R \rightarrow \mathbf{X}^s, \quad (2.2)$$

which map the image space coordinates of the two cameras to the corresponding physical space coordinates within the light sheet, denoted by $\mathbf{X}^s \equiv (X^s, Y^s, Z^s)$. Again, multi-plane polynomial expressions are used for the mapping functions \mathcal{M}_L^s and \mathcal{M}_R^s . The polynomial expressions are chosen such that LSM due to a slightly parabolic shape of the light sheet is also corrected for. The coefficients of transformation (2.2) are determined as explained below.

First, a simultaneous particle recording is made by both cameras. For these images, one uses actual measurement images so that no extra images need to be taken for the LSMC. However, the (measurement) images used during the LSMC are further referred to as “misalignment images” to distinguish them from the particle images used for 3C reconstruction (see Sect. 2.1.3). The mapping functions \mathcal{M}_L and \mathcal{M}_R , see (2.1), are then used to back-project the misalignment images to the estimated light plane $Z = Z_0$. Next, the dewarped images are cross-correlated using a PIV algorithm based on dynamic 2D Fast Fourier Transforms [98] with an in-plane particle-loss correction [97]. Each disparity vector is then triangulated to calculate the positional difference between the estimated light plane and the true light plane, see Fig. 2.3. Triangulation requires exact knowledge of the perspective rays through the initial and final points of each disparity vector. Such information is retrieved from the inverse mapping functions

$$\mathcal{M}_L^{\leftarrow} : \mathbf{X}_0 \rightarrow \mathbf{x}_L, \quad \mathcal{M}_R^{\leftarrow} : \mathbf{X}_0 \rightarrow \mathbf{x}_R, \quad (2.3)$$

with polynomial expressions for $\mathcal{M}_L^{\leftarrow}$ and $\mathcal{M}_R^{\leftarrow}$, the coefficients again extracted from the calibration data. The intersection points obtained from triangulation are finally used in a least-squares fitting procedure to solve the coefficients of the transformation functions of the true, tilted light plane, \mathcal{M}_L^s and \mathcal{M}_R^s .

Following [101], ensemble-averaging is performed over a series of disparity maps computed from many image pairs [62] to improve the statistical accuracy of the disparity map. Depending on the particle density and the thickness of the light sheet, about 5 to 50 image pairs are typically needed to compute an accurate disparity map from a well-shaped correlation peak. The ensemble-averaged disparity map is subsequently analysed by a universal outlier detection algorithm [99] to detect and replace any remaining

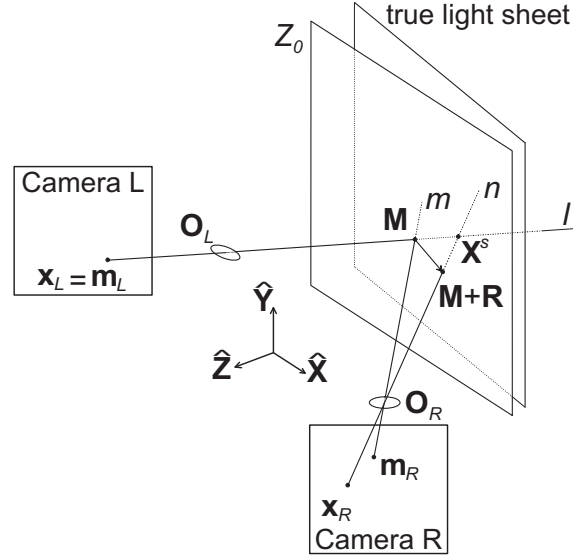


Figure 2.3 – Laser sheet misalignment correction based on triangulation of perspective rays. First, the 2C disparity vector \mathbf{R} is determined at PIV node \mathbf{M} in physical space. Next, the image points \mathbf{x}_L and \mathbf{x}_R are determined for the initial and final point, respectively, of the disparity vector \mathbf{R} . Finally, perspective rays l and n , corresponding to the image points \mathbf{x}_L and \mathbf{x}_R , respectively, are reconstructed and triangulated to obtain the coordinates of the light sheet coordinate \mathbf{X}^s .

spurious disparity vectors. Doing so, a reliable disparity map is obtained for the triangulation procedure, improving the accuracy of the mapping functions (2.2).

Three-component reconstruction by triangulation

Above it was described how the required mapping functions are obtained from the calibration. The next step is how to reconstruct a 2D3C displacement field from simultaneous particle recordings made by the left and right camera at times t and $t + \Delta t$. First, consider the left camera. The acquired particle recordings are dewarped using the mapping function \mathcal{M}_L^s [see (2.2)]. The succeeding (dewarped) particle recordings are then cross-correlated using the above-mentioned PIV algorithm to compute the 2D2C displacement map $\{\mathbf{D}_L^{2C}\}$ — 2D2C because the PIV computations

use a 2D orthogonal coordinate frame of which the base vectors span the light plane in physical space. This raw 2D2C displacement map is analysed by the universal outlier detection algorithm mentioned previously. The filtered 2D2C displacement field is then transformed to the physical space coordinate frame defined by the calibration procedure, yielding the 2D3C displacement field $\{\mathbf{D}_L^{3C}\}$. A similar procedure is repeated for the right camera (using \mathcal{M}_R^s instead of \mathcal{M}_L^s) to obtain the 2D3C displacement map $\{\mathbf{D}_R^{3C}\}$. The displacement maps of both cameras are associated with the centres of the interrogation windows, \mathbf{M}^s .

Finally, the physical space points $\mathbf{M}^s + \mathbf{D}_L^{3C}$ and $\mathbf{M}^s + \mathbf{D}_R^{3C}$ of a given interrogation window are triangulated in the same way as the initial and final point of a disparity vector are triangulated. The resulting intersection points $\{\mathbf{X}^{3C}\}$ are exactly the final points of the 3C displacement vectors that we are interested in. The final 2D3C displacement field thus consists of the 3C vectors $\{\mathbf{X}^{3C} - \mathbf{M}^s\}$ at corresponding coordinates $\{\mathbf{M}^s\}$. This final 2D3C displacement map is generally post-processed to detect and replace any spurious 3C displacement vectors.

2.2 Experimental setup

The laboratory experiments have been performed in a tank with two important characteristics. First, a shallow layer of electrolyte is used, where shallow means that the geometry confines the motion predominantly to the horizontal plane. Second, the motion of the fluid is driven by electromagnetic forcing.

A disk-shaped magnet is placed underneath the fluid layer and an approximately uniformly distributed electrical current is running through the fluid, between two electrode plates mounted along opposite side walls. The interaction of the current density \mathbf{j} and the magnetic field \mathbf{B} induces a Lorentz force that sets the fluid in motion. Our experimental setup is similar to that used in several other studies by, e.g., Dolzhanskii *et al.* [26], Danilov *et al.* [24], and Tabeling and co-workers [67, 68] (where the latter authors use a stably stratified two-layer system). Note that the electromagnetic forcing (i.e., the magnetic field) in the shallow flow setup is used to set the fluid in motion, not to two-dimensionalise the flow.

Three types of experiments have been performed, i.e., (i) the evolution of a dipolar vortex in a single fluid layer has been investigated (results presented in Chapter 3), (ii) a similar study of the dipole evolution in a

stably stratified two-layer system has been conducted (Chapter 4), and (iii) the dynamics (and dispersion properties) of a line of vortices parallel to a lateral wall in a single-fluid layer has been studied qualitatively (Chapter 5). First the setup used for the single layer dipole experiments will be presented as this is the most straightforward. Hereafter the extension to the two-layer experiments will be elucidated, and finally the setup used for the study of the line of vortices is given.

2.2.1 Dipolar vortex in a single-fluid layer

A schematic of the setup used for the dipolar vortex study in the single fluid layer is depicted in Fig. 2.4. The left-hand side of this figure shows

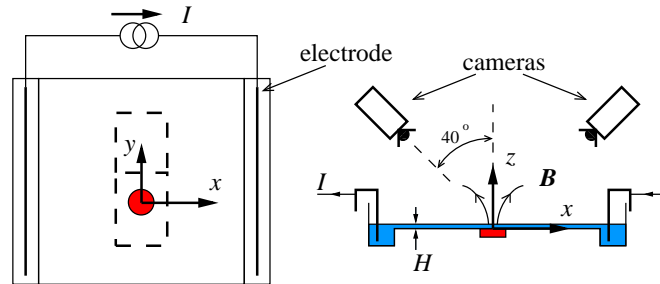


Figure 2.4 – (Colour online)ⁱⁱ Schematic of the experimental tank showing the x, y, z -coordinate system; Left: top view, right: cross section. The electrical current is denoted by I , the fluid depth with H , and \mathbf{B} represents the magnetic field produced by the magnet.

a top view of the $52 \times 52 \text{ cm}^2$ square tank with one disk-shaped permanent magnet below the bottom. The bottom plate has a thickness of 1 mm. Two rectangular-shaped electrodes are placed on opposite sides of the tank, leading to a uniform current density in the x -direction. A single layer of sodium chloride solution (NaCl, 15% Brix) serves as the conducting fluid enabling the electromagnetic forcing. The magnet is placed approximately in the middle of the tank to minimize the influence of the lateral walls and non-uniformities in the current density.

We adopt a Cartesian coordinate frame, with the x - and y -axes spanning a plane parallel to the bottom of the tank, and the z -axis is taken vertically upward. The origin of the coordinate system lies above the cen-

ⁱⁱHere and in the remainder, “Colour online” refers to the digital record of this thesis available from the website of the Eindhoven University of Technology Library.

tre of the magnet on the bottom of the tank. The y -axis coincides with the propagation direction of the dipole. The three velocity components in the x -, y -, and z -direction are denoted by u , v , and w , respectively. The cylindrical magnet (indicated in Fig. 2.4), with a diameter of 25 mm and thickness of 5 mm, is assumed to be uniformly magnetized in its axial direction and produces a magnetic field with a magnitude of the order of 1 T.

The forcing protocol to generate the dipolar vortex constitutes of a 1 s pulse of constant current strength I . This protocol was determined empirically, a very short pulse would need to be accompanied by a too high current strength, a too long pulse would result in a jet-like flow. Time t was set to zero at the onset of forcing for all the results in the remainder of this thesis.

The right-hand side of Fig. 2.4 shows a cross-section of the experimental set-up. Two cameras, placed at an angle, enable the use of SPIV [71] to measure the full three-component velocity field in a horizontal plane inside the fluid layer. The two cameras (Kodak Megaplug ES1.0 with sensor resolution 1008×1019 pixels, $f_{\#} = 2.8$) are mounted on Scheimpflug adaptors to enable in-focus imaging of the entire field of view, as the stereoscopic angle is approximately 80 degrees. The flow is illuminated with a dual pulse Nd:Yag laser (Spectron Laser SL454, 200 mJ/pulse) to produce a horizontal light sheet of 1 mm thickness. In order to limit the in-plane particle loss [71] and for correct temporal sampling of the signal, a delay time between laser pulses of 10 ms is chosen. The cameras and the light source are synchronized with a delay generator. With this setup, image pairs (and finally velocity fields) are acquired at 15 Hz.

The typical field of view is approximately $8.5 \times 7 \text{ cm}^2$ in x - and y -direction, respectively. The area covered by the cameras is indicated schematically in Fig. 2.4 by the two dashed rectangles. The rectangle around the position of the magnet is our viewing area during the forcing phase. As the dipole will be propagating in the positive y -direction, the upper rectangle represents the field of view used to study its evolution. During post-processing, all images are sampled at a resolution of 896^2 pixels based on the common field of view of the two cameras; the PIV analysis involves square interrogation windows of 32^2 pixels and 50% overlap between neighbouring windows. After post-processing, these settings result in SPIV velocity fields that are resolved on a 55×55 spatial grid, corresponding to physical grid spacing of (1.55;1.25) mm in x - and y -direction, respectively. In a correlation window of 32^2 pixels there are on average 16 seeding particles present.

The fluid is seeded with polystyrene particles having a mean diameter d_p of $20\ \mu\text{m}$ and a specific density ρ_p of $1.03 \cdot 10^3\ \text{kg}/\text{m}^3$. The volume fraction of the particles is of the order 10^{-5} , so that the seeding particles have a negligible influence on the flow properties. Settling of the seeding particles is negligible as $\rho_p \approx \rho_f$. The flow time scale τ_f is estimated as $1/\omega_{z,max} \approx 0.08\ \text{s}$, yielding a Stokes number $\text{St} = \tau_p/\tau_f$ of $2 \cdot 10^{-4}$, indicating that the particles follow the flow passively.

As is to be expected, the influence of the flow on the magnetic field is negligibly small, since the magnetic Reynolds number Re_m , defined as $\mu\sigma\mathcal{U}\mathcal{L}$, is small [$\text{Re}_m \sim \mathcal{O}(10^{-7})$]. Here μ and σ denote the magnetic permeability and electric conductivity, respectively.

The main goal of these experiments (together with the numerical simulations) is to understand (i) what causes the development of 3D motions in shallow flows, (ii) how does the geometrical confinement influence this development of 3D motions, and (iii) how can one quantify the deviation from two-dimensionality. For this purpose, several experiments have been performed where the fluid height (or importance of geometrical confinement and bottom friction) and forcing strength are varied. Furthermore, measurements were carried out at different levels inside the fluid layer. In total 25 experiments were performed with different combinations of fluid depth H (ranging from 11.4 mm to 6.0 mm) and current strength I (2.4 A to 6.4 A). The details of these experiments are presented in Sect. 3.2.

2.2.2 Dipole in a two-layer fluid

The shortcomings of the single-layer setup have been recognized and nowadays the two-layer fluid setup, consisting of a lighter fluid layer on top of a heavier bottom layer, has become quite standard [10, 67, 68, 73, 80]. The rationale behind the two-layer setup is that the measurement layer (the top layer) is now shielded from the no-slip bottom by an extra layer (the bottom layer) to minimize the influence of the no-slip bottom on the flow evolution.

The first study employing the two-layer configuration was by Tabeling and co-workers [60] in 1995. They used a stable configuration of two electrolytes. Basically there are three variations possible for the two-layer configuration: (i) two layers of electrolyte in a stable configuration [40, 41, 60, 66–68], (ii) a layer of fresh water above an electrolyte [10], and (iii) an electrolyte on top of a dielectric fluid (which is immiscible with the electrolyte) [73, 81, 103]. Nowadays the latter configuration is commonly used as

molecular diffusion of salt between the two layers is virtually absent. More importantly, higher Reynolds numbers can be achieved without destroying the stratification (due to absence of mixing between the two layers).

The experimental setup used for the two-layer experiments is identical to the setup described in the previous Sect. 2.2.1, except a two-layer fluid system is used, therefore a concise description follows.

The laboratory setup consists of a shallow two-layer fluid in a stably stratified situation: a denser dielectric lower fluid layer and a lighter conducting upper layer of thickness H_{ul} . In all the experiments the bottom fluid layer depth H_{bl} is kept constant at 3 mm, while the upper layer depth H_{ul} was varied between 3.5 mm and 9.0 mm. The density of the lower fluid (3MTM NovecTM Engineered Fluid HFE-7100) is $1.52 \cdot 10^3 \text{ kg/m}^3$ (about 1.5 times the density of the electrolyte), and it is immiscible with top layer (thereby excluding vertical mixing between the two layers). The upper layer is a sodium chloride solution (NaCl, 10% Brix), which serves as the conducting fluid enabling the electromagnetic forcing. Note that the forcing is only active in the top layer. In all the two-layer experiments reported here, the forcing protocol consisted of a 1 s pulse of approximately constant current density ($j_x \approx 0.13 \text{ A/cm}^2$).

A schematic of the set-up is depicted in Fig. 2.5. SPIV [2] measure-

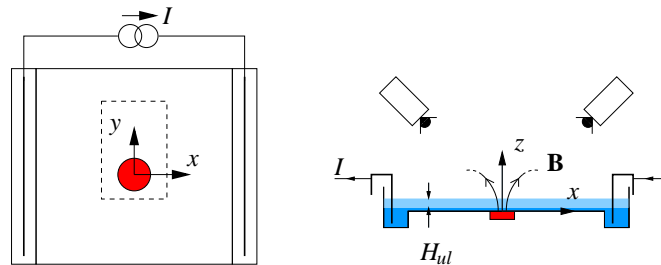


Figure 2.5 – (Colour online) Schematic of the experimental tank showing the x, y, z -coordinate system; Left: top view, right: cross section. The electrical current is denoted by I , the fluid depth of the top layer with H_{ul} , and \mathbf{B} represents the magnetic field produced by the magnet. The field of view is indicated by the dashed rectangle.

ments are performed inside the top fluid layer, always at mid-depth of this top layer. Images were acquired with two Kodak ES2020 cameras (different from the single-layer experiments) having a resolution of 1200×1600 pixels. After post-processing, velocity fields were resolved on a 60×79 spatial

grid, corresponding to a grid spacing of approximately 1 mm in both x - and y -direction. The area that is observed is illustrated schematically in Fig. 2.5 by the dashed rectangle (approximately $5.5 \times 7 \text{ cm}^2$).

The goal of these experiments is to determine if the two-layer fluid is indeed an improvement over the traditional one-layer setup. For this purpose, the 3D structures that develop in a shallow two-layer fluid are addressed, and a comparison is made with the single-fluid layer experiment. The behaviour of the flow is discussed when decreasing the fluid height H_{ul} in steps down to almost 3 mm (i.e., 9, 7, 5, and 3.5 mm), the latter mimicking the traditional fluid-layer height for 2D turbulence experiments (see, e.g., [67, 68, 73, 80]). Further details of these experiments are presented in Sect. 4.2.

2.2.3 Linear array of vortices

The two experimental setups described previously are aimed at studying the 3D structures and evolution of a single dipolar vortex in shallow fluid configuration. This dipole is a generic vortex structure of 2D turbulence. However, when putting theoretical and numerical predictions on 2D turbulence to a test with shallow laboratory experiments, one has to realise that many dipoles are generated by using a chessboard of magnets (see, e.g., [88]). In such a situation, both vortex-vortex and vortex-wall interactions may become important in altering the (2D or 3D) flow evolution [16, 17]. Note that it was already known from 2D turbulence simulations that the boundedness of the flow domain alters the evolution and spectral characteristics of 2D turbulence significantly [18, 19, 90, 93, 95, 96].

Turbulent dispersion of passive tracers has been studied in such electromagnetically forced shallow flows, motivated by the geophysical context. Dispersion characteristics in shallow flow setups are often studied by “dye” visualisations using one camera or single-camera PIV or PTV, viewing the flow from above (see, e.g., [73]). However, this configuration neglects the possible 3D flow structure, questioning the validity to experimentally verify theoretical and numerical results on 2D turbulent dispersion with these approaches.

The third experimental configuration that has been considered in this study is a linear array of vortices close to a wall. As opposed to the previously described single dipole in a one- or two-layer configuration, now particularly vortex-wall interactions are present. This mimics the experimental configuration used to study 2D turbulence (near rigid side walls).

The goal of these experiments is to investigate the flow evolution in a shallow fluid close to a lateral wall. The boundary layer that develops at such a wall produces small-scale vorticity and alters the 2D or 3D flow evolution. To study these processes, measurements are performed with and without a lateral wall. Furthermore, a time dependent electromagnetic forcing is used so that the activity of the small-scale vorticity production can be varied in time.

In order to generate this line of vortices in the shallow fluid tank a row of magnets is placed underneath the bottom (1 mm spacing between adjacent magnets) with neighbouring magnets having reversed polarity. In Fig. 2.6(a) a schematic (top view) is displayed of the experimental setup without a lateral wall. With the x - and y -axes as indicated in this figure, the z -axis is taken upward. A total of 14 magnets is used, where white (gray) means “North” (“South”) pointing in the positive z -direction. In

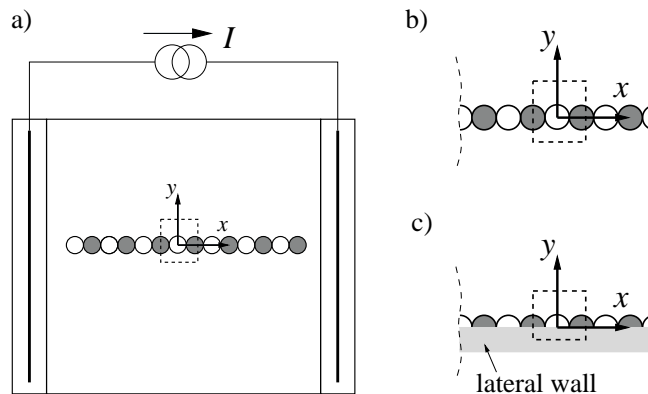


Figure 2.6 – (a) Schematic top view of the experimental tank showing the coordinate system and magnet arrangement. (b) Close-up of the field of view. (c) Close-up showing field of view and the position of the lateral wall.

Fig. 2.6(b) a close-up of the field of view is presented of the setup without a lateral wall. The field of view ($7 \times 7 \text{ cm}^2$) is approximately in the middle of the tank and spans about 2.5 magnets in the x -direction, as indicated by the dashed rectangle. In Fig. 2.6(c) this close-up is shown with the lateral wall. This wall is positioned such that the wall coincides with the centre points of the magnets (and spans the full width of the tank). The motivation for this positioning is that the maximum horizontal velocity in the y -direction is expected near the magnet centres, and therefore the activity

of the boundary layers at the lateral wall is intense. The field of view for the situation with a wall is approximately $7 \times 4 \text{ cm}^2$.

For all experiments the tank was filled with a single 7.0 mm fluid layer, where measurements are performed at mid-depth of this fluid layer with SPIV. For the experiments where a lateral wall is present, a drop of detergent is added to the fluid to decrease the concave meniscus of the fluid at the lateral wall.

As opposed to the previous experiments, a continuous forcing is utilized that changes in time. As the location and strength of the magnets are constant, the variable forcing is accomplished by changing the applied current, i.e., $I = I(t)$. The shape of $I(t)$ is chosen as a sinus function with mean value a and amplitude b , as depicted in Fig. 2.7. Two different combinations were

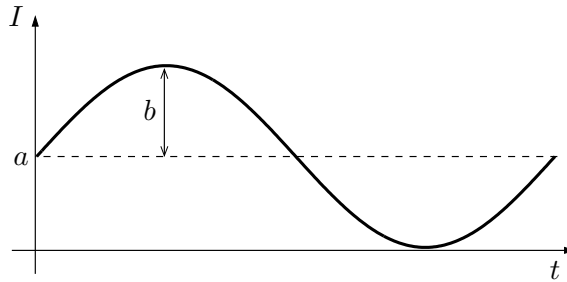


Figure 2.7 – Schematic of the sinus forcing current I with mean a and amplitude b . Note that only one period is shown.

used, viz. $a = 0$ and $b \neq 0$, or $a = b$. Typical values used (for both cases) are $b = 0.5 \text{ A}$ and $b = 2.5 \text{ A}$. It is expected that the combination $a = 0$ and $b = 0.5 \text{ A}$ yields a low Reynolds number flow with no global mean flow. As opposed to this, the combination $a = 0$ and $b = 2.5 \text{ A}$ is expected to result in a flow that is dominated by advection. With an offset present, i.e., $a \neq 0$ a mean flow is introduced. The frequency of $I(t)$ was kept constant at 0.25 Hz. The motivation for this forcing frequency is that the flow is altered most efficiently with a temporal period of the forcing of the same order of magnitude as the characteristic time scale of the flow (i.e., the eddy turnover time of the dipolar vortices). Measurements are performed during 50 seconds, so that at least 10 forcing periods are recorded.

Note that specific choices have been made for the parameter regime that is to be considered in the experiments with the linear array of vortices (such as forcing protocol, magnet positions, and position of the lateral wall). Therefore, the corresponding results chapter is a more qualitative study to

explore the three-dimensionality and the transport properties of the flow.

2.3 Numerical method

The experiments, as described in the previous section, will be confronted with numerical simulations obtained with the commercial software code COMSOL Multiphysics [21]. These simulations are aimed at mimicking the experimental ones. Furthermore, the influence of different boundary and initial conditions can be investigated numerically whereas this would be troublesome or even impossible in the experiments. This section is organised in a similar way as the previous one, i.e., the numerical setup used for the single-layer dipole, the two-layer dipole, and the linear array of vortices are presented.

2.3.1 Numerical setup single-layer dipole

The numerical simulations are based on the Navier-Stokes equation for an incompressible fluid, i.e.,

$$\frac{\partial \mathbf{v}}{\partial t} + (\mathbf{v} \cdot \nabla) \mathbf{v} = -\frac{1}{\rho} \nabla p + \nu \nabla^2 \mathbf{v} + \frac{1}{\rho} \mathbf{f}_L, \quad (2.4)$$

complemented by the continuity equation for an incompressible fluid

$$\nabla \cdot \mathbf{v} = 0, \quad (2.5)$$

where \mathbf{v} is the 3D velocity, p the pressure, ρ the mass density, ν the kinematic viscosity, and \mathbf{f}_L the external body force.

The Navier-Stokes equation is solved using a finite element method [21] in the three spatial dimensions in conjunction with adaptive meshing and error control. The external body force \mathbf{f}_L in (2.4) represents the electromagnetically generated Lorentz force, resulting from the interaction of the magnetic field \mathbf{B} with the current density \mathbf{j} , i.e.,

$$\mathbf{f}_L = \mathbf{j} \times \mathbf{B}. \quad (2.6)$$

Here the current density is a uniform and constant pulse of 1 s duration in the x -direction ($\mathbf{j} = j_0 \mathbf{e}_x$ for $0 < t \leq 1$ s and $\mathbf{j} = 0$ for $t > 1$ s), similar to the forcing applied in the experiments. Since the electromagnetic forcing

inside the fluid layer does not take place in the so-called far field of the permanent magnet, a point-dipole approximation of the magnetic field is not justified here. Therefore we use exact expressions known in analytical form for the magnet’s magnetic field, derived under the assumption that the magnet’s magnetization current can be modelled as a stack of current-carrying circular wires, the magnetic field of which can be written in terms of elliptic integrals (see, e.g., [37]).

Note that although the magnetic field drives the fluid into motion, this motion does not introduce an induced magnetic field, as the magnetic Reynolds number $Re_m \ll 1$ (see Sect. 2.2.1). Hence, the magnetic field is computed first and hereafter used as an input for (2.4) – there is no need to solve them simultaneously.

As the magnet’s strength is not exactly known, it is adjusted in such a way that the numerical simulation matches the corresponding laboratory experiment at some arbitrary moment in time. For this matching one can use different criteria, such as the maximum of the vertical vorticity component or the “horizontal” kinetic energy, both at the end of the forcing period. The former matching criterion is used for the numerical results presented in the remainder of this thesis, as the local magnitude of the vertical vorticity determines the strength (and thus the speed) of the dipole at a certain height inside the fluid.

The computational domain is identical to the experimental one with the exception of the lateral (outer) domain boundary (see Fig. 2.8). This is taken circular (for computational efficiency) with a diameter of 7 times the magnet diameter, whereas the experimental setup has a square outer boundary. It has been checked by simulations with a larger circular domain that its size did not affect the result. The small, solid gray circle in Fig. 2.8 (top view) represents the domain above the magnet. The outer domain is shifted in the positive y -direction as the dipole will be propagating in this direction. The dashed circle represents the border between a fine meshed domain (closer to the magnet) and a domain with a coarser mesh (outer region). Furthermore, use was made of the symmetry in the domain, indicated with the dashed line in Fig. 2.8, i.e., only the right part of the domain was used. For some cases it was checked with a simulation of the full domain that this imposition of symmetry did not affect the result.

To acquire the desired accuracy in a typical run, the computational domain is discretized with approximately 50,000 mesh elements, with finer elements being used near the bottom, near the free-surface, and close to the

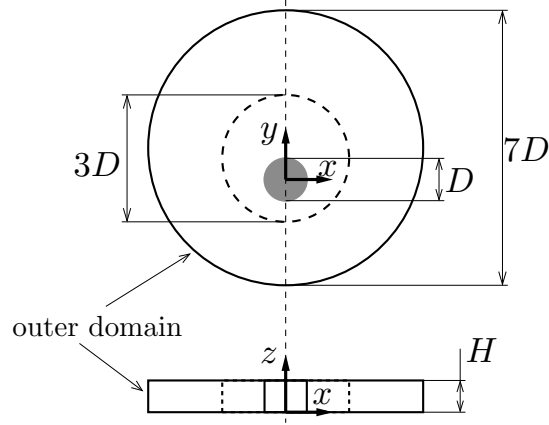


Figure 2.8 – Schematic top and side view of the computational domain for the single fluid layer simulations. Magnet location is indicated by the gray circle. Note that the thickness of the fluid layer H is not in scale with the magnet diameter D .

magnet (where the forcing is strongest) in order to resolve the gradients in the local flow field. The resulting number of degrees of freedom solved for is approximately 250,000. Convergence of the solution is checked with the aid of δ given by

$$\delta(t) = \sqrt{\frac{\iint_S (\omega_1^2 - \omega_2^2) dA}{\iint_S \omega_1^2 dA}}, \quad (2.7)$$

where ω_1 and ω_2 represent the vorticity vector obtained from the fine and coarser mesh, respectively. Integration is performed over a horizontal plane S . This error remains below a few percent for the complete duration of temporal integration. The theoretical order of convergence is third-order in space and time [21]. The time integration is started with a lower-order method.

Two types of numerical simulations have been performed. In all runs the upper free-surface was taken to be stress-free and flat. The latter implies that the generation of surface gravity waves is excluded in the numerical simulations. The first set of runs were aimed to simulate the experimental results. For that purpose, a no-slip boundary condition is imposed at the bottom of the computational domain. In order to examine how the bottom boundary layer at a no-slip bottom is related to the 3D flow structures found experimentally and numerically, a second set of simulations has been

performed. In these runs the bottom, just like the upper surface of the fluid layer, was taken to be stress-free rather than no-slip, leaving all other parameters and settings unchanged.

2.3.2 Numerical settings two-layer simulations

The two individual fluid layers of the two-layer simulation are subject to the same governing equations as the single layer, i.e.,

$$\frac{\partial \mathbf{v}_i}{\partial t} + (\mathbf{v}_i \cdot \nabla) \mathbf{v}_i = -\frac{1}{\rho_i} \nabla p_i + \nu_i \nabla^2 \mathbf{v}_i + \frac{1}{\rho_i} \mathbf{f}_i \quad \text{in } \mathcal{D}_i, \quad i = 1, 2 \quad (2.8)$$

complemented by $\nabla \cdot \mathbf{v}_i = 0$, where \mathbf{v}_i is the 3D velocity vector, p_i the pressure, ν_i the viscosity, ρ_i is the mass density, and \mathbf{f}_i the external body force in layer i . The subscript $i = 1$ in Eq. (2.8) refers to the top layer, and in the remainder subscript $i = 2$ will be used to indicate the bottom layer.

For the upper layer, the external body force \mathbf{f}_1 constitutes of the Lorentz force, which is given Eq. (2.6). The magnetic field is computed in the same way and the same matching criterion (maximum of the vertical vorticity component at $t = 1$ s) is used.

For the lower layer Eq. (2.8) is used, with $i = 2$. However, as in the two-layer fluid experiments, the fluid is only forced in the upper-layer, so that the external body force in this layer is $\mathbf{f}_2 = 0$.

The no-slip condition is used at the bottom and a rigid, stress-free condition at the free surface. At the internal interface, where the two sets of equations are coupled, kinematic boundary conditions are applied, dictating that the velocity components should be continuous over this interface ($u_1 = u_2$, $v_1 = v_2$, and $w_1 = w_2$), and besides it is assumed that the interface does not deform ($w_1 = w_2 = 0$). Furthermore, a dynamic boundary condition at this interface is applied, stating that the shear and normal stresses should be continuous over the internal interface [50], i.e.,

$$\rho_1 \nu_1 \frac{\partial v_1}{\partial z} = \rho_2 \nu_2 \frac{\partial v_2}{\partial z} \quad \text{and} \quad \rho_1 \nu_1 \frac{\partial u_1}{\partial z} = \rho_2 \nu_2 \frac{\partial u_2}{\partial z},$$

and

$$2\rho_1 \nu_1 \frac{\partial w_1}{\partial z} - p_1 = 2\rho_2 \nu_2 \frac{\partial w_2}{\partial z} - p_2,$$

respectively.

Note that the assumption of a non-deformable free surface and internal

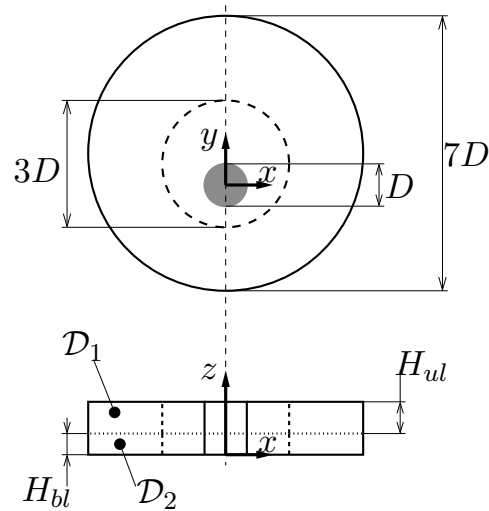


Figure 2.9 – Schematic top and side view of the computational domain used for the two-layer simulations. \mathcal{D}_1 and \mathcal{D}_2 refer to the top (having fluid height H_{ul}) and bottom layer (H_{bl}), respectively. The internal interface is indicated with the dotted line in the side view. Note that the vertical dimension of the computational domain is exaggerated for clarity of presentation.

interface represents a qualitative difference between the numerical simulations and the experiments, since in the latter case these surfaces are deformable. The possible effect of the rigid internal interface will be discussed in the results section. Implementation of a deformable internal interface is currently not feasible in the simulations.

The computational domain is built up in a similar way as was done for the single fluid layer case, together with the use of symmetry. A schematic of the computational domain is displayed in Fig. 2.9.

As a comparison, the 3D numerical simulation as described above is confronted with a numerical simulation of the 2D Navier-Stokes equation for the evolving dipolar vortex. In this 2D simulation the horizontal component of the Lorentz force present at mid-depth of the top-fluid layer was used to drive the fluid, and produces a dipole having approximately the same Reynolds number at the end of the forcing. In order to account for bottom friction, a linear friction term $-\alpha \mathbf{v}$ was added to the 2D Navier-Stokes equation with α the bottom friction coefficient and \mathbf{v} the horizontal velocity vector. The 2D computational domain (having zero thickness) is identical to the top view of Fig. 2.9. A comparison of tracer transport in

these 2D computations with transport in full 3D simulations is intended to illustrate the important effect of 3D recirculating flows on the dispersion of passive tracers at the free surface.

2.3.3 Numerical setup line of vortices

The numerical simulation of the linear array of vortices is based on the same equations as the dipole in a single-fluid layer, i.e., equations (2.4) to (2.6), although the Lorentz force \mathbf{f}_L is now computed for the present magnet arrangement.

For all these simulations, the free surface is taken to be rigid and stress-free and a no-slip condition applies at the bottom. Similar to the experiments, a continuous forcing that varies in time is utilised (see Sect. 2.2.3 for details). Furthermore, simulations were performed with and without lateral wall. Depending on the forcing and presence of the lateral wall, different computational domains were used.

In Fig. 2.10 the first computational domain is shown. Here, the left and

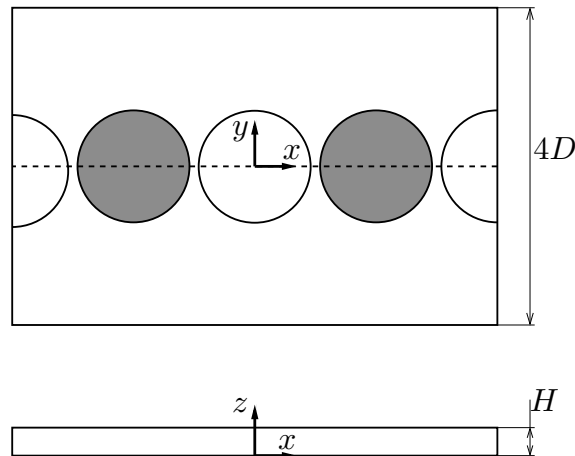


Figure 2.10 – Schematic top and side view of the computational domain used for the line of vortices simulations typically when the flow is dominated by viscosity. The magnet centred at the origin faces “North” upwards (indicated by white, “South” upwards by gray). The dashed line indicates the position of the lateral no-slip wall if present. Note that this drawing is not on scale.

right walls are taken stress-free, meaning that these boundaries are symme-

try boundaries. However, this is only permitted when there is no symmetry breaking with respect to $x = 0$, typically for cases where the forcing is with the lower electrical current strength (i.e., $a = 0$ and $b = 0.5$ A). The outer lateral walls at $y = \pm 3D$ are taken no-slip. For the simulations with a lateral wall present at $y = 0$, only the region $y > 0$ is used. Note that the symmetry with respect to $x = 0$ is not used to its full extent. A similar computational domain is used for the forcing case $a = 0$ and $b = 2.5$ A with a lateral wall present, although the domain in the y -direction spans from 0 to $4D$.

Symmetry breaking with respect to $x = 0$ occurs at higher Reynolds numbers as a result of the finiteness of the number of magnets. The outer magnets create dipolar vortices that propagate in an inward-curved direction. Therefore, the complete array is modelled consisting of 14 magnets as is the case in the laboratory experiments. In Fig. 2.11 the used computational domain is presented. All lateral (outer) side walls are no-slip

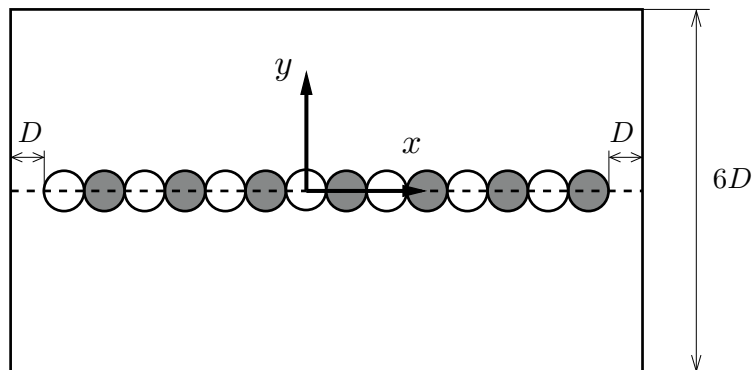


Figure 2.11 – Schematic top view of the computational domain used for the line of vortices simulations with strong forcing. The magnet facing “North” upwards are indicated by white, “South” upwards by gray. The dashed line indicates the position of the lateral no-slip wall if present.

boundaries. Note that, as in the experimental setup, a 1 mm spacing is between adjacent magnets and between the outer magnets and (left and right) side walls there is a gap of 25 mm (i.e., D). For the cases with a lateral wall present at $y = 0$, the no-slip condition is applied at this wall and only the domain where $y > 0$ is used. Typically, the domain depicted in Fig. 2.11 is used for the forcing case with $a = 0$ and $b = 2.5$ A (without lateral wall positioned on top of the magnets). For the forcing cases with a

offset ($a \neq 0$) a mean flow is introduced (in the y -direction), and a domain of a lower resolution is added at $|y| > 3D$.

To study the influence of 3D motion on the tracer transport, also 2D simulations were performed. The computational domains of these 2D simulations are identical to their 3D counterpart (see, e.g., Figs. 2.11 and 2.10), of course with zero thickness. The horizontal component of the Lorentz force present at mid-depth of the top-fluid layer was used to drive the fluid, leading to a similar Reynolds number as the 3D simulations. Furthermore, the influence of the bottom friction is accounted for by adding a linear damping term (“Rayleigh friction”) to the 2D Navier-Stokes equation, i.e., a contribution of $-\alpha\mathbf{v}$. The bottom friction coefficient is denoted by α and \mathbf{v} represents the horizontal velocity field.

The simulations are intended to mimic the experimental ones, with emphasis on the flow structures. These results will be presented in Chapter 5.

2.3.4 Passive tracer transport

To investigate the transport behaviour of passive particles, the numerically obtained velocity field is integrated in time. The position of a particle at time t^* is given by

$$\mathbf{x}(t^*) = \mathbf{x}_0 + \int_0^{t^*} \mathbf{v} dt, \quad (2.9)$$

where \mathbf{x}_0 is the initial particle position. Integration of (2.9) is performed numerically using a fourth-order Runge-Kutta method.

For the 2D simulations, the numerically obtained 2D velocity field is integrated in time with Eq. (2.9). When releasing particles on the free surface for the 3D simulations, basically a 2D tracking of these particles is performed as the vertical velocity component w is identical zero at the free surface. The difference, however, is that the velocity field of the 2D simulation is divergence-free as opposed to the horizontal velocity field at the free surface obtained with the 3D simulation. When the particles are not released at the surface, in the 3D simulations a genuine 3D tracking is performed, i.e., integration of Eq. (2.9) with the 3D velocity field.

For the two-layer dipole simulation (as well as the corresponding 2D simulation), the particles are only released at $t = 0$ on a spatially uniform grid (consisting of several thousands of particles) at the free surface, where $w = 0$.

For the (3D) linear array of vortices simulations, particles are released on the free surface and on a horizontal plane inside the fluid layer. Furthermore, the dispersion of particles periodically released at the lateral wall is studied. Further details are presented in the corresponding chapters.

CHAPTER 3

The dipolar vortex in a shallow fluid layer

Many experiments have been performed in electromagnetically driven shallow fluid layers to study quasi-two-dimensional (Q2D) turbulence, the shallowness of the layer commonly being assumed to ensure Q2D dynamics. This chapterⁱ reports on a detailed study of the vertical motions developing in shallow-layer flows. For this purpose, one of the most elementary vortex structures in 2D turbulence is studied, the dipolar vortex, in a non-rotating homogeneous shallow fluid layer. Stereoscopic Particle Image Velocimetry (SPIV) has been used for an experimental investigation of the flow, providing all three velocity components simultaneously in a horizontal plane inside the fluid. Additionally, 3D numerical simulations are carried out, which easily allow inclusion of different boundary and initial conditions, and which provide the full 3D velocity and vorticity fields over the entire flow domain.

The results indicate significant three-dimensionality of the shallow fluid flow and the remarkably complex and non-trivial 3D structure of the dipole, both during and after the forcing stage. In order to quantify deviations from 2D or Q2D flow behaviour, the flow evolution is analysed by adopting the ratio of “horizontal” and “vertical” kinetic energies (being the kinetic en-

ⁱThis chapter is to a large extent based on two papers [2, 3], i.e. R.A.D. Akkermans, A.R. Cieslik, L.P.J. Kamp, R.R. Trieling, H.J.H. Clercx and G.J.F. van Heijst, “The three-dimensional structure of an electromagnetically generated dipolar vortex in a shallow fluid layer,” *Phys. Fluids* (2008) and R.A.D. Akkermans, L.P.J. Kamp, H.J.H. Clercx and G.J.F. van Heijst, “Intrinsic three-dimensionality in electromagnetically driven shallow flows,” *Europhys. Lett.* (2008).

ergy associated with the horizontal and vertical fluid velocity components, respectively) and the normalized horizontal divergence. Besides, the deviation from a Poiseuille-like profile is investigated for decreasing fluid depth.

This chapter is organized as follows: Sec. 3.2 presents the experimental and numerical details. The experimental and numerical results of the dipole evolution during and after the forcing are then presented in Sec. 3.3. Additional simulations are discussed in which different boundary and initial conditions were applied in order to examine the influence of bottom friction, electromagnetic forcing, and initialization on the 3D motions. Based on the laboratory experiments and numerical simulations with no-slip bottom, three quantities are evaluated that could be used as criteria for the degree of two-dimensionality of the flow. Finally, in Sec. 3.4 the results are discussed and the conclusions are summarized.

3.1 Introduction

In order to validate theory on two-dimensional (2D) turbulence many investigators have performed laboratory experiments in, e.g., rotating fluids [94], in stratified fluids [58], and in shallow (non-stratified) fluid layers [20, 24, 26, 84, 88]. In the latter case it is commonly assumed that these shallow flows behave in a two-dimensional fashion when the vertical length scale \mathcal{H} is much smaller than the horizontal length scale \mathcal{L} . The rationale behind this thin-layer configuration is that although vertical three-dimensional (3D) motions are present, their magnitude, assumed to be proportional to \mathcal{H}/\mathcal{L} , is much smaller than the dominant (2D) horizontal flow speeds. Moreover, the effect of bottom friction can be parameterized by adding a linear friction term $-\alpha\mathbf{v}_H$ to the 2D Navier-Stokes equation (usually referred to as “Rayleigh friction”), under the assumption of a Poiseuille-like profile in the vertical direction. Here α represents the bottom friction coefficient and \mathbf{v}_H the local depth-averaged horizontal fluid velocity (see, e.g., [38]). This thin-layer configuration has been applied in flowing soap film experiments [22, 46, 72, 76] and shallow fluid experiments [20, 24, 26, 84, 88]. In some experiments a single fluid layer is utilized, see [20, 24, 26, 84, 88], while in the investigations of Boffetta *et al.* [10], Shats *et al.* [80], Rivera and Ecke [73], or Tabeling and co-workers [67, 68] a stable two-layer stratification has been used. Although slightly different flow forcing was applied in each of these experimental studies, these studies all use the two-layer system to provide an additional mechanism to inhibit vertical motions and to minimize the

influence of bottom friction, which is predominantly present in the lower layer.

Just as the ordinary Reynolds number $\text{Re} (= \mathcal{U}\mathcal{L}/\nu)$ expresses the relative importance of lateral diffusion with respect to nonlinear processes, one can define an alternative Reynolds number $\text{Re}_\alpha (= \mathcal{U}/\alpha\mathcal{L})$ based on the influence of the bottom friction [26]. Here, \mathcal{U} denotes a characteristic velocity, \mathcal{L} a typical horizontal length scale and ν the viscosity, while the bottom friction coefficient α is given by $\alpha = \nu(\pi/2\mathcal{H})^2$, under the assumption of a Poiseuille-like flow in the vertical. The ratio $\text{Re}_\alpha/\text{Re}$ expresses the relative importance of the bottom friction to the horizontal diffusion. In the case $\text{Re}_\alpha/\text{Re} \ll 1$ [or equivalently $(2\mathcal{H}/\pi\mathcal{L})^2 \ll 1$] the flow is considered to be dominated by bottom friction effects.

The linear friction term is non-selective with respect to length scales, provided that this friction is not too small, it will therefore prevent the pile-up of energy at length scales corresponding to the box size (and is for this reason often used in numerical studies of 2D turbulence [8, 9]). As opposed to this linear friction, the “internal” viscous dissipation predominantly removes energy at the smallest scales. However, in the review paper of Danilov and Gurarie [25] it is argued that the influence of bottom friction can be parameterized only in a qualitative sense in the form of Rayleigh damping. Furthermore, these shallow fluid flows are (vertically) bounded by a no-slip bottom and a free surface, and therefore possess a 3D structure due to the shear in the vertical. This shear may lead to significant secondary circulations, see, e.g., Satijn *et al.* [77] where this is numerically investigated for a monopolar vortex.

Apart from the influence of the bottom boundary layer, the flow forcing mechanism could also act as an additional source of vertical motion. In some experiments a magnetic field is used to force an electrolyte fluid through which an electric current flows. It is then the Lorentz force, resulting from the interaction of the current density and the magnetic field, that drives the flow. However, this magnetic field decays over a limited vertical distance and the forcing will therefore vary with height. In addition to its horizontal component, the Lorentz force also has a vertical component, whose effect on the flow generation has yet to be determined. The consequences of the spatial non-uniformities in the electromagnetic forcing and the vertical component of the Lorentz force are especially of interest for electromagnetically forced shallow flows.

The above described assumptions on the behaviour of a flow in a shallow

Table I – Experimental parameter values for the SPIV measurements: total fluid depth H , measurement level h_{ls} , electrical current I , current density j_x , and ratio vertical/horizontal Reynolds numbers. The same parameter values are used for the numerical simulations.

H (mm)	h_{ls} (mm)	I (A)	j_x (A/cm ²) ^a	Re_α/Re (-)
6.0	2.0; 3.5	2.4; 3.7	0.08; 0.12	0.02
9.3 ^b	2.0; 5.0; 9.0	2.4; 4.4 ^b ; 5.4	0.05; 0.09; 0.11	0.06
11.4	2.0; 5.0; 9.0; 10.0	2.4; 4.4; 6.4	0.04; 0.07; 0.11	0.08

^aDue to an unfortunate typing error the reported values of j_x in [2] are a factor 10 too high (fortunately, this typing error has no consequences for the experimental and numerical results in [2]). The here presented values are correct.

^bResults of this experimental (and numerical) case, i.e., $H = 9.3$ mm and $I = 4.4$ A, presented in Sects. 3.3.1 and 3.3.2 are indicative for all the other cases.

fluid layer have never been verified accurately. Notable exceptions are the numerical investigation by Satijn *et al.* [77] concerning a decaying monopole in shallow fluid layers or the experimental study of a dipolar vortex by Lin *et al.* [54].

3.2 Details of experiments and simulations

The experimental setup used for the investigation of the dipolar vortex in a shallow flow was already presented in Chapter 2, together with the way this dipole is generated. In this section the performed experiments will be detailed, as well as additional information concerning the numerical simulations is given. Several experiments were performed with different fluid depths H and electrical current strength I to investigate the influence of these variables on the three dimensionality.

Table I provides an overview of the performed experiments. In this chapter results are presented mainly for a fluid depth $H = 9.3$ mm and a forcing protocol consisting of a single 1 s constant-current pulse of $I = 4.4$ A (see Table I). It is stressed that the results for this case are indicative for all the other fluid layer depths and forcing protocols. Measurements were performed at several levels h_{ls} inside the different fluid depths. Time t was set to zero at the onset of forcing for all the experiments.

By changing the fluid depth H and forcing current I we effectively change the Re_α -value and initial Re -value, respectively. Note that the current density j_x is a measure of the forcing strength. This current density

is computed as the electrical current I divided by the cross-sectional area, which equals $H \cdot L_{tank}$ (the tank width L_{tank} being 52 cm). The last column of Table I presents values of the quantity $\text{Re}_\alpha/\text{Re}$, or equivalently $(2\mathcal{H}/\pi\mathcal{L})^2$, where the magnet diameter and fluid depth were taken as measures of the characteristic horizontal and vertical length scales, respectively. The small values of the ratio $\text{Re}_\alpha/\text{Re}$ indicate that all experiments are dominated by bottom friction effects.

Note that the Reynolds number Re based on the maximum horizontal velocity \mathcal{U} at the end of the forcing period (forcing current strength $I = 4.4$ A) measured approximately 1400. The Reynolds number based on the bottom friction coefficient for this case equals approximately 75. In the regime diagram of Satijn *et al.* (see Fig. 6 in [77]) this $(\text{Re}_\alpha/\text{Re})$ combination lies outside the Q2D regime (note that their diagram is for a monopole). However, as noted before, the results presented for this case, i.e., $H = 9.3$ mm and $I = 4.4$ A are representative of the other fluid layer depths and forcing strengths.

Various numerical simulations have been performed, which can broadly be categorized in two parts. In all runs the upper free-surface was taken to be stress-free and flat. The latter implies that the generation of surface gravity waves is excluded in the numerical simulations. The first set of runs were aimed to simulate the experimental results. For that purpose a no-slip boundary condition was imposed at the bottom of the computational domain. In order to examine how the bottom boundary layer at a no-slip bottom is related to the 3D flow structures found numerically, a second set of simulations has been performed. In these runs the bottom, just like the upper surface of the fluid layer, was taken to be stress-free rather than no-slip, leaving all other parameters and settings unchanged. Furthermore, simulations were performed with (artificial) different initial conditions to study the influence of the electromagnetic forcing on the dipole evolution. For the numerical details the reader is referred to Chapter 2.

3.3 Experimental and numerical results

3.3.1 The generation and evolution of the dipolar vortex

In this subsection results for the case of a fluid depth $H = 9.3$ mm and electrical current $I = 4.4$ A (see Table I) are presented, as the flow evolution of

this case is indicative for all the other fluid depths and forcing strengths.

Figure 3.1 shows plots of the instantaneous vertical (shades/colours) and horizontal (vectors) velocities in a horizontal cross-sectional plane at 5 mm above the bottom. For clarity of representation the vectors are under-sampled: only every third vector is shown in the x - and in the y -direction, so that (approximately) only 11% of the total set is shown. The disk-shaped magnet (indicated by the circle) is centred at $(x, y) = (0, 0)$. The left column of figures shows experimental results at three instances of time and the right column shows numerically obtained results at the same times. Since the total forcing time $\Delta t = 1$ s and the forcing is started at $t = 0$, Figs. 3.1(a,d) and 3.1(b,e) correspond to the mid-stage ($t = 0.5$ s) and to the final stage ($t = 0.96$ s) of the forcing, while Figs. 3.1(c,f) show snapshots of the flow field 0.5 s after the forcing has stopped.

As can be seen in Fig. 3.1(a), two regions of downward flow have developed in the two vortex cores. At the late stage of the forcing [see Fig. 3.1(b)], these regions of downward flow are still present inside the vortices, while upward motion is observed at the tail of the dipole. During the entire forcing phase, a build-up of downward motion is seen inside the vortices. Comparison of the numerical simulation results shown in Figs. 3.1(d,e) with Figs. 3.1(a,b) reveals a striking resemblance, although the upward motion at the tail side found in the simulations is not so clearly visible in the experimental result shown in Fig. 3.1(b). It should be noted that the downwelling in both vortex cores is not driven directly by the vertical component of the Lorentz force, but can be understood as follows.

From the numerical simulations it is observed that the initial (linear) flow evolution is governed by a magneto-hydrostatic balance between the vertical component of the Lorentz force and the vertical pressure gradient. This balance is described by

$$\frac{\partial p}{\partial z} = \mathbf{f}_L \cdot \mathbf{e}_z = j_0 \mathbf{B} \cdot \mathbf{e}_y = j_0 B_y. \quad (3.1)$$

Since the magnet is circular and assumed to be axially symmetric, the right-hand-side of this balance can also be written as

$$j_0 B_y = j_0 \sin \varphi B_r = -j_0 \sin \varphi \frac{\partial A_\varphi}{\partial z}, \quad (3.2)$$

where cylindrical coordinates (r, φ, z) have been introduced. A_φ is the azimuthal component of the vector potential \mathbf{A} for the magnet's magnetic

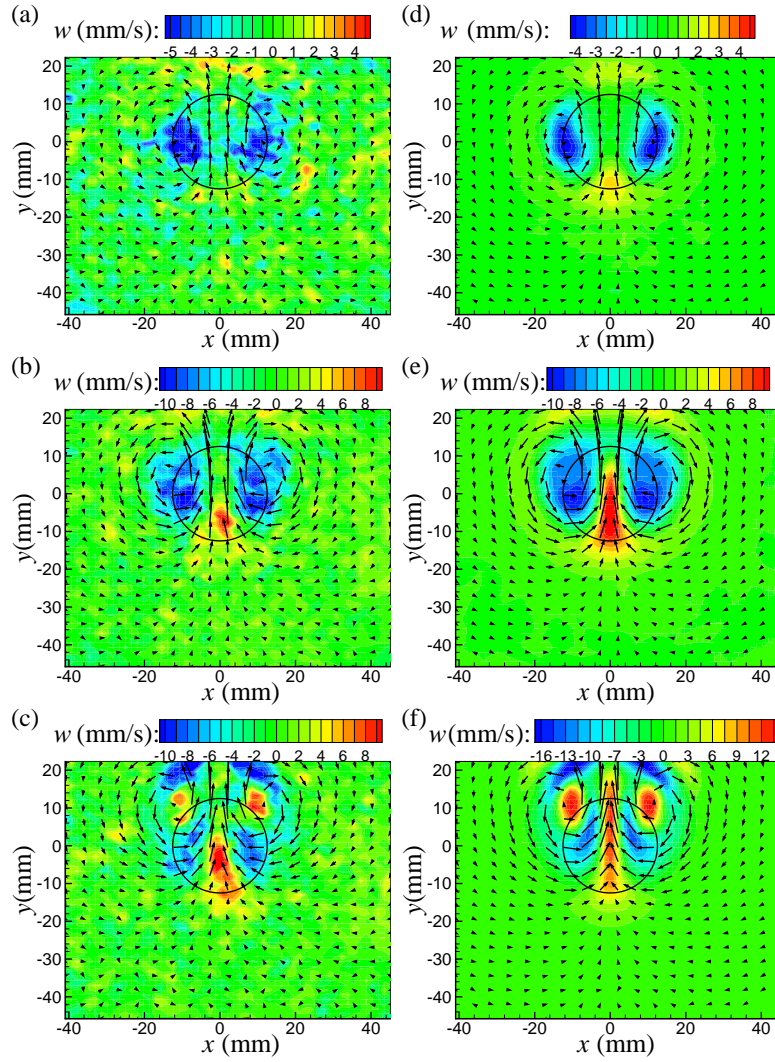


Figure 3.1 – Instantaneous velocity fields of a dipolar vortex in a horizontal plane at $z = 5$ mm (see Table I for the experimental and numerical parameters). Vectors represent horizontal velocity components and shades/colours indicate the magnitude of the vertical velocity. The circle denotes the position of the disk-shaped magnet. Experimental results obtained with SPIV at (a) $t = 0.50$ s, (b) $t = 0.96$ s, and (c) $t = 1.50$ s. Numerical results at (d) $t = 0.50$ s, (e) $t = 0.96$ s, and (f) $t = 1.50$ s.

field, $\mathbf{B} = \nabla \times \mathbf{A}$.

Integrating Eq. (3.1) with respect to z using (3.2) yields

$$p = -j_0 \sin \varphi A_\varphi(r, z) + C(r, \varphi), \quad (3.3)$$

where $r = \sqrt{x^2 + y^2}$.

It is easily verified from (2.4), keeping in mind that inside the fluid (i.e., outside of the permanent magnet) the magnetic field is curl-free, that the pressure needs to satisfy Laplace's equation in the initial (linear) regime that we are considering here. Moreover, the integration “constant” $C(r, \varphi)$ must satisfy

$$\nabla^2 C = \nabla^2(j_0 \sin \varphi A_\varphi) = 0. \quad (3.4)$$

Since $C(r, \varphi) \rightarrow 0$ as r approaches infinity, the solution is $C(r, \varphi) \equiv 0$.

From the above we conclude that in the very beginning of the forcing phase, the spatial pressure distribution inside the fluid is not yet governed by dynamical effects but completely determined by the spatial structure of the magnetic field that permeates the fluid, i.e.,

$$p(x, y, z, t) \propto p_0 = -j_0 \frac{y}{r} A_\varphi(r, z), \quad \text{for } t \downarrow 0. \quad (3.5)$$

The latter equation implies that the vertical component of the Lorentz force does not drive the flow in the initial period when the electromagnetic forcing is active.

Whilst the magnitude of the horizontal flow velocities gradually increases during the forcing, a cyclostrophic balance between the horizontal pressure gradient and the centrifugal force in both swirls is established. Due to the stronger forcing close to the magnet the swirl is strongest close to the bottom, implying a vertical pressure gradient along the vortex axes in the positive z -direction. As a result, the initial magneto-hydrostatic balance [see Eq. (3.5)] in each of the two vortex cores is gradually distorted by additional vertical pressure gradients that start to drive a downward motion in both swirls during the whole forcing phase, as is observed in Figs. 3.1(a,b) as well as in Figs. 3.1(d,e).

Figure 3.1(c) [or 3.1(f)] shows a snapshot of the experimentally (numerically) observed flow field 0.5 s after the forcing has stopped. Comparison with Fig. 3.1(b) [or 3.1(e)] reveals an essentially different flow distribution. One now observes well-defined upward motion in the vortex cores surrounded by downwelling similar to the secondary circulation observed

in a single monopolar vortex [77]. This upward motion appears shortly after the forcing has stopped. In the monopolar vortex case the emergence of secondary circulation is driven by the interaction with the viscous boundary layer at the bottom. Although this mechanism is also working in the dipolar vortex case, it cannot explain the velocity magnitude observed. Estimation of the vertical velocity based on the Bödewadt flow model (see, e.g., [6, 36]) leads to a typical vertical velocity of 4 mm/s, whereas from Fig. 3.1(c) we read a substantially larger velocity of approximately 10 mm/s. This difference suggests a relaxation of the flow after the forcing phase that has a different origin than linear bottom friction. This questions the use of linear friction to model the influence of the bottom in 2D turbulence simulations, as this relaxation is not a bottom friction effect. The mechanism of this relaxation will be discussed in more detail later in this section.

Figures 3.2(a)-(c) display three numerically obtained snapshots of the vertical vorticity ω_z at the same time instants as Figs. 3.1(d)-(f), and evaluated at 5 mm above the bottom. In these figures oppositely signed vorticity patches are observed, characteristic for a 2D dipolar vortex. Initially, these vorticity patches have a kidney shape, typical for the magnetic field produced by a cylindrical magnet. This kidney-like shape becomes less pronounced for later times and for larger vertical distances from the magnet.

To make a more quantitative comparison between experiment and numerical simulation, vorticity profiles of ω_z are displayed in Fig. 3.3 for the same time instances as in Fig. 3.2. In general a good quantitative agreement between the experimental and numerical results is seen. Figure 3.3(c) shows the development of small-scale structures in the numerically obtained vorticity. This fragmentation of vorticity becomes more pronounced at later stages of the evolution. These regions of high gradients in the vorticity are less well reproduced by the experiments due to the spatial averaging effect of the cross-correlation by the SPIV technique.

In order to observe the evolution of the dipole after the forcing has been switched off, the field of view is shifted in the positive y -direction (i.e., the upper dashed rectangle in Fig. 2.4). Figure 3.4 shows plots of instantaneous velocities in a horizontal cross-section 5 mm above the bottom at $t = 1.50$ s, $t = 2.00$ s, and $t = 2.60$ s. The left column displays experimentally obtained velocity fields and the right column shows the velocity field obtained numerically. The meaning of the shades/colours and vectors is the same as in Fig. 3.1.

After the electromagnetic forcing has stopped, one observes the appear-

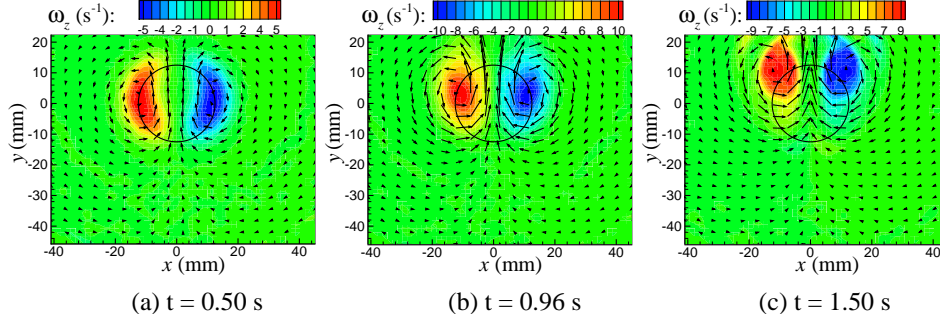


Figure 3.2 – Snapshots of the numerically simulated flow evolution, showing the horizontal velocity components (vectors) and the vertical vorticity component ω_z (magnitude indicated by shades/colours) in the horizontal plane at $z = 5$ mm. The circle indicates the position of the disk-shaped magnet. Snapshots taken at (a) $t = 0.50$ s, (b) $t = 0.96$ s, and (c) $t = 1.50$ s.

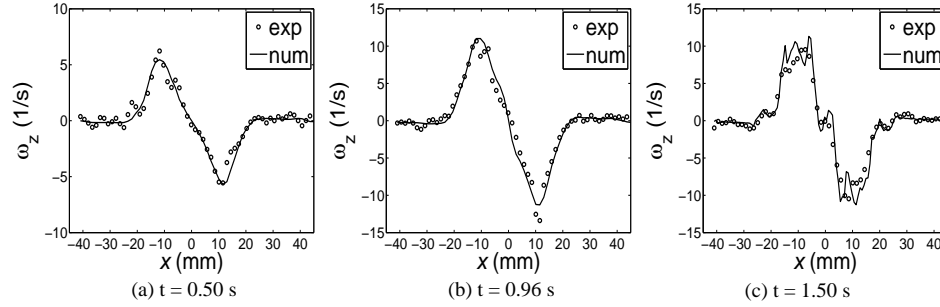


Figure 3.3 – Comparison of experimental (open circles) and numerical (solid line) vorticity profiles at (a) $t = 0.50$ s and $y = 0$ mm, (b) $t = 0.96$ s and $y = 3$ mm, and (c) $t = 1.50$ s and $y = 11$ mm. The profiles are evaluated at height $z = 5$ mm above the bottom.

ance of well-defined upward motion in the two vortex cores, surrounded by bands of negative vertical velocity, as seen in Fig. 3.4(a). Although these 3D motions are quite similar to the secondary circulation seen in the monopolar vortex [77], as stated before, the driving mechanism is quite different, i.e., the upwelling is not driven by a viscous boundary layer at the bottom. This can be understood as follows.

In absence of forcing, no swirl is maintained in the lower part of the fluid layer. The continuing down-flow and related outflow at the base of the two vortex cores will then, in contrast to the forced case, rapidly reduce the vertical vorticity ω_z close to the bottom. This is basically due to conservation of angular momentum rv_θ : the swirl velocity v_θ of the radi-

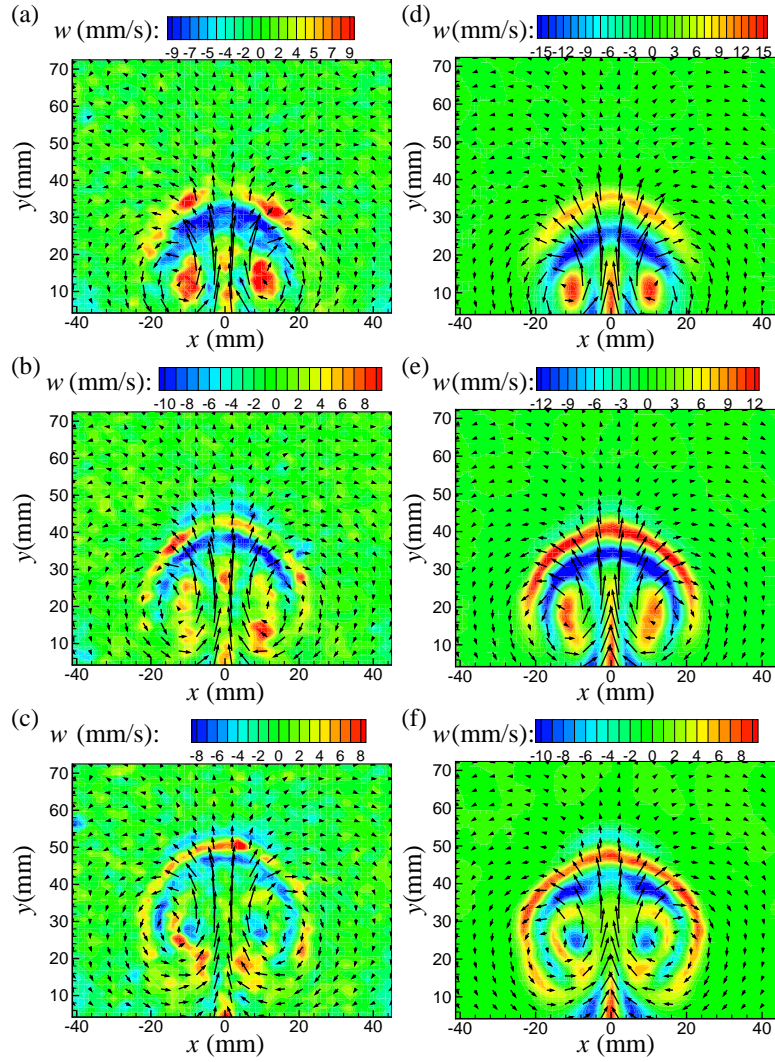


Figure 3.4 – Instantaneous velocity fields of a dipolar vortex, evaluated in the horizontal plane at $z = 5$ mm above the bottom, during post-forcing phase (see Table I for the experimental and numerical parameters). Meaning of vectors and shades/colours: see caption Fig. 3.1. Experimental results at (a) $t = 1.50$ s, (b) $t = 2.00$ s, and (c) $t = 2.60$ s. Snapshots of numerical simulation at (d) $t = 1.50$ s, (e) $t = 2.00$ s, and (f) $t = 2.60$ s.

ally spreading fluid decreases. The experiments and simulations indicate that this spin-down (as seen in the kinetic energy of the horizontal mo-

tion) occurs on a much shorter time scale (approximately 1.5 s) than the typical bottom friction time scale τ_E ($= \frac{2\mathcal{H}^2}{\pi^2\nu}$, here equal to approximately 18 s). The cyclostrophic balance then dictates an increase of the pressure in the vortex core near the bottom, while no significant pressure change is expected near the free-surface. Eventually, the axial pressure gradient in the vortices is even reversed, resulting in a deceleration of the down-flow and actually leading to an upward flow, as is seen in Fig. 3.4(a). Note that this phenomenon is independent of viscosity but is a consequence of the vertical confinement of the flow. The minor importance of bottom friction was already hinted at before, where it appeared that the Bödewadt model substantially underestimated the magnitude of this upward motion.

Besides this complex 3D motion, upward motion at the plane of symmetry of the dipole, and significant negative vertical motion at the front of the dipole are observed. For example, in the region of strong downward motion the vertical velocity turns out to be of the order 25% of the horizontal velocity. At the front of the dipole one observes a feature referred to by Sous *et al.* [85,86] as “frontal circulation”, i.e., a roll-like flow structure with upward motion at the front of the dipole and a weaker downward motion in front of that [see Figs. 3.4(b) and (c)]. Note that Lin *et al.* [54] (who were, to our knowledge, the first to report on this feature) and Sous *et al.* [85,86] did not use the electromagnetic forcing method, but their dipoles were created by injecting a small amount of fluid horizontally in the tank.

As time progresses one observes an oscillating motion of the vertical velocity component inside the two vortex cores. This is illustrated in Fig. 3.4(c), where the emergence of oppositely signed vertical motion is seen inside the individual vortex cores as compared to Fig. 3.4(a). These oscillations are interpreted to be of inertial origin [75] and resulting from an overshoot of the decelerated upwelling described above. Typically, two to three oscillations are seen in both the experiments and the simulations, depending on the forcing strength. These inertial oscillations were further studied for the monopolar vortex case by Duran-Matute *et al.* [28].

Comparison of the numerically obtained Figs. 3.4(d,f) with Figs. 3.4(a,c) reveals a striking resemblance, although the upward motion at the tail side found in the simulations is not so clearly visible in the experimental result. From this resemblance one can conclude that free-surface effects (through surface gravity waves) are of minor importance in generating vertical motions in the laboratory experiments. In the laboratory experiments surface deformations are present, such as the dimple on the free surface in the

vortex core, whereas the generation of surface gravity waves is excluded in the numerical simulations (the surface is not allowed to deform). One can also estimate the phase speed c of a surface gravity wave in a shallow fluid layer, see, e.g., [50]. The phase velocity of a surface gravity wave equals $c = \sqrt{\frac{g\lambda}{2\pi} \tanh(\frac{2\pi H}{\lambda})}$, where g is the gravitational acceleration, λ the wavelength, and H the fluid depth. Taking for the wavelength λ the magnet diameter D as a characteristic horizontal length scale, one obtains a phase speed c of 23 cm/s, which is much larger than the fluid velocities. Surface tension can be neglected as the wavelength λ is larger than the wavelength λ_{cr} for which surface tension σ becomes important, i.e., $\lambda_{cr} = 2\pi \sqrt{\sigma/(\Delta\rho g)}$ (where $\Delta\rho = \rho_f - \rho_{air}$). For an air-water interface λ_{cr} equals 1.6 cm.

To summarize, the necessary condition for the occurrence of the dynamical flow behaviour inside the dipolar vortex as discussed above is a z -dependence of the vertical vorticity component, i.e., $\omega_z = f(z)$. This condition can be understood in the following way. When ω_z is a function of the vertical coordinate, the cyclostrophic balance dictates that the pressure p must also vary with z . This vertical pressure gradient will drive a vertical motion. In general, any z -variation in the vertical vorticity, as a result of the forcing and/or dictated by boundary conditions, will lead to vertical motions.

3.3.2 The structure of the dipole: stagnation points and horizontal vorticity rolls

Figures 3.5(a)-(c) present numerically obtained distributions of the z -component of the vorticity for the same three instances of time as in Figs. 3.4(d)-(f). For $t = 1.50$ s, i.e., 0.5 s after the forcing has been stopped, Fig. 3.5(a) shows two coherent, symmetrical patches of oppositely signed vorticity. Moreover, one observes weak bands of vorticity at the locations of the frontal circulation band. As time progresses, an increasing fragmentation of the vorticity in Figs 3.5(b) and 3.5(c) is seen, as was also observed by Lin *et al.* [54]. This fragmentation is most pronounced near the free-surface. Comparison of Figs. 3.5(c) and 3.4(f) reveals a correlation between the increased magnitudes of ω_z vorticity and vertical motion w , i.e., where $\nabla_H \cdot \mathbf{v} \neq 0$. Due to conservation of angular momentum rv_θ , increased (decreased) magnitude of vertical vorticity is expected at region where the horizontal flow field is converging (diverging). The fragmentation of ω_z is thus directly re-

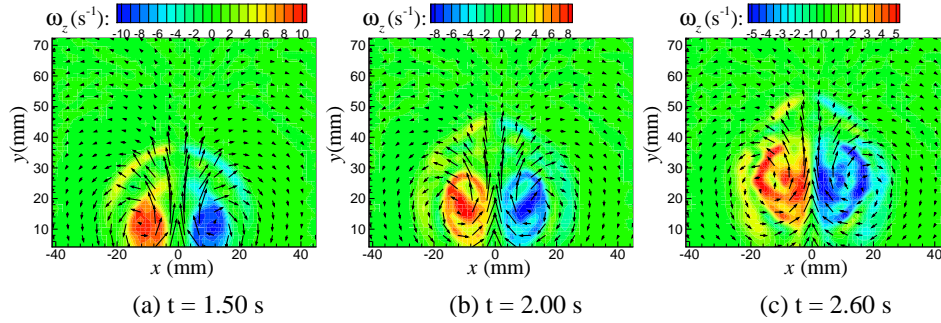


Figure 3.5 – Numerically observed evolution of the vertical vorticity ω_z at $z = 5$ mm (see Table I for the numerical parameters). Meaning of vectors and shades/colours: see caption of Fig. 3.2. Numerical snapshots at (a) $t = 1.50$ s, (b) $t = 2.00$ s, and (c) $t = 2.60$ s.

lated with the 3D structure of the flow field.

To investigate the vertical flow structures at the front and tail side of the dipolar vortex, the numerically obtained instantaneous flowline patternⁱⁱ for the horizontal flow field $\mathbf{v}_H = (u, v)$ at mid-depth and in a reference frame that is co-moving is shown in Fig. 3.6. In this figure spiraling flowlines are seen inside the individual vortex cores, inward or outward depending on the net in- or outflux (i.e., on the sign of $\partial w/\partial z$) at the specific evaluation height. Furthermore, at the front and tail of the dipole two hyperbolic points can be identified. It is found that these points coincide with regions of significant vertical motion. Remarkable is that the band of the upward motion in the frontal circulation structure delineates the instantaneous “separatrix” that is associated with the frontal stagnation point. The separatrix is not closed at the rear of the dipole, implying advection of fluid out of the dipole into the tail. This is directly associated with the fluid entering this midplane near the vortex cores, as is evident from the locally spiral-shaped flowlines. Regions of upwelling flow are observed near the frontal and rear (hyperbolic) stagnation points. The elongated shape of these regions is directly linked with the orientation of the flowlines near these hyperbolic points.

Figure 3.7(a) shows a numerically obtained distribution of the y -component of the vorticity (ω_y) in a vertical slice approximately through the

ⁱⁱInstantaneous flowlines are defined here as curves of which the tangent directions indicate the direction of the horizontal component of the 3D flow velocity vector at some z -level and for some fixed time instant. Since this horizontal part of the flow field does not constitute an incompressible flow, these lines are not streamlines.

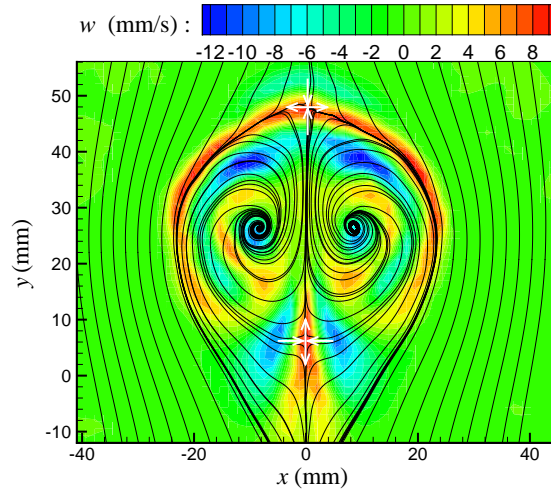


Figure 3.6 – Numerically obtained flowlines for $t = 2.60$ s at mid-depth of the 9.3 mm fluid layer (see Table I for the numerical parameters). Shades/colours indicate the magnitude of vertical velocity component. Arrows at the two hyperbolic points indicate the directions of advection.

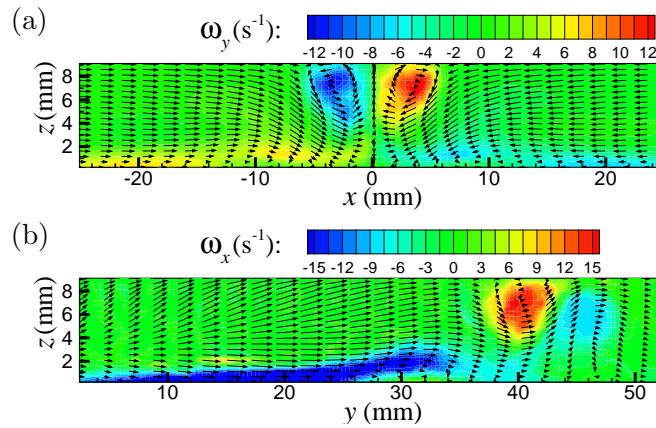


Figure 3.7 – (a) Vertical slice ($y = 6.0$ mm for $t = 2.60$ s) of the numerically obtained distribution of the ω_y vorticity component. The shades/colours indicates the magnitude of ω_y , while the vectors represent the flow in the xz -plane. (b) Vertical slice through the symmetry plane of the dipole ($x = 0$) at time $t = 2.60$ s showing the ω_x distribution (shades/colour) with vectors representing the flow in the yz -plane.

instantaneous stagnation point at the tail of the dipole, i.e., $y = 6.0$ mm for $t = 2.60$ s. Clearly visible are two vortical structures which are associated with the up- and downwelling close to this hyperbolic point [see Fig. 3.6]. The magnitude of the vorticity component ω_y in this (co-moving) vertical slice turns out to evolve to significantly larger values than that of the “primary” vorticity component ω_z . In Fig. 3.7(b) the frontal circulation is seen in front of the dipole indicated by the negative ω_x , which originates from the bottom boundary layer. Furthermore, a spanwise vortex with high (positive) spanwise vorticity is seen.

To further illustrate the 3D structure inside the vortices during and after the forcing phase, the velocity distribution in a vertical slice defined by the plane $x = -12.5$ mm is displayed in Fig. 3.8 for $t = 0.50$ s, $t = 0.96$ s, $t = 1.50$ s, $t = 2.00$ s, and $t = 2.60$ s. Here vectors represent the v - and w -velocity components. The magnitude of the vertical velocity component w has also been indicated by shades/colours. The vertical plane defined by $x = -12.5$ mm is chosen such that it cuts approximately through one of the vortex cores. Figures 3.8(a)-(b) clearly illustrate the buildup of downward motion inside the vortex core, located around $y = 0$, during the forcing phase. For $t = 0.96$ s it is seen that a large recirculation cell is present inside the vortex, with the largest downward motion located near the axis of the vortex at $y = 0$. Shortly after the forcing has stopped [see Fig. 3.8(c)], a reversal of the vertical velocity just inside the vortex core is observed, i.e., upward motion at approximately $y = 10$ mm [cf. Fig. 3.4(d)]. Figures 3.8(c)-(e) illustrate the complex flow motion in the vertical slice, which persists after the forcing has been switched off. The second reversal of the vertical velocity is only weakly visible (approximately at $y = 26$ mm) in Fig. 3.8(e) as the slice $x = -12.5$ mm barely touches the region where this second reversal takes place [see Fig. 3.4(d)]. Clearly, in view of the vertical structure of the flow field both during the forcing phase and during the post-forcing phase, the flow does not behave as a quasi-2D flow, i.e., planar flow with a Poiseuille-like vertical structure. The emergence of these significant 3D structures during the forcing phase raises serious questions regarding the use of electromagnetic forcing in a shallow fluid flow to study forced Q2D turbulence.

3.3.3 Alternative initial and boundary conditions

As argued above, the no-slip boundary is not a necessary condition for the 3D structure of the dipolar vortex and its subsequent evolution. To sub-

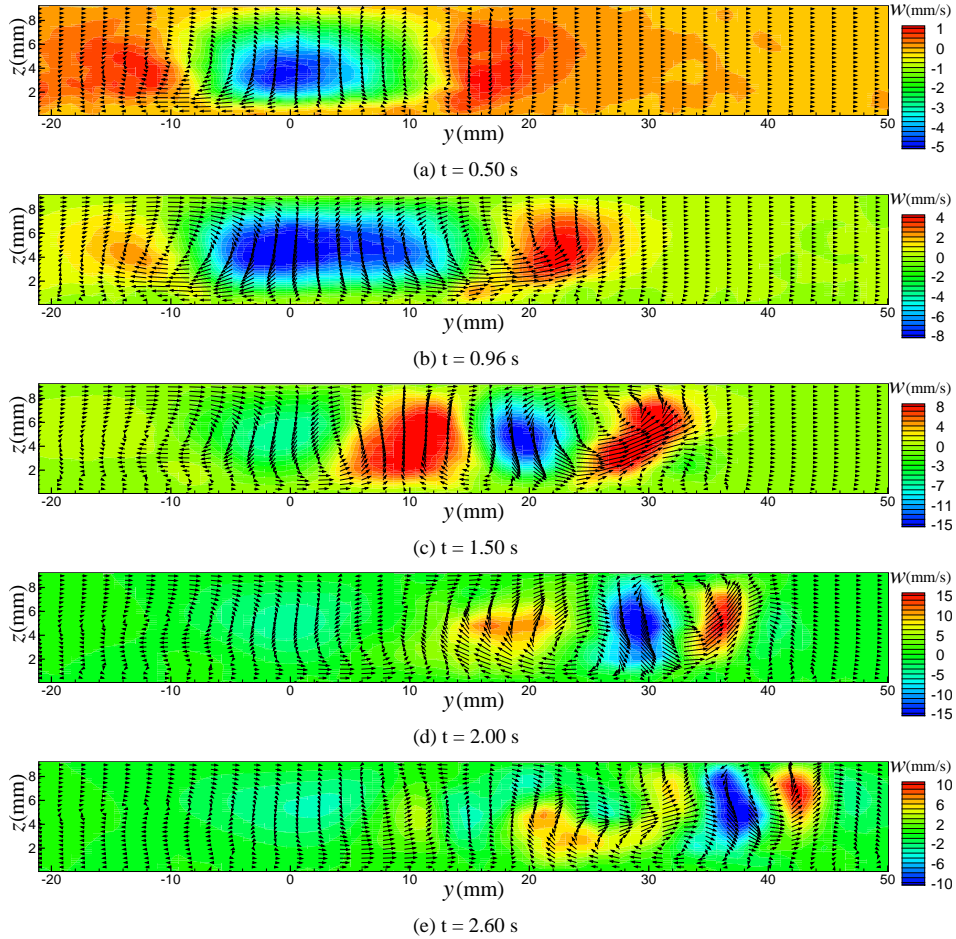


Figure 3.8 – (Colour online) Numerically obtained snapshots of vertical slice of the plane $x = -12.5$ mm at (a) $t = 0.50$ s, (b) $t = 0.96$ s, (c) $t = 1.50$ s, (d) $t = 2.00$ s, and (e) $t = 2.60$ s (see Table I for the numerical parameters). Vectors represent the v - and w -velocity components, while shades/colours indicate the magnitude of the vertical velocity w .

stantiate this, Figs. 3.9(a)-(c) and Fig. 3.10 display numerically calculated velocity fields where the bottom and the free surface are both taken to be stress-free, leaving all other parameters and settings unchanged. Comparing Figs. 3.9(a)-(c) and Fig. 3.10 with the corresponding results in the previous subsection (with a no-slip bottom), one observes that the spatial and temporal evolution of the flow is qualitatively the same except the frontal circulation is not present. This frontal circulation does seem to be depen-

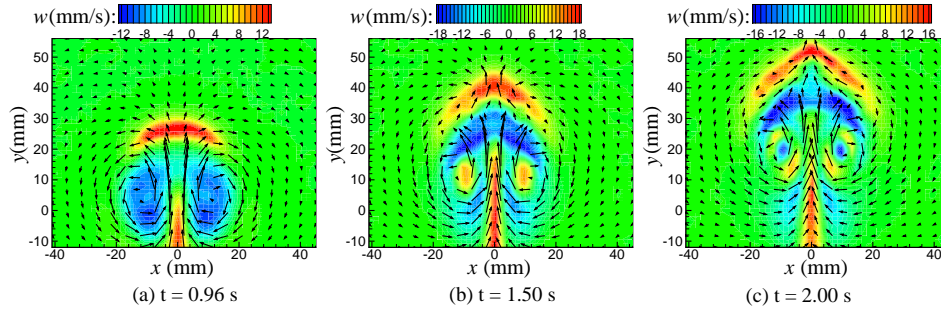


Figure 3.9 – Numerically obtained snapshots of the velocity fields (5 mm measurement height) with stress-free conditions at both the bottom and the free surface (see Table I for the numerical parameters) at (a) $t = 0.96$ s, (b) $t = 1.50$ s, and (c) $t = 2.00$ s. Meaning of vectors and shades/colours: see caption of Fig. 3.4.

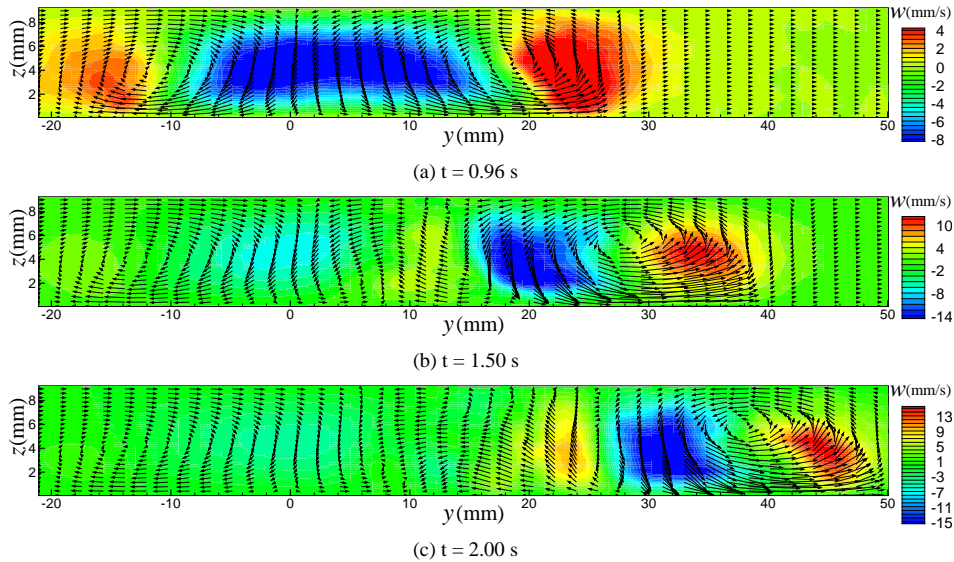


Figure 3.10 – Numerically obtained snapshots of the velocity in the vertical slice at $x = -12.5$ mm with stress-free conditions at both the bottom and the free-surface (see Table I for the numerical parameters) for (a) $t = 0.96$ s, (b) $t = 1.50$ s, and (c) $t = 2.00$ s. Meaning of vectors and shades/colours: see caption of Fig. 3.8.

dent on the no-slip condition. However, the spanwise vortex with strong positive ω_x , see Fig. 3.7(b), is still present. Furthermore, a higher propagation velocity of the dipole is observed as a consequence of the absence of damping due to bottom friction. Obviously the no-slip bottom boundary layer is *not* the only actor in the generation of three-dimensionality in the

flow.

Also the vertical component of the (three-dimensional) Lorentz force plays a negligible role in generating three-dimensionality and associated vertical motion, which was confirmed by numerical simulations with the vertical component of the Lorentz force (artificially) set to zero. It is rather the non-uniformity in the vertical direction of the *horizontal* components of the Lorentz force that results in the observed 3D motion, as this introduces a z -dependence of the vertical vorticity ω_z , or, equivalently, in the swirl velocity v_θ . Of course, during the forcing period, this non-uniformity is the main driving mechanism of vertical motion, and explains why the numerical simulations with no-slip and stress-free bottom condition show such close resemblance [cf. Figs. 3.8(b) and 3.10(a)]. However, one should not conclude from this that the observed 3D structures in the post-forcing phase are solely due to three-dimensionality introduced by the electromagnetic forcing. Numerical simulations with the flow initialized in an alternative

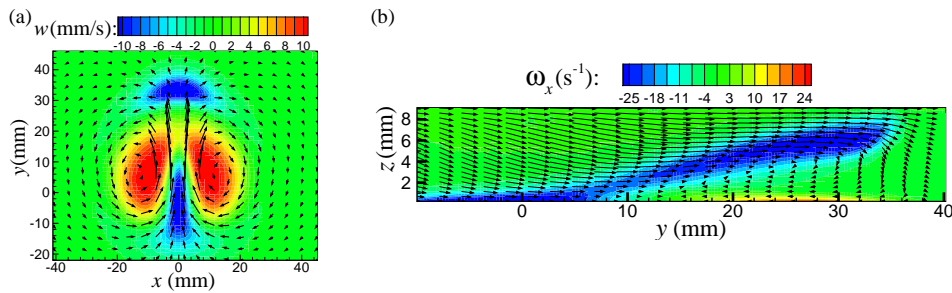


Figure 3.11 – (a) Numerically obtained snapshot of the velocity (5 mm measurement height for $t = 1.0$ s) where colours indicate the magnitude of the vertical velocity w resulting from a Lamb-like initialisation. (b) Vertical slice ($x = 0$ for $t = 1.0$ s) of the numerically obtained ω_x vorticity component resulting from a Lamb-like initialisation.

way, e.g., by imposing a Lamb-like planar dipole structure with a purely horizontal flow field that is divergence-free and that satisfies a no-slip bottom boundary with a Poiseuille-like structure in the vertical, show that such an initial dipolar flow evolves similar as observed in the laboratory experiments, i.e., with qualitatively the same 3D flow structures as shown in Figs. 3.1 and 3.4. Figure 3.11 displays numerically obtained snapshots from such an artificial initialisation. In the horizontal slice presented in Fig. 3.11(a) strong upwelling is seen inside the vortex cores caused by the

vertical dependence dictated by the initial Poiseuille-like profile of the velocity field. In Fig. 3.11(b) the frontal circulation is seen in front of the dipole indicated by the negative ω_x whose magnitude exceeds the magnitude of the primary vorticity ω_z by a factor 2.5.

From the above it is concluded that not the no-slip boundary condition is the main cause of three-dimensionality, but it is rather the vertical confinement of the shallow layer in combination with the vertical gradient in the horizontal forcing that leads to the complicated 3D structures.

3.3.4 Quantifying two-dimensionality of the shallow flow

Three-dimensional effects in shallow fluid flows may be quantified in different ways. One possibility is to use the kinetic energy ratio $q = E_V/E_H$, where the instantaneous kinetic energies E_H and E_V associated with the horizontal and vertical flow components, respectively, are computed as

$$E_H = \frac{1}{2} \mathcal{H} \iint_S \rho(u^2 + v^2) dx dy, \quad (3.6a)$$

$$E_V = \frac{1}{2} \mathcal{H} \iint_S \rho w^2 dx dy. \quad (3.6b)$$

Note that E_H and E_V defined in this way represent the kinetic energy evaluated in a horizontal plane S at $z = h$. The fluid depth H will be used as a measure of the vertical length scale \mathcal{H} .

Figures 3.12(a)-(c) present the numerically obtained “horizontal” kinetic energy E_H (solid line) and “vertical” kinetic energy E_V (dashed line) for a fluid depth of 9.3 mm, evaluated at three different levels $z = h$ above the (no-slip) bottom, i.e., at $h = 2.00, 5.00,$ and 9.00 mm. The second column of figures [Figs. 3.12(d)-(f)] shows the energies E_H and E_V as measured in an experiment carried out under the same conditions, i.e., with a no-slip bottom. Since the total fluid depth $H = 9.3$ mm, Figs. 3.12(a) and 3.12(d) show the evolution as evaluated just above the bottom, Figs. 3.12(b) and 3.12(e) at approximately mid-depth of the fluid layer, and Figs. 3.12(c) and 3.12(f) just below the free-surface.

In Figs. 3.12(a)-(c) one observes an increase of E_H during the forcing phase for all three evaluation levels. A global maximum is attained at $t = 1$ s [for Fig. 3.12(c) a little bit later] when the forcing stops, after which decay sets in. For the vertical component of the kinetic energy E_V (note the different scaling of the left and right axes in the figures), it is seen that

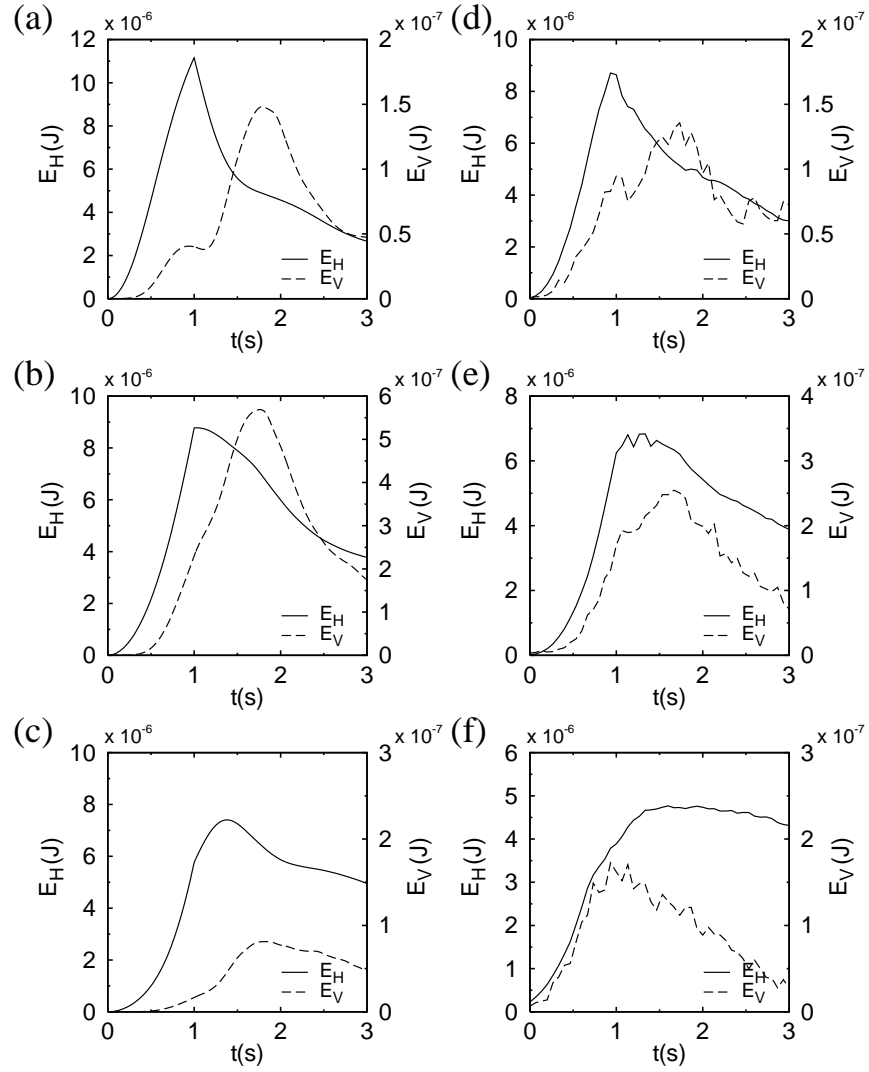


Figure 3.12 – Evolution of the horizontal kinetic energy E_H (left axis) and vertical kinetic energy E_V (right axis) at different levels $z = h$ inside the fluid. Numerical results evaluated at (a) $h = 2.00$ mm, (b) $h = 5.00$ mm, and (c) $h = 9.00$ mm above the bottom. Experimental results measured at (d) $h_{ls} = 2.00$ mm, (e) $h_{ls} = 5.00$ mm, and (f) $h_{ls} = 9.00$ mm, for fluid depth $H = 9.3$ mm and current strength $I = 4.4$ A.

the maximum is reached some time after the forcing has stopped, roughly at $t = 1.7$ s. As is to be expected, E_V is largest at mid-depth and smaller near the bottom and the free-surface. For early times, it is seen that E_V remains small, consistent with the fact that initially the vertical component of the Lorentz force does not drive the flow, as discussed in the previous subsection.

Comparison of the numerical simulation results [Figs. 3.12(a)-(c)] with the corresponding experimentally obtained results [Figs. 3.12(d)-(f)], reveals a good qualitative agreement. Quantitatively, differences are seen which we attribute to the matching of the numerical simulations to the experiments, as discussed in Sect. 2.3. Besides these differences, the initial time behaviour of E_V and the time at which E_V attains its maximum is nicely captured [except for Fig. 3.12(f) where the measurement was performed close to the free surface].

Figure 3.13 shows the evolution of the kinetic energy ratio $q = E_V/E_H$ for three cases to illustrate the influence of (i) the evaluation level [see Fig. 3.13(a)], (ii) the forcing strength [Fig. 3.13(b)], and (iii) the fluid depth [Fig. 3.13(c)].

(i) Figure 3.13(a) reveals that the energy ratio q is highly dependent on

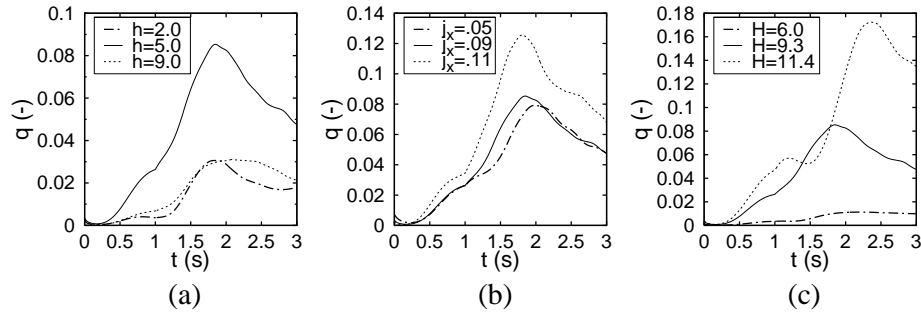


Figure 3.13 – Numerically obtained evolution of the kinetic energy ratio q . (a) Varying evaluation level h , whereas fluid depth ($H = 9.3$ mm) and forcing strength ($j_x = 0.09$ A/cm²) are kept constant. (b) Varying forcing strength j_x , whereas fluid depth ($H = 9.3$ mm) and evaluation level ($h = 5.0$ mm) are kept constant. (c) Varying fluid depth H , whereas forcing strength ($j_x \approx 0.09$ A/cm²) is kept constant and evaluated at mid-depth of the fluid (i.e., $h/H \approx 0.5$).

the evaluation level. Near the free-surface and no-slip bottom the q -value is minimal due to the impermeability condition, leading to small values of w , whereas the kinetic energy ratio attains a maximum at mid-depth,

where w approximately attains its maximum magnitude. Clearly, based on the kinetic energy ratio q , the free-surface is not representative of the two-dimensionality inside the bulk of the fluid. The ratio q attains a maximum after the forcing has been switched off (approximately at $t = 1.7$ s) as E_V attains its maximum there [see, e.g., Fig. 3.12(e)].

(ii) Figure 3.13(b) demonstrates the effect of changes in strength of the forcing: an increase of the forcing strength corresponds with an increase of the kinetic energy ratio q .

(iii) Figure 3.13(c) shows the numerically obtained evolution of the q -ratio for varying fluid depth H . Apparently, the flow behaves more 2D-like with decreasing fluid depth. However, it should be noted that experimentally there exists a practical lower bound for the fluid depth, as the damping of the flow (due to the bottom friction) becomes stronger for decreasing fluid depth.

Figure 3.14 displays the numerically obtained ratio Q of the vertical and horizontal kinetic energies contained in the entire 3D fluid volume, for decreasing values of the fluid depth H . Since one expects a scaling of the

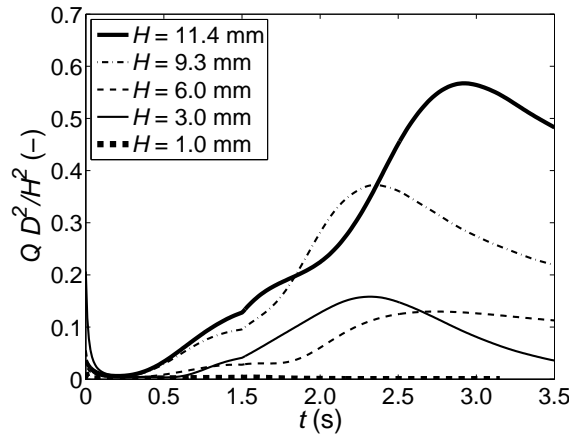


Figure 3.14 – Numerically simulated evolution of the kinetic energy ratio $Q \cdot D^2/H^2$ for 5 different fluid depths H . Note that the vertical and horizontal kinetic energy components are computed through an integration over the entire 3D domain.

kinetic energy ratio Q with H^2/D^2 , the scaled version $Q \cdot D^2/H^2$ is depicted in Fig. 3.14. Qualitatively, similar behaviour is seen as the q -ratio displayed in Fig. 3.13(c). Clearly, for the $H = 1$ mm fluid depth $Q \approx 0$, the flow is

very close to two-dimensionality. However, a strong increase of the Q -value is seen when increasing the fluid depth. This increase is stronger than expected from the scaling, which might be due to the inertial oscillations.

An alternative quantity that can be used to characterize the deviation from two-dimensionality in the flow is the normalized horizontal divergence Λ , which is computed in a horizontal plane as

$$\Lambda = \frac{\mathcal{H} \iint_S |\nabla_H \cdot \mathbf{u}| \, dx \, dy}{\mathcal{L} \iint_S |\omega_z| \, dx \, dy}, \quad (3.7)$$

where ∇_H denotes the divergence with respect to only the horizontal components. In the expression for Λ , ω_z is the vertical component of the vorticity, and the magnet diameter is taken as a measure of the horizontal length scale \mathcal{L} . The normalization factor is a measure of the characteristic horizontal velocity.

Figure 3.15 displays the numerically calculated evolution of Λ at three different levels, i.e., at $h = 2.0$, 5.0, and 9.0 mm for the same fluid depth ($H = 9.3$ mm) and current strength ($I = 4.4$ A) as in Fig. 3.12. Obviously,

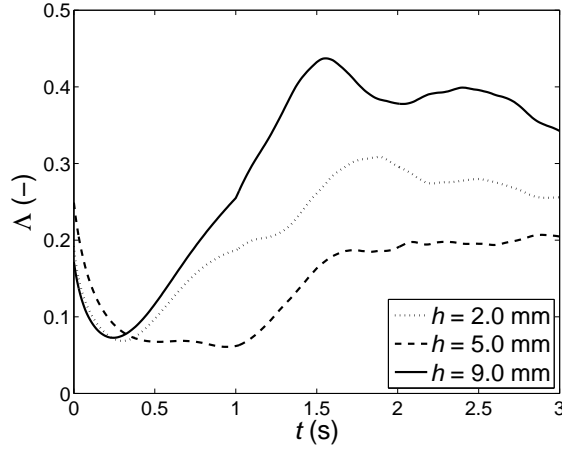


Figure 3.15 – Numerically calculated evolution of the normalized horizontal divergence Λ at three different evaluation levels (2.0, 5.0, and 9.0 A). For all cases $H = 9.3$ mm and $I = 4.4$ A [same settings as Figs. 3.12(a)-(c)].

the normalized horizontal divergence Λ is non-zero at all three measurement planes, whereas in pure 2D flow it should be zero. The highest Λ -values (maximum over 40%) are observed at the level closest to the surface ($h = 9.0$ mm).

It is remarkable that the behaviour of the normalized horizontal divergence Λ suggests deviations from Q2D behaviour in a different way than revealed by the kinetic energy ratio q : while q approaches zero at the free-surface (where w becomes zero) and attains a maximum at mid-depth of the fluid layer, Λ reaches a minimum at mid-depth and maximum at the free-surface.

To investigate the tendency of relaxation to a Poiseuille-like profile of the (3D) velocity field with decreasing fluid depth H , a quantity is derived which is a measure of the difference between the actual 3D velocity field and a velocity field with a Poiseuille-like structure in the vertical direction. The numerically obtained 3D velocity field \mathbf{v} can be compared with a Poiseuille-like profile in the following way. First considering the 3D velocity field, i.e.,

$$\mathbf{v} = \mathbf{v}(x, y, z, t) = u\mathbf{e}_x + v\mathbf{e}_y + w\mathbf{e}_z, \quad (3.8)$$

one can then define the Poiseuille-like profile \mathbf{v}_p in the following way

$$\mathbf{v}_p = \mathbf{v}(x, y, z = H, t) \sin\left(\frac{\pi z}{2H}\right). \quad (3.9)$$

The Poiseuille-like flow \mathbf{v}_p is thus the 3D velocity field, taken at the surface with a sine-like dependence in the vertical direction. Eqs. (3.8) and (3.9) satisfy $\mathbf{v}(x, y, z = H, t) = \mathbf{v}_p(x, y, z = H, t)$ and $\mathbf{v}(x, y, z = 0, t) = \mathbf{v}_p(x, y, z = 0, t) = 0$.

Now consider the rms value as a measure of the difference between the 3D velocity field and the Poiseuille-like profile, i.e.,

$$F(t, H) = \sqrt{\langle (u - u_p)^2 + (v - v_p)^2 \rangle}, \quad (3.10)$$

which is a function of time t and the fluid depth H under consideration. A spatial averaging is implied by the angular brackets. Substitution of the planar components of Eqs. (3.8) and (3.9) in (3.10) leads to

$$F^2 = \frac{1}{V} \iiint_V \left\{ \left[u(x, y, z, t) - u(x, y, z = H, t) \cdot \sin\left(\frac{\pi z}{2H}\right) \right]^2 + \left[v(x, y, z, t) - v(x, y, z = H, t) \cdot \sin\left(\frac{\pi z}{2H}\right) \right]^2 \right\} dx dy dz, \quad (3.11)$$

where V is the volume of the computational domain. The latter equation is normalized with the rms value of the horizontal components of the 3D

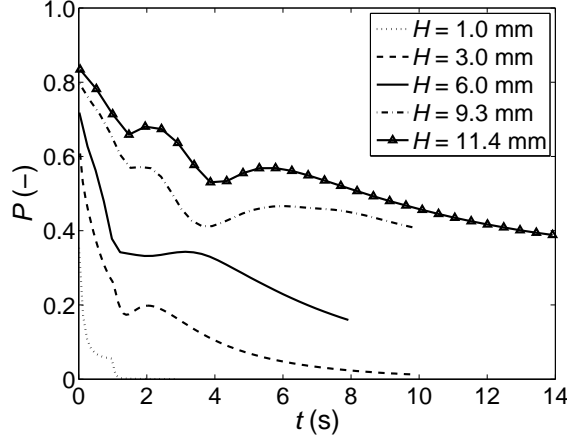


Figure 3.16 – Numerically obtained temporal evolution of the quantity P [see Eq. (3.13)], which expresses the deviation from a Poiseuille-like profile, for different values of the fluid depth H . The current density j_x is kept constant at 0.09 A/cm^2 .

velocity field

$$F_{norm}^2 = \frac{1}{V} \iiint_V \left[u^2(x, y, z, t) + v^2(x, y, z, t) \right] dx dy dz. \quad (3.12)$$

A measure P of the relative difference between the 3D velocity field and the Poiseuille-like flow is defined according to

$$P = \frac{F}{F_{norm}}. \quad (3.13)$$

If $P \approx 0$, the flow is very close to a flow with a Poiseuille-like vertical structure. Figure 3.16 shows the numerically obtained temporal evolution of P for several fluid depths. The non-zero P value at $t = 0$ is artificial due to division of two numerically very small numbers (there is no fluid motion at $t = 0$). The graph displays a sharp decrease of P during the forcing phase, i.e., $0 < t \leq 1$ s. As soon as the forcing stops, a relaxation process sets in (except for $H=1$ mm, which is due to the strong bottom friction). The oscillatory behaviour visible in Fig. 3.16 during this relaxation phase is related to the previously mentioned inertial oscillations. For large times an exponential decay of P is observed whose time scale is comparable to the bottom friction time scale τ_E , whereas one would like to see the relaxation towards Poiseuille-like profile to be much faster than the bottom friction

time scale. This illustrates, as seen before, that bottom friction is merely one of the mechanisms generating 3D motions, not the main actor. The deviation from the Poiseuille-like vertical structure decreases with decreasing fluid depth, although one has to bear in mind that the damping due to bottom friction becomes stronger with decreasing fluid depth (and may therefore become experimentally unpractical).

3.4 Conclusions and Discussion

Many experiments on 2D or quasi-2D turbulence have been performed in shallow layers of fluid, under the assumption that the shallowness assures sufficient suppression of vertical motions. Moreover, vertical dependence due to the no-slip bottom is commonly modelled through the introduction of Rayleigh damping, which is presumed to be justified by a Poiseuille-like flow profile in the vertical.

In this chapter, the validity of these assumptions have been examined by studying experimentally as well as numerically the 3D structure of a generic vortex structure in Q2D turbulence, i.e., a dipolar flow in a single shallow layer of electrolyte. Our results show that significant and remarkably complex 3D structures and vertical motions occur throughout the flow evolution, i.e., during and after the forcing.

The development of vertical motion in the dipole is directly linked with the horizontal flow field varying with depth. The cyclostrophic balance then dictates a pressure that also varies with height, which subsequently drives a vertical motion. Moreover, since free-surface deformation is absent in the numerical model, the close resemblance of the simulations and laboratory experiments implies that surface gravity waves are of minor importance in generating this vertical motion in the laboratory experiments.

Due to the type of boundary conditions, vertical confinement or z -dependent forcing, vertical variations in the horizontal flow field are inevitable in every experimental realization of one- and two-layer shallow flows. The *only* situation in which these 3D flow features with vertical velocities will not develop is a flow with: (i) stress-free bottom and surface boundary conditions, and (ii) a forcing mechanism that has no vertical component, with its horizontal components uniform over the fluid depth and which generates a horizontal divergence-free velocity field. This is a situation that is certainly hard to achieve in practice with the current ex-

perimental set-up (although these conditions might be more closely met in soap-film experiments).

Moreover, based on the criteria introduced in Sect 3.3.4 it is shown that the vertical structure of such shallow flows relaxes towards a Poiseuille-like profile on a timescale that is comparable to the bottom friction time scale. The latter result questions the use of a linear (Rayleigh) friction model to model a no-slip bottom. Since the vortex dipole can be considered as a prototype flow structure in 2D turbulence, the conclusions of the present study may apply more generally to experimental realizations of 2D turbulence, both for the decaying and the forced case.

CHAPTER 4

The dipole in two-layer fluids

The experiments on a freely evolving dipolar vortex in a homogeneous shallow fluid layer, as described in the previous chapter, have clearly shown its complex 3D structures and subsequent evolution. The present chapterⁱ focuses on the 3D structures of a dipolar vortex in a stable two-layer fluid setup, which was believed to be a significant improvement over the single-layer setup in the sense of shielding the upper layer from the bottom, and hence suppressing any vertical motion. Remarkably, the experimental results, supported by numerical simulations, show to a large extent the same 3D structures and evolution as in the single-layer case. The so-called “frontal circulation” is also observed in the two-layer experiments and is shown to be related to deformations of the internal interface.

The rest of this chapter is organized as follows: Sect. 4.2 outlines the experimental and numerical details. The experimental and numerical results of the dipole evolution during the forcing and the subsequent free-evolution phase are then presented in Sec. 4.3. Furthermore, the influence of the deformable internal interface on the 3D flow, the effects of decreasing upper fluid-layer thickness, the degree of two-dimensionality of the flow, and tracer transport at the free surface are discussed. Finally, in Sec. 4.4 the conclusions are summarized.

ⁱThis chapter is to a large extent based on two papers [3, 4], i.e. R.A.D. Akkermans, L.P.J. Kamp, H.J.H. Clercx and G.J.F. van Heijst, “Three-dimensional flow in electromagnetically driven two-layer fluids,” *Phys. Rev. E* (submitted, 2009) and R.A.D. Akkermans, L.P.J. Kamp, H.J.H. Clercx and G.J.F. van Heijst, “Intrinsic three-dimensionality in electromagnetically driven shallow flows,” *Europhys. Lett.* (2008).

4.1 Introduction

Large-scale geophysical flows such as the Earth’s atmosphere and oceans can be considered as quasi-two-dimensional due to the combined action of background rotation, density stratification, and the limited vertical dimension as compared to the horizontal ones [50]. On smaller scales, the effects of background rotation and stratification do not play an important role. However, the limited vertical dimension \mathcal{H} as compared to the horizontal length scale \mathcal{L} suppresses vertical motions, and the flow is predominantly planar. Examples where the shallowness alone promotes quasi-two-dimensional flow behavior are rivers, channels, and estuaries (see, e.g., [39,89]). Furthermore, two-dimensional (2D) turbulence can be seen as an extremely shallow flow configuration. Therefore, many experiments have been performed in shallow fluid layers to investigate the dynamics of vortices and 2D turbulence, see Refs. [2,3,12,26,27,84,88] and [19] for a review.

Despite the shallowness of the flow, deviations from two-dimensionality occur. This is due to the way the flow is generated but also due to friction at the solid bottom, which induces vertical gradients of the velocity field [2]. In shallow fluid layer experiments the interaction of the flow with the no-slip bottom boundary is usually modelled by adding a linear friction term (Rayleigh friction) to the 2D Navier-Stokes equations under the assumption that the vertical variation of a predominantly horizontal flow field is Poiseuille-like [20,38,67]. However, several studies have recently shown that this vertical Poiseuille-like profile is questionable [2,3,51].

In the last years the 3D flow structure of elementary vortices in a shallow fluid layer has received considerable attention [2,3,51,54,77,85,86]. For the monopolar vortex without background rotation, numerical studies by Satijn *et al.* [77] revealed the presence of a secondary circulation as a result of the Bödewadt flow (see, e.g., [6,36]).

Similar secondary flows are also expected within the vortices constituting the dipole. However, several other 3D flow structures have been found for propagating dipoles in shallow fluids. Lin *et al.* [54] showed the emergence of a vortex orthogonal to, and just in front of the propagating dipole. This roll-like vortical structure is referred to as the “frontal circulation” [85,86]. In both the experiments by Lin *et al.* [54] and those by Sous *et al.* [85,86] the dipole was created by injecting horizontally a small amount of fluid in the fluid layer. Furthermore, Sous *et al.* report that the frontal circulation was not present in experiments carried out in a two-layer

fluid (based on qualitative observations).

Recently, Akkermans *et al.* [2, 3] confirmed the presence of this frontal circulation in experiments (and numerical simulations) of electromagnetically forced vortex dipoles in a shallow fluid layer. The importance of this roll-like structure was quantified by the magnitude of the horizontal vorticity component of the frontal circulation cell. This horizontal vorticity exceeded the magnitude of the primary vorticity by at least a factor two during its evolution. In addition to the frontal circulation, strong upwelling in the wake of the dipole and axial motion inside the two individual vortex cores of the dipole are present, the latter even oscillating in time [2].

The above mentioned studies concerned flow structures far away from lateral walls. Cieslik *et al.* [16] studied the influence of a lateral wall on the three-dimensionality of the flow for the canonical case of a dipole-wall collision. Remarkably, the influence of the wall on the vertical motion inside the dipolar vortex becomes stronger for decreasing fluid depths, which was attributed to the role of the frontal circulation [16].

The shortcomings of the single layer setup have been recognized and nowadays the two-layer fluid setup, consisting of a light fluid layer on top of a heavier bottom layer, has become quite standard [10, 67, 68, 73, 80]. These experiments focus on the motion in the top layer, which is less influenced by bottom friction. Whether this two-layer setup is a significant improvement over the single-layer setup remains an open question.

4.2 Details of experiments and simulations

The experimental setup was already outlined in Sect. 2.2.2. In order to study the influence of different fluid-layer depths on the flow behaviour, the top-layer thickness H_{ul} has been decreased in steps down to almost 3 mm, i.e., 9.0, 7.0, 5.0, and 3.5 mm. The latter fluid-layer thickness mimics the traditional fluid-layer configuration for 2D turbulence experiments (see, e.g., [67, 68, 73, 81]). Table I provides an overview of the performed experiments. Note that the Reynolds number Re is based on the maximum horizontal velocity \mathcal{U} at the end of the forcing, while the magnet diameter is taken as a measure of \mathcal{L} . The densimetric Froude number Fr' is defined as $\mathcal{U}/\sqrt{g'H_{ul}}$. The reduced gravity g' is computed as $g\Delta\rho/\rho_1$, with $\Delta\rho = \rho_2 - \rho_1$ (subscript 1 and 2 refer to the top and bottom layer, respectively) and g denotes the gravitational acceleration.

Table I – Experimental parameter values for the SPIV measurements in the two-layer flow: upper fluid-layer depth H_{ul} , measurement level h_{ls} , current density j_x , Reynolds number Re , and densimetric Froude number Fr' . Note that the bottom layer thickness H_{bl} is kept constant at 3 mm for all experiments.

H_{ul} (mm)	h_{ls} (mm)	j_x (A/cm ²)	Re (-)	Fr' (-)
9.0	7.5	0.13	1200	0.23
7.0	6.5	0.12	1250	0.28
5.0	5.5	0.13	1700	0.43
3.5	4.5	0.14	2000	0.64

All measurements have been performed in a horizontal cross-sectional plane at mid-depth of the top fluid layer. In Sect. 4.3 results are presented mainly for the experiments with $H_{ul} = 7.0$ mm, as the flow evolution observed in these experiments is indicative for the experiments with different fluid-layer depths.

In all the two-layer simulations the upper free-surface was set to be stress-free and flat, while the bottom was taken to be no-slip, as in the experimental situation. In the previous chapter, free-surface deformations were shown to be of minor importance in generating vertical motions for the single-layer dipole.

At the (nondeformable) internal interface the following conditions are imposed: continuity of the 3D velocity vector and (shear and normal) stresses, and zero vertical velocity. The latter condition means that the generation of interfacial waves is excluded. This is the only difference between the simulations and experiments; the possible effect of this rigid internal interface will be discussed in the results section.

4.3 Experimental and numerical results

In this section the experimental and numerical results are presented. First, the experimental results for the case $H_{ul} = 7.0$ mm are discussed, together with the corresponding numerical results (although obtained for the case of a rigid internal interface). Next, the effect of a decreasing upper fluid layer depth is considered. Finally, the structure of tracer transport at the free surface is illustrated.

4.3.1 The 3D flow evolution of a dipole in a two-layer fluid

Figure 4.1 shows plots of the instantaneous vertical (shades/colours) and horizontal (vectors) velocities in a horizontal plane at mid-depth of the upper layer. For clarity of presentation the vectors are under-sampled: only every fourth vector is shown in the x - and in the y -direction, so that approximately only 6% of the total set is shown. Since the total forcing time $\Delta t = 1$ s and the forcing is started at $t = 0$, Figs. 4.1(a,c) correspond to the end-stage of the forcing, while Figs. 4.1(b,d) show the flow field after the forcing has stopped.

During the entire forcing phase, a buildup of downward motion is seen inside the two vortex cores, as is illustrated in Fig. 4.1(a), as well as strong upwelling in the tail of the dipole. After the forcing has stopped, see Fig. 4.1(b), the dipole starts to propagate and soon upward motion is seen inside the vortex cores, surrounded by an area with downward motion. Comparison of the numerical simulation results shown in Figs. 4.1(c,d) with the corresponding experimental observations [Figs. 4.1(a,b)] reveals a close resemblance with respect to the flow structures and their evolution.

At a later stage of the flow evolution, the vertical motion inside the vortices is seen to change in a downward one [delineated by the dashed circles in Fig. 4.2(b)]. Furthermore, bands of upward and downward motion are observed at the front side of the moving dipole, representing the frontal circulation roll. Surprisingly, the 3D structures and evolution as depicted in Figs. 4.1(a,b) and Figs. 4.2(a,b) show a remarkable resemblance with the ones already seen in the single-layer dipole (see Chapter 3).

In Chapter 3 the development of vertical motion was related to vertical gradients in the horizontal flow field. Apparently, the horizontal flow field in the top layer has a z -dependence that is similar to the one present in the single-layer case, which explains the close similarity of the 3D structures and evolution in the two-layer fluid. This z -dependence is introduced by the magnetic field whose strength varies with height and also by the shear stress exerted by the bottom layer.

Comparison of the numerical simulation results shown in Figs. 4.2(c,d) with the corresponding experimental observations [Figs. 4.2(a,b)] reveals a striking resemblance with respect to the flow structures and their evolution. However, there is a slight phase shift present, e.g., the second sign change of the vertical velocity inside the individual vortex cores in the experiment [see Fig. 4.2(b)] is not yet seen in the numerical snapshot shown in Fig. 4.2(d); this occurs after approximately $t = 2.5$ s in the simulation. Furthermore,

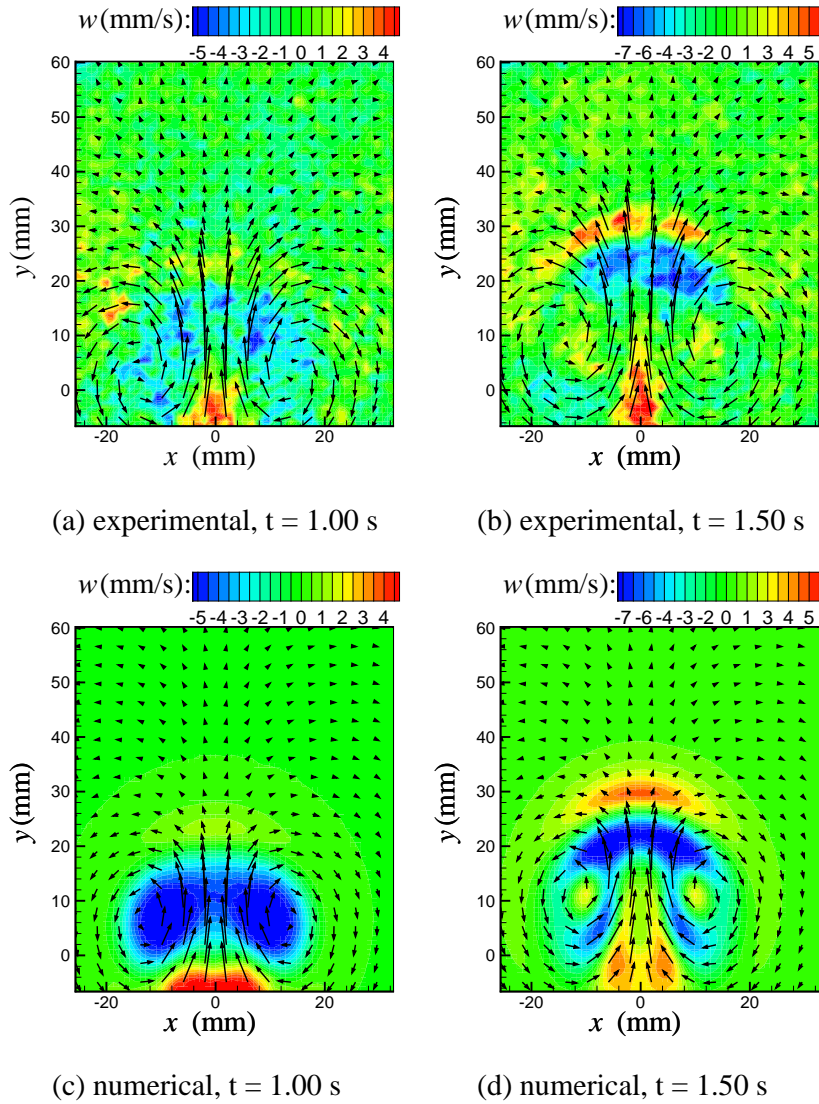


Figure 4.1 – Instantaneous velocity fields of a dipolar vortex in a two-layer system observed in a horizontal plane at mid-depth of the top fluid layer ($H_{ul} = 7.0$ mm). Vectors represent horizontal velocity components and colour/gray levels indicate the magnitude of the vertical velocity. Experimental results obtained with SPIV at (a) $t = 1.00$ s and (b) $t = 1.50$ s. Numerical snapshots obtained with a rigid internal interface at (c) $t = 1.00$ s and (d) $t = 1.50$ s.

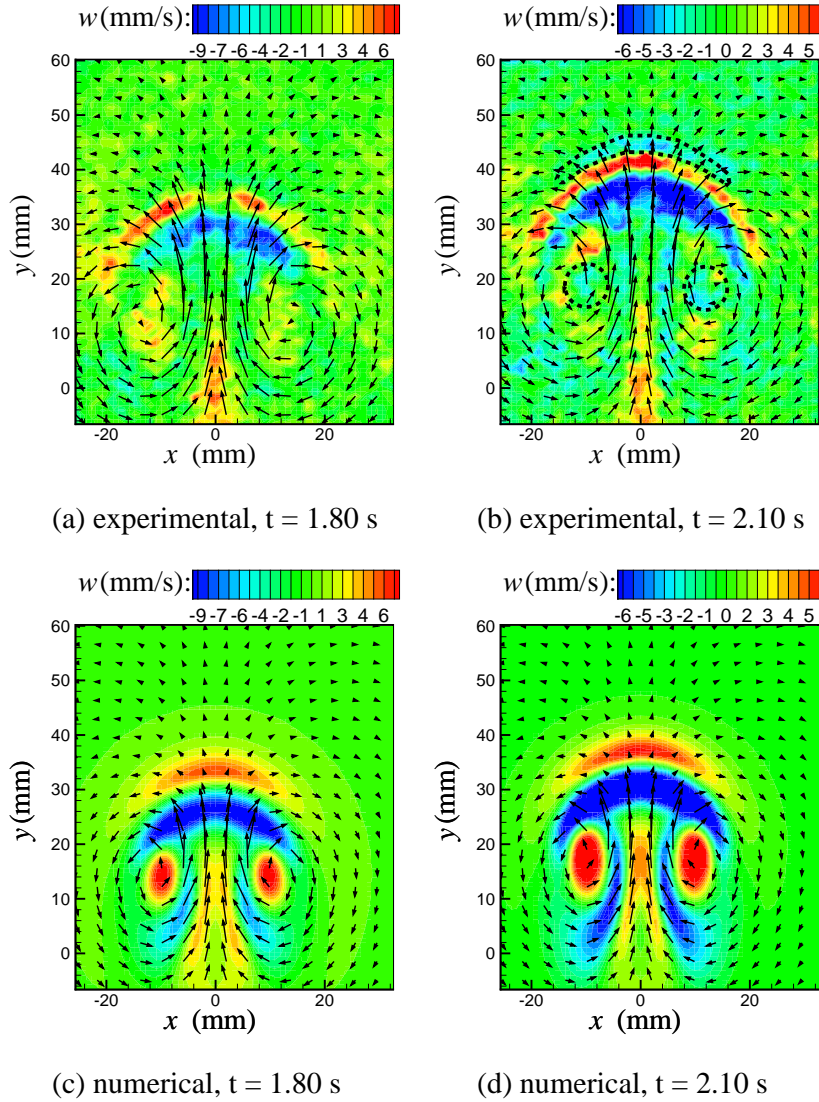


Figure 4.2 – Same as Fig. 4.1, except left column represents flow field at $t = 1.80$ s and right column at $t = 2.10$ s. The dashed circles in (b) indicate the region of downwelling inside the vortex cores and the elongated dashed contour points toward the region of downwelling associated with the frontal circulation.

the frontal circulation is not seen in the top layer of the numerical simulation [compare Fig. 4.2(d) with Fig. 4.2(b)], the region of rather weak

downward motion associated with the frontal circulation [as delineated by the dashed contour in Fig. 4.2(b)] is not present in the numerical simulation. This absence is attributed to the rigid internal interface used in this simulation, as will be explained next.

4.3.2 Development of the frontal circulation

This absence of the frontal circulation is illustrated in more detail in the vertical slice presented in Fig. 4.3(a). The negative vorticity ω_x in the lower fluid layer is associated with the viscous boundary layer at the no-slip bottom. At later stages in the evolution this negative vorticity patch detaches

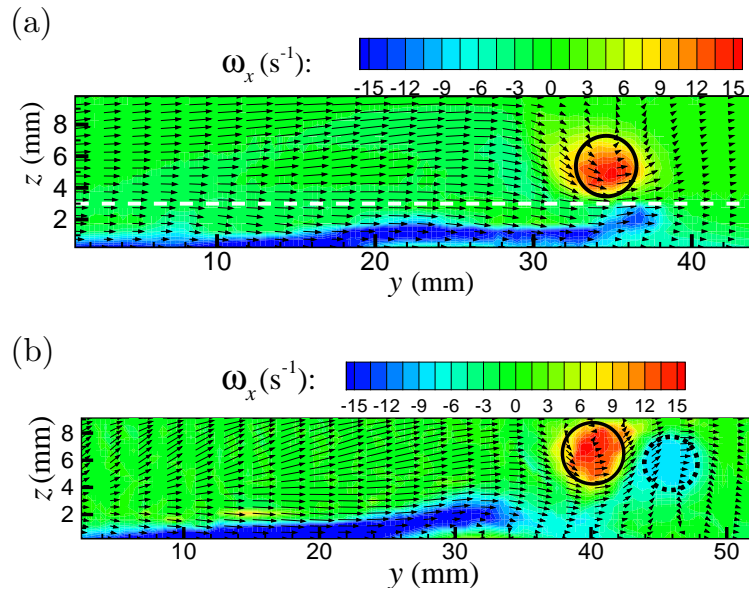


Figure 4.3 – (Colour online) Numerically obtained snapshots of vertical slices through the symmetry plane of the dipole ($x = 0$) at time $t = 2.60$ s showing the ω_x vorticity distribution, with vectors representing the flow in the yz -plane. Snapshot of (a) two-layer setup, illustrating the absence of the frontal circulation in the top layer (the white dashed line indicates the internal interface between the fluid layers) and (b) single-layer setup with frontal circulation present. The solid and dashed circles indicate the positive and negative ω_x vorticity patches, respectively.

from the bottom and forms the frontal circulation, in a way similar to what happens in the single layer situation [see Fig. 4.3(b)]. However, in

the two-layer case this negative vorticity ω_x does not penetrate through the internal interface [indicated with the dashed white line in Fig. 4.3(a)], and is therefore absent in the top layer. The positive vorticity ω_x is associated with the downwelling initiated during the forcing phase (the magnetic field decays with height, which results in a pressure gradient that drives a downward motion). This downward and subsequently horizontal motion is deflected upward at the instantaneous separatrix, the latter is delineated by the band of upward motion in front of the dipole [see, e.g., Fig. 4.1(d)]. This results in the positive ω_x vorticity patch seen in both the single- and two-layer simulations as indicated by the solid circles in Fig. 4.3. However, in the two-layer simulation only the upper fluid layer is forced, therefore the positive vorticity patch is only present in the upper layer. Note that the magnitude of the (positive) vorticity component ω_x in the vertical slice of Fig. 4.3(a) turns out to evolve to significantly larger values than that of the “primary” vorticity component ω_z , similar to what was seen for the single-layer dipole.

In the numerical simulation the interface is taken flat, whereas in the experiment the interface will most likely deform, as the density of the two fluids is comparable ($\Delta\rho/\rho_1 \approx 0.5$). In the present two-layer experiments the formation of the frontal circulation has presumably a different origin than in the one-layer experiments (as discussed Chapter 3), as it is to be directly linked with the interface deformation. Interface deformation implies baroclinic vorticity production, which is described by a source term of the form $\frac{1}{\rho^2} \nabla\rho \times \nabla p$ in the vorticity equation. The sharp internal interface implies locally a strong density gradient. As soon as the interface deforms, the pressure gradient and density gradient are no longer aligned ($\nabla\rho \times \nabla p \neq 0$), which leads to vorticity production. This is schematically depicted in Fig. 4.4, showing the interface deformation at the front side of the dipole (in the symmetry plane of the dipole, i.e., $x = 0$). Based on the simulation, the interface will be displaced upwards at the front and downward closer to the dipole [cf. Fig. 4.1(h)], resulting in the interfacial shape as depicted in Fig. 4.4. Locally, the density gradient $\nabla\rho$ is directed downwards, perpendicular to the interface. Together with a vertical pressure gradient as shown in the schematic, this leads to a production of negative vorticity ω_x in the top layer. This negative vorticity patch is then advected upward in a way similar to what is seen in the single-layer case [cf. Fig. 4.3(b)].

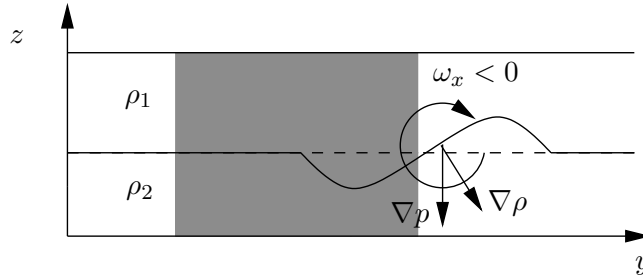


Figure 4.4 – Schematic illustration of the baroclinic vorticity production resulting from interfacial deformation in a stably stratified two-layer system. The position of the dipole is schematically illustrated in gray.

4.3.3 The 3D structure of the dipole with decreasing upper fluid layer depth

Figure 4.5 shows snapshots of the dipolar flow structure for different upper fluid-layer depths: the panels show the structure of the horizontal and vertical fluid motion in a horizontal cross-section at mid-depth of the top layer for the case of an upper layer thickness (a) $H_{ul} = 9.0$ mm, (b) $H_{ul} = 7.0$ mm, (c) $H_{ul} = 5.0$ mm, and (d) $H_{ul} = 3.5$ mm. For all cases one observes a similar pattern of vertical motion, as was also seen for the case $H_{ul} = 7.0$ mm [see Fig. 4.5(b)] that was discussed in Sect. 4.3.1: strong upward motion in the tail of the dipole, together with the frontal circulation. In contrast to the qualitative observation by Sous *et al.* [85,86], the frontal circulation is observed in the here reported two-fluid layer experiments. Also, in all four snapshots the second sign change of the vertical velocity inside the individual vortices can be seen. These features are also present for the case $H_{ul} = 5.0$ mm, although less pronounced. Clearly, the observed 3D structures in the $H_{ul} = 7.0$ mm case are indeed representative for the other upper fluid depths. The same applies for the evolution in time. The magnitude of the vertical velocity component remains approximately constant with decreasing H_{ul} , whereas the horizontal velocity magnitude increases with decreasing upper fluid layer thickness. This increase is expected as the measurement height becomes more close to the magnet for decreasing H_{ul} , where the Lorentz force effectively drives a stronger horizontal velocity field. In the next section, numerical simulations are discussed where this effect is studied.

The shallowness of the fluid layers in our experimental setup is often used as a justification for quasi-2D flow behaviour. Although the snapshots

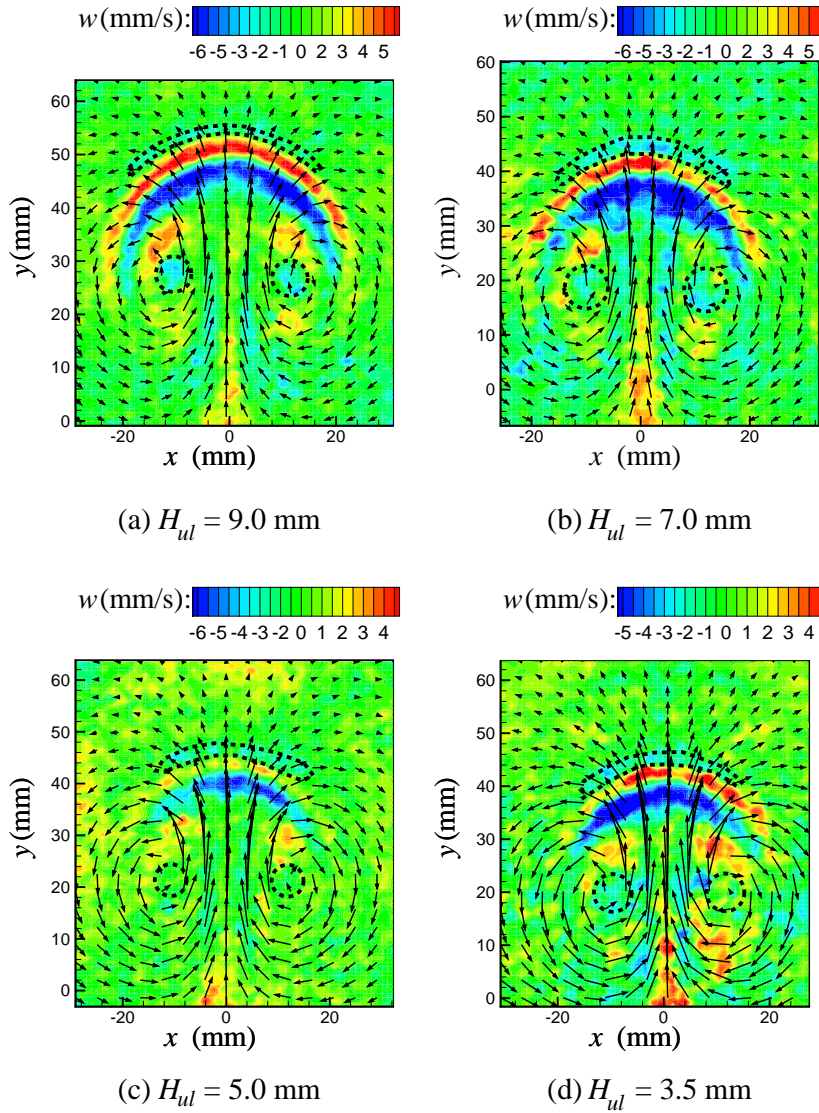


Figure 4.5 – Experimentally obtained velocity fields of a dipolar vortex in a horizontal plane at mid-depth of the top fluid layer having a thickness of (a) $H_{ul} = 9.0$ mm, (b) $H_{ul} = 7.0$ mm, (c) $H_{ul} = 5.0$ mm, and (d) $H_{ul} = 3.50$ mm. The time instants have been chosen such that the second change in vertical velocity inside the vortex cores can be seen as well as the frontal circulation. Meaning of vectors, shades/colours, and dashed contours: see caption Fig. 4.1.

of the velocity field indicate that the magnitude is almost independent of the fluid depth H_{ul} , it is useful to introduce dimensionless numbers to quantify the shallowness of the flow and to compare these with data from the literature. When the flow is electromagnetically generated, the magnet dimension is a measure of the horizontal length scale \mathcal{L} . The geometrical aspect ratio γ is then defined as \mathcal{H}/\mathcal{L} , where \mathcal{H} is a measure of the vertical length scale. In Table II the γ -range for the performed experiments is presented, as well as some typical literature values. Clearly, the aspect ratio of

Table II – Geometrical aspect ratio γ ($=\mathcal{H}/\mathcal{L}$) for the performed two-layer experiments together with literature values. Unless stated otherwise, the cited references employ a stable two-layer fluid setup, with a heavy (dielectric) bottom fluid layer and a lighter conducting top layer.

Refs.	\mathcal{H} (mm)	\mathcal{L} (mm)	γ (-)	Re (-)
Present study	9.0 ~ 3.5	25	0.36 ~ 0.14	1150 ~ 2000
Tabeling <i>et al.</i> [40, 42] ^a	3	8	0.375	200 ~ 400 ^b
Rivera and Ecke [73]	3	12.7	0.24	1200 ^c
Shats <i>et al.</i> [81]	4	5	0.8	100 ^d

^aThe Refs [40, 42] utilize a two-layer setup of NaCl solutions with different densities in a stable configuration, i.e., both fluid layers are electromagnetically driven.

^bIndirectly estimated from references in [40, 42].

^cThe authors provide a Reynolds number of approximately 500 based on the rms velocity fluctuations and injection length scale. Furthermore, they explicitly mention that this rms Reynolds number is four to five times larger than that of Jullien *et al.* [42]. We have therefore conservatively estimated the Reynolds number based on the velocity magnitude for the experiments by Rivera and Ecke to be of the order of 1200.

^dObtained through personal communications with H. Punzmann (ANU, Australia).

cases $H_{ul} = 9.0$ mm ($\gamma = 0.36$) and 7.0 mm ($\gamma = 0.28$) are consistent with the γ -values of Tabeling and co-workers [40, 42] and Rivera and Ecke [73]. Furthermore, the case $H_{ul} = 3.5$ mm ($\gamma = 0.14$) corresponds to a shallower fluid-layer geometry than those reported in the literature. The Reynolds numbers based on a characteristic horizontal velocity scale are presented in the last column of Table II. In the present study, the value of the Reynolds number is approximately five times larger than the cited literature values, therefore the dipole experiences less viscous dissipation. The Reynolds numbers of the present experiments are comparable or slightly higher than that of Rivera and Ecke [73]. Note that Rivera and Ecke [73] explicitly mention that, although their Reynolds number is four to five times higher than that of Jullien *et al.* [42], considerable finite Reynolds number effects

remain that result in deviations from the expectations of theory. Similar concerns were also expressed by Boffetta and Sokolov [11] and recently by Lindborg [56].

4.3.4 Degree of two-dimensionality of shallow dipoles

Qualitatively the 3D structure of the dipolar vortex in the two-layer fluid shows a great resemblance with that seen in the single-layer configuration. Figs. 4.6(a) and 4.6(b) display the numerically and experimentally obtained kinetic energy ratios q , respectively, in order to make a more quantitative comparison of the importance of the 3D flow structure of the coherent vortices between the single and two-layer fluids. The kinetic energy ratio q is

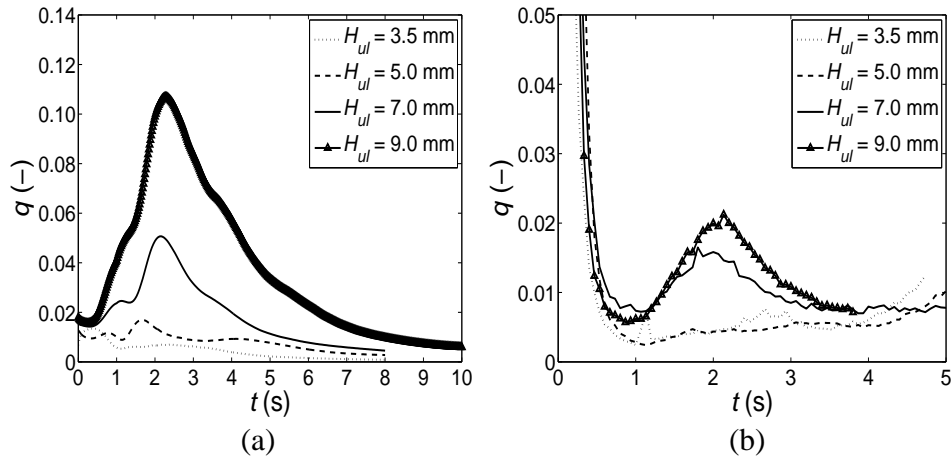


Figure 4.6 – (a) Numerically obtained evolution of the kinetic energy ratio q with varying upper fluid-layer depth H_{ul} . This q -ratio is evaluated at a horizontal plane at mid-depth of the upper layer. (b) Same as (a) except now for the experiments.

defined as the ratio of the kinetic energy contained in the vertical motion to that in the horizontal motionⁱⁱ, evaluated at a horizontal plane at mid-depth in the upper layer. It is observed that the ratio q increases during the forcing (i.e., for $0 < t \leq 1$ s), attains a global maximum at around $t = 2.0$ s, long after the forcing has been switched off, and then decays gradually. An exception to this is the case $H_{ul} = 3.5$ mm (dotted line) for which a global

ⁱⁱNote that for fully developed isotropic turbulence, i.e., u , v , and w -velocity components are of the same order, this ratio $q [=E_V/E_H$, see Eq. (3.6)] would have a value of 0.5.

maximum is attained during the forcing. Clearly, the kinetic energy ratio q decreases with decreasing H_{ul} . For the aspect ratios consistent with Tabeling and co-workers [40, 42] and Rivera and Ecke [73], typical values of the vertical velocity w amount to 30 or 45% of the horizontal velocity magnitude \mathcal{U} . Surprisingly, the typical maximum value of q corresponds with that for the single-layer fluid [i.e., Fig. 3.13(b) in Sect. 3.3.4 shows a maximum q value of approximately 0.13 for $H = 9.3$ mm and $j_x = 0.11$ A/cm²]. Based on the comparison of the ratio q , the two-layer setup does not offer a significant improvement over the single layer setup, in the sense that the vertical flow component contains a substantial amount of kinetic energy.

In Fig. 4.6(b) the experimentally obtained ratio q is presented. Qualitatively, a decrease of kinetic energy ratio q with decreasing H_{ul} is seen and q attains its maximum around $t = 2.0$ s. Apart from the initial time behaviour (where the noise in the vertical velocity distribution is corrupting the ratio q), a fairly good qualitative agreement is seen with Fig. 4.6(a). Here, $w \sim 20\%$ of \mathcal{U} for the corresponding literature values of the aspect ratio γ .

Quantitatively, the difference between the experimentally and numerically obtained kinetic energy ratio q is substantial, which is mainly attributed to the generation of interfacial deformations as indicated in Fig. 4.4. These interface deformations are intimately linked with the local vertical motion and they extract energy from the dipole, most efficiently when the interface Froude number is of order unity, which is the case in our experiments. The potential energy per unit area contained in such an interfacial deformation is of the order $g\Delta\rho A^2$, where A is the amplitude of the deformation [50]. With the area taken as the dipole area, i.e., $\pi(2D)^2$, and a deformation amplitude estimated of the order of 1 mm, this potential energy turns out to be of the same order as the kinetic energy contained in the vertical motion of the complete upper-fluid layer domain. Therefore, when interface deformations are present, the E_V will most likely be substantially lower than in a simulation without interface deformation, thereby reducing the ratio q in the experiment as compared to the simulations.

As discussed in Sec. 4.3.3, the magnitude of the vertical velocity remains approximately constant while the magnitude of the horizontal velocity components increase with decreasing H_{ul} (see Fig. 4.5), thereby reducing the ratio q ($=E_V/E_H$). Additional simulations have been performed for decreasing upper fluid-layer depths while keeping the magnitude of the horizontal velocity field approximately constant (Re-value at the end of the

forcing phase was kept constant at 1250). It turns out that the ratio q obtained from these simulations shows approximately the same magnitude and evolution as depicted in Fig. 4.6(a). Therefore, the kinetic energy ratio q depicted in Fig. 4.6(a) was not biased by the stronger electromagnetic forcing closer to the magnets for decreasing H_{ul} .

In Fig. 4.7 the numerically obtained normalized divergence Λ is displayed for three different evaluation heights inside the upper layer (with depth $H_{ul} = 7.0$ mm). This quantity Λ is computed as

$$\Lambda = \frac{H_{ul} \iint_S |\nabla_H \cdot \mathbf{u}| \, dx \, dy}{D \iint_S |\omega_z| \, dx \, dy}, \quad (4.1)$$

where ∇_H denotes the divergence with respect to the horizontal components and D the magnet diameter. The normalization factor $D \iint_S |\omega_z| \, dx \, dy$ is a measure of the characteristic horizontal velocity. The normalized hor-

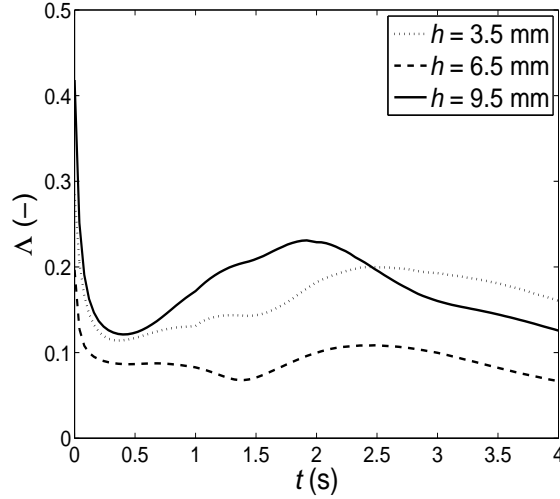


Figure 4.7 – Numerically calculated evolution of the normalized horizontal divergence Λ at three different evaluation levels (3.5, 6.5, and 9.5 mm) inside the upper fluid layer (with depth $H_{ul} = 7.0$ mm). Note that $H_{bl} = 3$ mm, thus the evaluation levels 3.5, 6.5, and 9.5 mm correspond to positions 0.5 mm above the internal interface, 3.5 mm above the internal interface (mid-depth of the top layer), and 0.5 mm below the free surface, respectively.

izontal divergence Λ depicted in Fig. 4.7 is non-zero at all three measurement planes, whereas in purely 2D (incompressible) flow it is by definition zero. The highest Λ -values are observed at the level closest to the surface

($h = 9.5$ mm) and the internal interface ($h = 3.5$ mm) as $|\partial w/\partial z|$ attains its maximum there. At approximately mid-depth of the upper fluid layer $\partial w/\partial z$ is approximately zero, leading to low values of the normalized horizontal divergence. After the forcing phase, the magnitude of Λ is smaller than that of the single-layer case [cf. Fig. 3.15].

4.3.5 Tracer transport at the free surface

To illustrate the effect of the 3D structures inside the shallow fluid layer on motion at the free surface, the transport of massless passive particles is numerically studied. These particles are released at $t = 0$ on a uniformly distributed spatial grid (consisting of 9800 particles in total) at the free surface. Although the vertical velocity is identically zero at the free surface, vertical motions inside the flow do influence tracer transport on this surface, since in general $\nabla_H \cdot \mathbf{v} \neq 0$ at the free surface.

In Fig. 4.8(a) the numerically obtained tracer distribution is shown at $t = 3.75$ s for the 3D simulation, where colours indicate the magnitude of the vertical velocity just below the surface and particle positions by the black dots. As $w = 0$ at the free surface, the tracer particles are bounded to the surface and therefore may accumulate locally. It is clearly seen that the particles become concentrated in narrow bands coinciding with the presence of downward vertical motion below the surface, both at the front and tail side of the dipole. Higher particle concentrations are thus observed in regions where the horizontal flow field is convergent, whereas lower concentration corresponds to locally $\nabla_H \cdot \mathbf{v} < 0$. Note that the normalized horizontal divergence Λ (see Fig. 4.7) attains its maximum close to the free surface.

The horizontal velocity field of an incompressible 2D flow is by definition divergence-free and narrow bands of accumulated particles will therefore not form in this case. This is illustrated by the 2D simulation in Fig. 4.8(b), where a fairly uniform particle distribution is observed. Clearly, caution is needed when interpreting passive tracer transport and dispersion at the free surface of these shallow two-layer setups.

4.4 Conclusions and Discussion

The canonical laboratory setup to study non-rotating 2D turbulence is the electromagnetically driven flow in shallow fluid layers. In the last years, this standard laboratory setup utilized a stable two-fluid layer configuration, with the flow measurements performed at the free surface of the upper layer. This top layer is shielded from the no-slip bottom by a denser fluid layer, thus attempting to minimize the influence of the no-slip bottom on the development of the flow. The question whether this two-layer setup is a significant improvement over the single layer setup has hardly received any attention.

In this chapter, the 3D structures developing in the top layer of a two-fluid layer setup have been examined, both experimentally and with numerical simulations for the generic case of a dipolar flow in a two-layer fluid. Remarkably, these 3D structures and their evolution show a close resemblance with those observed in a single fluid layer. Even for the smallest upper fluid layer thickness (whose geometrical aspect ratio is significantly lower than values of previously reported experimental studies on 2D turbulence utilizing a two-layer fluid) the same 3D structures emerge as in the single-layer fluid.

With the aid of the numerical simulations it is indirectly shown that the development of the frontal circulation is related to deformations of the internal interface. In contrast to reports in literature, the frontal circulation is observed in all the performed two-fluid layer experiments.

Quantities used as indicators for quasi-2D flow behaviour, i.e., the ratio (q) of kinetic energy contained in the vertical motion to horizontal motion and the normalized horizontal divergence (Λ), show a similar evolution and quantitative behaviour as that was previously seen for the same dipolar flow in a shallow single fluid-layer. Based on our observations of the kinetic energy ratio q , the two-layer configuration does not provide a significant improvement over the single-layer setup. Furthermore, passive tracer transport at the free surface shows the emergence of distinct narrow bands of particles, which are related to the non-zero horizontal divergence. As 2D flow is by definition horizontally divergence-free, such narrow bands do not develop in the purely 2D case.

Since the vortex dipole can be considered as a generic flow structure in 2D turbulence, the conclusions of the present study may apply more generally to experimental realizations of 2D turbulence, both for the decaying

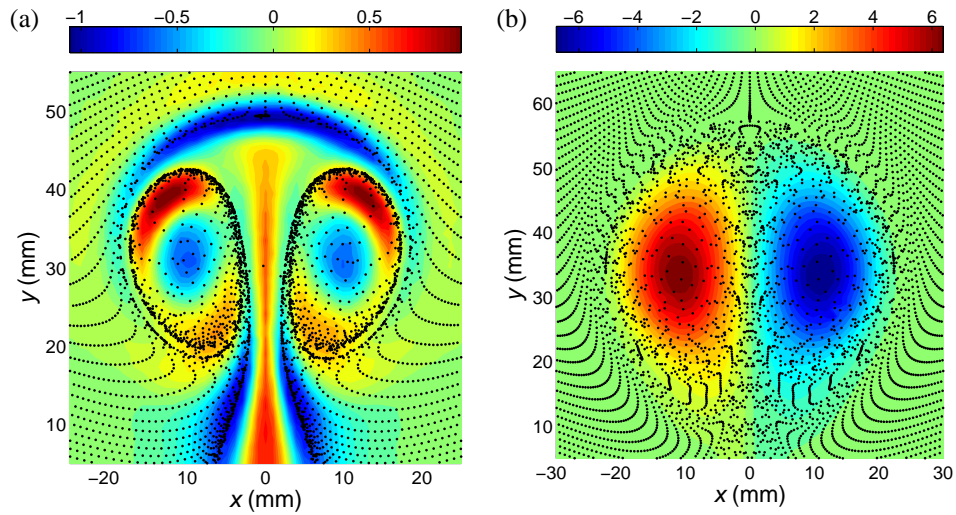


Figure 4.8 – (a) Distribution of tracer particles (black dots) on the free surface of the $H_{ul} = 7.0$ mm simulation at $t = 3.75$ s. Colours indicate the magnitude of the vertical velocity w just below the free surface (at $z = 9.5$ mm). (b) Distribution of tracer particles at $t = 3.75$ s obtained with a 2D simulation, where colours indicate the magnitude of the vorticity ω_z .

and the forced case.

CHAPTER 5

Linear array of vortices

The previous two chapters were focussed on the three-dimensional (3D) structure of a single dipole in a shallow one- and two-layer fluid. The present chapterⁱ is devoted to a qualitative study of the dynamics of a linear array of vortices that interact with a lateral no-slip wall. Our aim is an exploration of the influence of the forcing protocol and the presence of a lateral wall on the three-dimensionality of the flow dynamics and associated passive tracer transport.

The parameter regime to be considered is quite large. It includes aspects like fluid layer depth, forcing length scales (magnet size, inter-magnet distance, magnet-wall distance), and forcing protocols (with a range of amplitudes and frequencies). Therefore the choice is made to consider only a few forcing protocols and to explore the three-dimensionality of the flow and the transport properties on a qualitative level only to map out a limited part of the parameter space by laboratory experiments and numerical simulations. The influence of the 3D flow field (with and without a lateral wall present) on particle dispersion is numerically investigated and a comparison is made of particle dispersion resulting from a purely 2D numerical simulation.

This chapter is organized as follows: Section 5.2 outlines the experimental and numerical details. In Section 5.3 the results of the flow structures

ⁱThe contents of this chapter is to a large extent based on: R.A.D. Akkermans, L.P.J. Kamp, H.J.H. Clercx and G.J.F. van Heijst, “3D Structures and tracer transport by a linear array of vortices near a lateral wall,” (in preparation, 2010).

are presented, focussing on three reference cases. Hereafter, the influence of these 3D flow structures and presence of a lateral wall on tracer transport are presented in Section 5.4. In the final Section 5.5 the results are discussed and the conclusions are summarized.

5.1 Introduction

The properties of quasi-two-dimensional (quasi-2D) multi-vortex systems have been studied extensively, as they exhibit elementary processes taking place in two-dimensional (2D) turbulent flow (see, e.g., [12, 88]). In the laboratory, these quasi-2D flows can be enforced by rapidly rotating homogeneous fluids, fluids with density stratification, and geometrical confinement in shallow fluid layers (or soap films). A review of such quasi-2D vortex systems and ways to generate them in the laboratory environment is presented by van Heijst and Clercx [92].

Most numerical studies on 2D turbulence have been carried out on a square domain (subject to double-periodic boundary conditions) with pseudo-spectral codes [19]. However, simulations on bounded 2D turbulence have revealed the influence of the (no-slip) domain boundaries on the flow evolution in both decaying and forced 2D turbulence [19, 93]. The 2D vortices interact with the no-slip wall, which leads to the formation of thin boundary layers that detach from the lateral wall and roll up to form small vortices containing high-amplitude vorticity. Another example of the influence of a lateral wall is the spontaneous spin-up on non-circular domains (see, e.g., [95]).

Since the early 1980s many of the theoretical and numerical predictions on (unbounded) 2D turbulence have been put to test with laboratory experiments (see, e.g., [66, 68]). However, these laboratory experiments are horizontally bounded by lateral walls and in the vertical direction by a no-slip bottom and a free-surface. For example, Cieslik *et al.* [16] have investigated the collision of a dipolar vortex against a solid vertical lateral boundary, both experimentally and numerically. This work revealed that the lateral domain boundaries further contribute to deviations from 2D behaviour.

In the previous chapters, the single dipolar vortex was studied while far away from lateral walls and therefore dipole-dipole and dipole-wall interactions are absent. Such interactions may affect the 3D motion and dispersion properties of the flow, and is something that needs to be investigated fur-

ther. Therefore, in this chapter a linear array of vortices generated close to a lateral wall is studied.

5.2 Details of laboratory experiments and numerical simulations

The experiments were carried out in the setup outlined in Sect. 2.2.3. As opposed to the previous chapters, a linear array of magnets is now used to generate multiple vortices. The reader is referred to Fig. 2.6 for a schematic of the experimental setup.

The goal of these experiments is to study qualitatively the influence of 3D motions and the presence of a lateral wall on the dispersion properties of the flow. For this purpose, the forcing strength I was varied in time, creating a flow that is dominated by viscous effects or a flow dominated by advection. In the latter case, strong interaction between vortices is expected. Furthermore, experiments are performed with and without a lateral wall present. In Table I the different forcing protocols are presented, together with the Reynolds numbers resulting from these forcing protocols. The Reynolds number Re ($= \mathcal{U}\mathcal{L}/\nu$) is defined by taking the magnitude of

Table I – Parameter values of the applied current $I(t)$ for the experiments with a linear array of vortices together with the Reynolds number Re , the Reynolds number Re_α based on the bottom friction coefficient α , and the Strouhal number Sr for the case with and without a lateral wall present. The magnet diameter D (equal to 25 mm) is taken as a measure of the horizontal length scale \mathcal{L} . The period of the forcing signal is denoted by T and kept constant at 4 s.

Case	$I(t)$ (A)	without wall			with wall		
		Re	Re_α	Sr	Re	Re_α	Sr
I	$0.5 \sin(2\pi t/T)$	350	11	0.44	180	6	0.78
II	$0.5 + 0.5 \sin(2\pi t/T)$	900	29	0.17	600	18	0.26
III	$2.5 \sin(2\pi t/T)$	1350	43	0.11	800	25	0.20
IV	$2.5 + 2.5 \sin(2\pi t/T)$	3400	100	0.05	1600	50	0.10

the maximum horizontal velocity as a measure of the characteristic velocity \mathcal{U} and the diameter of the magnet D as the characteristic length scale \mathcal{L} . The viscosity of the fluid is denoted by ν . The Reynolds number Re_α , based on the bottom friction coefficient α , is defined as $\mathcal{U}/\alpha\mathcal{L}$. This bottom

friction coefficient α is given by $\alpha = \nu(\pi/2\mathcal{H})^2$, under the assumption of a Poiseuille-like flow in the vertical. The Strouhal number Sr is defined as $f\mathcal{L}/U$ where f denotes the forcing frequency. Time is set to zero at the onset of forcing throughout the remainder of this chapter. Depending on the Reynolds number, the flow can exhibit a quasi-periodic response to the flow forcing. When appropriate, the forcing phase will be indicated as depicted

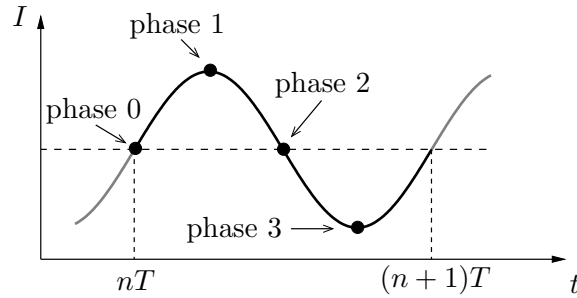


Figure 5.1 – Schematic of the forcing by the sinusoidal current I with indication of 4 different phases within one forcing period T .

in Fig. 5.1, i.e., with phase 0, 1, 2, or 3 when presenting the results.

In the results section three different flow regimes will be studied. These regimes are denoted by case I, III, and IIIw. The latter case is identical to case III with the exception that a lateral no-slip wall is placed on top of the magnets (hence the addition of “w”). For the remaining cases, characteristic snapshots are presented in Appendix A together with a concise explanation. In the following results section only the major differences are stated between the cases presented in the results section and in the appendix.

The fluid layer thickness H has been kept constant at 7 mm for all the experimental results presented in this chapter. In the previous chapters it was shown that qualitatively the 3D flow structures do not change with different fluid depths. Measurements are performed at mid-depth of the fluid layer with the SPIV technique.

In the numerical simulations the free-surface was set to be stress-free and flat, while the bottom was taken to be no-slip, as in the experimental situation. A no-slip boundary condition is applied when a lateral wall is present. These numerical simulations are intended to mimic the experimental configuration. However, to study the influence of the no-slip condition of the lateral wall, additional simulations have been performed where this

wall boundary condition was set to stress-free. For the numerical setup the reader is referred to Chapter 2.

The influence of the 3D flow structure and presence of a lateral wall on the dispersion of particles will be studied only numerically. The particles will be released in different configurations, i.e., on a spatially uniform grid at the free surface or mid-depth of the fluid layer, or periodically released at the wall (if present). Furthermore, the influence of the 3D motions on particle dispersion is illustrated by a comparison with tracer dispersion studies from purely 2D numerical simulations.

5.3 Flow structure of the linear array of vortices

5.3.1 Weak forcing without wall: Case I

Figure 5.2(a) shows plots of the instantaneous vertical (shades/colours) and horizontal (vectors) velocities in a horizontal cross-sectional plane at 3.5 mm above the bottom for $t = 26.0$ s (at phase 1, see Fig. 5.1). In Fig. 5.2(b) the corresponding vertical vorticity component ω_z is displayed. For clarity of presentation the vectors are under-sampled: only one out of three vectors is shown in the x - and in the y -direction, so that approximately 10% of the total set is shown. The position of the magnets is indicated by the dashed circles.

In Fig. 5.2(a) one can recognise counter-rotating vortices in the horizontal velocity vectors as well as dipolar structures in the oppositely-signed patches of vorticity ω_z [as can be recognised in Fig. 5.2(b)]. Downwelling is concentrated inside the vortex cores [see Fig. 5.2(a)], whereas weaker regions of upwelling are present in the tails of the dipoles, similar to what can be observed in Fig. 3.1(a,b) for the single dipole. The downward motion inside the vortex cores is related z -dependent horizontal velocity field (in this situation due to the decay of the magnetic field with height), which introduces a vertical pressure gradient that drives a downward motion (as discussed in Chapter 3). In the early stages after the onset of forcing, the velocity field lags behind the applied current due to the fluid inertia. This time-lag remains hereafter constant at approximately 1 s.

The vertical component of the vorticity ω_z is depicted in Fig. 5.2(b). Patches of alternating vorticity ω_z are seen. As the magnets are positioned in an alternating order, a linear array of vortices is created that is “chained”

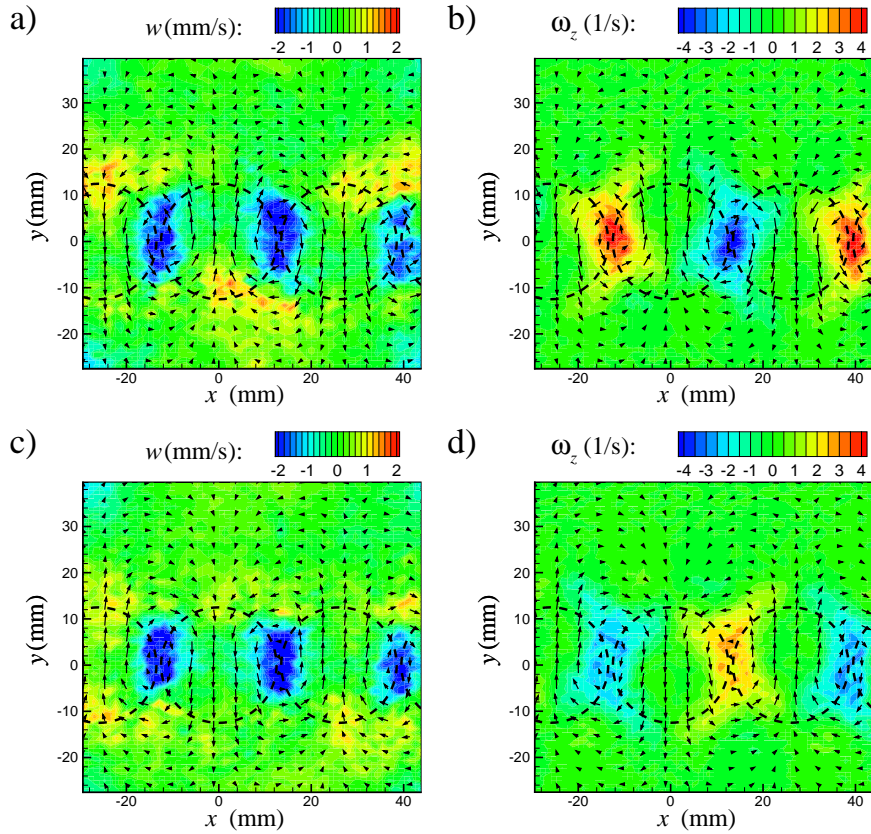


Figure 5.2 – The top panels show experimentally obtained snapshots of case I at $t = 26.0$ s (phase 1) showing (a) the vertical velocity w in colour/shade and (b) the vertical vorticity ω_z in colour/shade at $z = 3.5$ mm. Vectors indicate the horizontal velocity field. The magnet locations are denoted by the dashed circles. The second row of figures represents the situation at $t = 28.0$ s (at phase 3, i.e., half a forcing period later than the first row).

together. The dipoles that are created do not propagate due to the combined effect that the vortices are chained together and the rather low Reynolds number.

The flow field at half a forcing period later is depicted in the second row of Fig. 5.2. The flow and vorticity distribution are approximately reversed as compared to the upper row of Fig. 5.2, except for the vertical velocity component w . The vertical dependence of the horizontal velocity field (and therefore the vertical velocity) remains the same half a forcing period later.

As a comparison, the numerically obtained snapshots are displayed in Fig. 5.3 for the same time instant as the upper row of Fig. 5.2. A good quan-

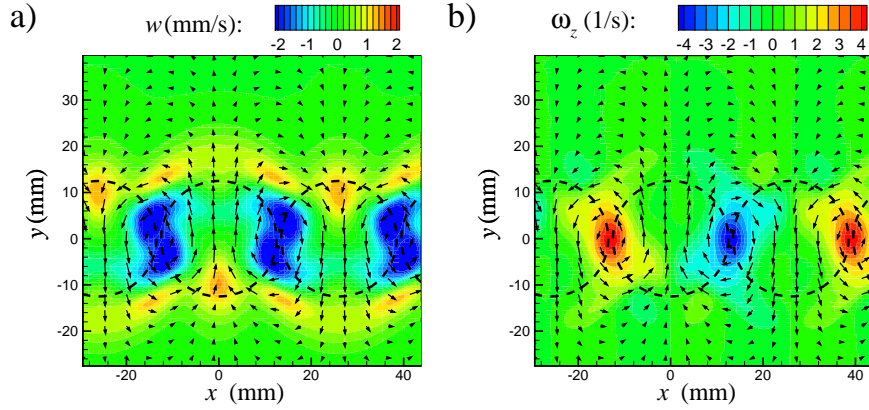


Figure 5.3 – Numerically obtained snapshots of case I at $t = 26.0$ s showing (a) the vertical velocity w in colour/shade and (b) the vertical vorticity ω_z in colour/shade at $z = 3.5$ mm. See Fig. 5.2 for meaning of vectors and colours.

titative similarity is seen between the numerical and experimental snapshots, although the regions of upward motions at the edges of the magnet are less pronounced in the experiments [cf. Figs. 5.3(a) and 5.2(a)]. Also the numerically obtained flow evolution during a forcing period shows good agreement with the experiments.

The global response of the flow to the varying electromagnetic forcing is illustrated in Fig. 5.4, which shows the time evolution of kinetic energies E_H and E_V , defined as

$$E_H = \frac{1}{2}H \iint_S \rho(u^2 + v^2) dx dy \quad \text{and} \quad E_V = \frac{1}{2}H \iint_S \rho w^2 dx dy. \quad (5.1)$$

Integration is performed over a horizontal plane S , in this case the measurement plane $z = 3.5$ mm and the fluid depth H is used as a measure of the vertical length scale. Since one expects a scaling of the vertical kinetic energy E_V with $(H/D)^2$ (i.e., $w \sim uH/D$), the scaled version $(D/H)^2 E_V$ is depicted in Fig. 5.4. Both E_H and E_V are in phase, and after an initial transient period a quasi-periodic response of the kinetic energies is seen. The observed frequency of E_H and E_V (0.5 Hz) is twice the forcing frequency. It turns out that the velocity field shows a frequency response equal to the forcing frequency, and due to the definition of E_H and E_V a doubling results. Furthermore, the large quantitative difference between E_H and E_V

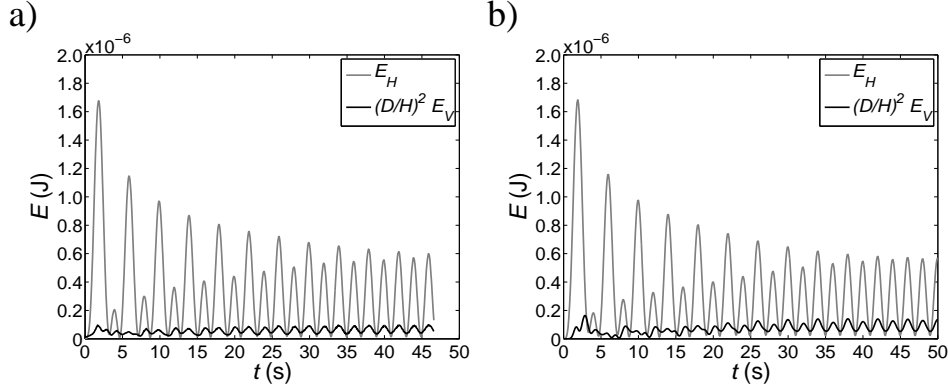


Figure 5.4 – Experimentally (a) and numerically (b) obtained time evolution of the kinetic energies E_H and E_V for case I.

contradicts the common assumption that the vertical motion scales with the horizontal motion proportional to the aspect ratio H/D , as was already seen for the dipolar vortex in a single fluid layer (see Chapter 3). Recently, Duran-Matute *et al.* [29] came to a similar conclusion for the case of a decaying axisymmetric monopole. Comparison of the experimentally obtained kinetic energy components E_H and E_V with the numerical ones [see Fig. 5.4(b)] reveals an excellent quantitative agreement.

Case Iw, i.e., identical to case I but with a lateral wall present, shows similar results as case I (see Appendix A for experimentally obtained snapshots). The influence of the lateral wall is mainly seen in the ω_z vorticity, where near the wall the emergence of oppositely signed vorticity with respect to the sign of ω_z in the vortex cores is seen. Also the flow velocities are lower, which is the result of the presence of a lateral no-slip wall that introduces extra dissipation.

For the weak forcing case with offset, i.e., case II with $I = 0.5 + 0.5 \sin(2\pi t/T)$ A, characteristic snapshots of the flow evolution are given in App. A. A consistent mean flow is created as a result of the forcing offset, and a jet-like flow is observed with superimposed dipolar vortices. The dipoles propagate and dipole-dipole interaction can be observed. After approximately 10 s, the flow loses its temporal periodicity.

When a wall is present, i.e., case IIw (see characteristic snapshots in App. A), the flow remains periodic in time, although slight distortions are seen at later times.

5.3.2 Strong forcing without wall: Case III

In Fig. 5.5 the flow evolution of case III is shown with the velocity field (left column) and the vertical component of the vorticity ω_z (right column). The first, second, and third row correspond to time instances $t = 1.7$ s, $t = 28.0$ s, and $t = 44.0$ s, respectively.

In Fig. 5.5(a) the flow structure is displayed 1.7 s after the forcing has been switched on. Clearly seen are the multiple dipolar structures, which show a striking resemblance with the flow field already observed in the case of a single dipole in a homogeneous shallow fluid layer (see Chapter 3). Compared to case I, the magnitudes of the velocities are higher (as the forcing is stronger) and the dipoles start to propagate. After some time, the quasi-periodicity that was present in Case I is broken, as observed in Fig. 5.5(c). At an even later stage in the evolution, the temporal periodicity of the flow field remains broken. However, dipolar vortex structures can still be recognised [see Fig. 5.5 (e)]. Furthermore, multiple band-like structures are seen in the left column of Fig. 5.5. Adjacent bands of up- and downward motion suggest the presence of numerous horizontal roll-like structures having significant horizontal vorticity. Note that locally the magnitude of the vertical velocity far exceeds the magnitude of the horizontal velocity components (with approximately a factor of two). Figures 5.5(b), (d), and (f) show the evolution of the vertical vorticity ω_z . During the evolution, the formation of thin filaments of high-amplitude ω_z vorticity is seen.

The numerically obtained flow evolution of case III is presented in Fig. 5.6 at the same time instants as for the experimentally obtained snapshots shown in Fig. 5.5. Clearly, a good qualitative agreement exists between the velocity and vorticity distribution of the numerical simulation (as seen in Fig. 5.6) and the experimentally obtained snapshots shown in Fig. 5.5. In Fig. 5.6(c) the snapshot is depicted after the temporal symmetry is broken in the field of view, which happens around $t = 25$, slightly earlier than in the experiments. Although quantitatively some differences are present, qualitatively the same flow evolution is seen in the numerical simulations and the experiments.

Figure 5.7 shows numerically obtained vertical slices of the horizontal vorticity component ω_x in the plane defined by $x = 0$, for the same three time instances as Fig. 5.6. In Fig. 5.7(a), the bottom boundary layer is clearly seen as well as the patch of positive ω_x associated with the downwelling inside the vortex core. At the front side of the dipole (around $y = 28$ mm), the detachment of the bottom boundary layer can be seen,

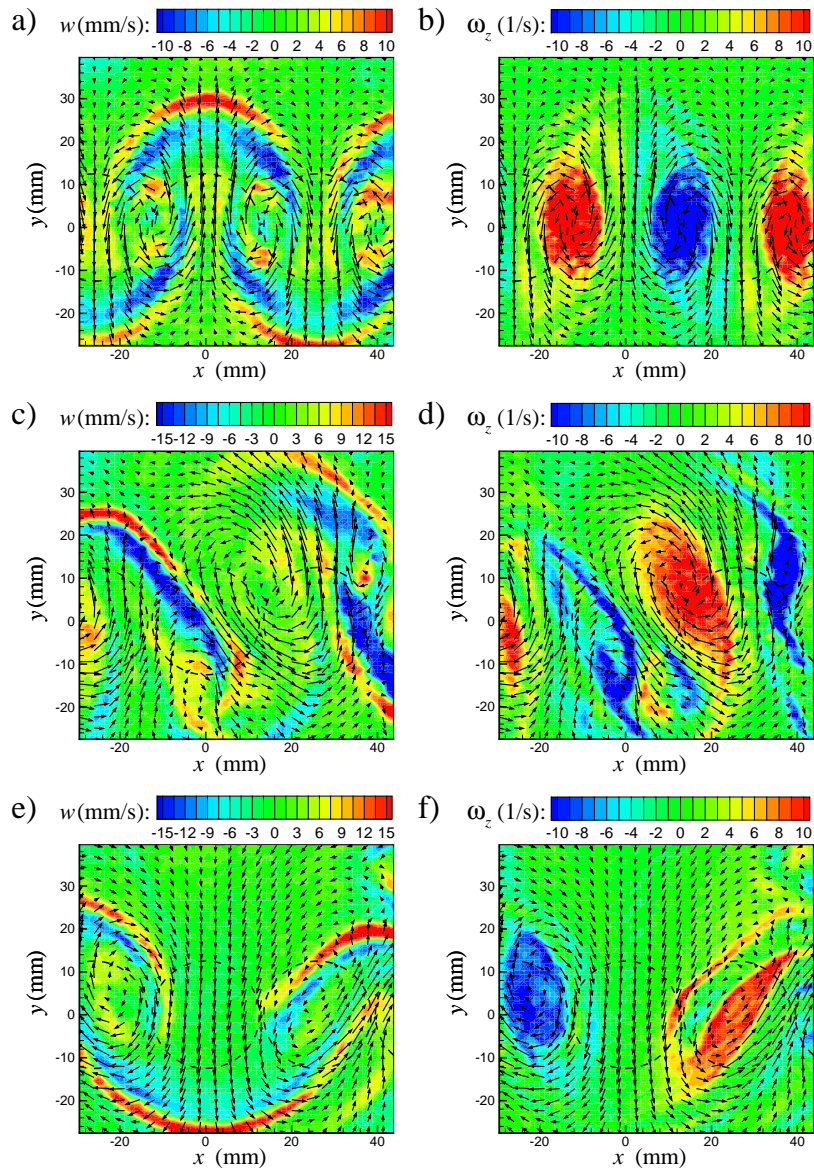


Figure 5.5 – Experimentally obtained snapshots for case III. Vectors indicate the horizontal velocity field. Vertical velocity w (a) and vorticity ω_z (b) in colour/shades at $t = 1.7$ s. The second and third row: same as (a) and (b) except now for $t = 28.0$ s and $t = 44.1$ s, respectively.

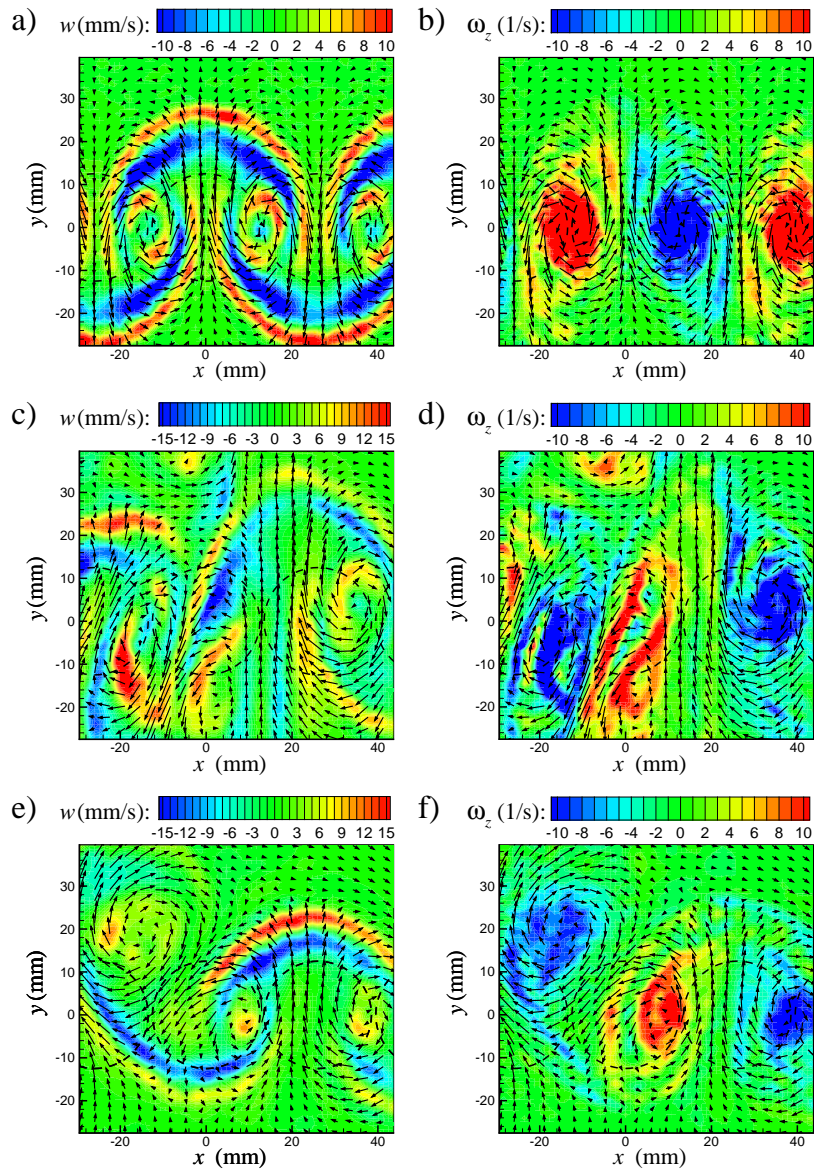


Figure 5.6 – Numerically obtained snapshots of case III. Vectors indicate the horizontal velocity field. Vertical velocity w (a) and vorticity ω_z (b) in colour/shades at $t = 1.7$ s. The second and third row: same as (a) and (b) except now for $t = 28.0$ s and $t = 44.1$ s, respectively.

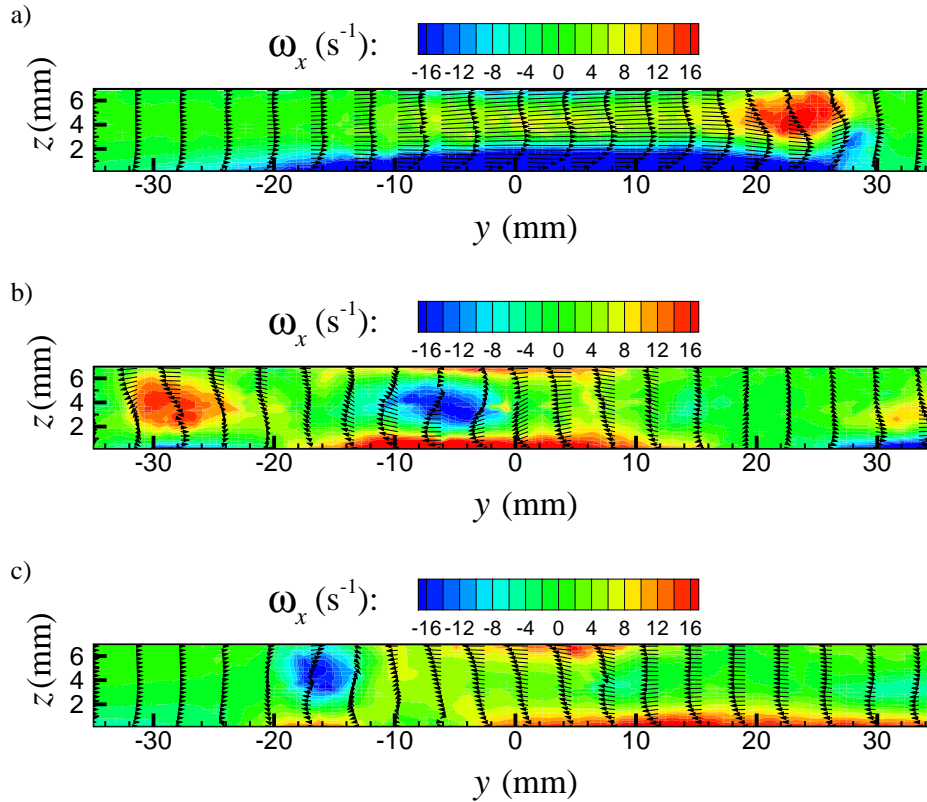


Figure 5.7 – Numerically obtained vertical slices (at $x = 0$) of the horizontal vorticity component ω_x (colour) and in-plane velocity vectors for case III at (a) $t = 1.7$ s, (b) $t = 28.0$ s, and (c) $t = 44.1$ s. The magnet is centred at $y = 0$ and has a diameter of 25 mm.

which at later times during the evolution will form the frontal circulation (see Chapter 3). In the second snapshot, several horizontal vorticity (ω_x) patches are observed. Furthermore, the vertical structure of the in-plane velocity can hardly be assumed to have a Poiseuille-like profile in the vertical direction. In the last vertical slice, see Fig. 5.7(c), significant ω_x patches are seen near the boundaries and inside the fluid layer. During the complete evolution, the maximum of the magnitude of the horizontal vorticity component ω_x is comparable to or even exceeds that of the “primary” vorticity component ω_z (i.e., $\omega_x \approx 2\omega_z$). Furthermore, comparison of Fig. 5.7 with Fig. 5.6 indeed confirms that adjacent bands of up- and downward motion

coincide with roll-like structures containing significant horizontal vorticity ω_x .

In chapter 3, the development of 3D motion inside the dipole was related to a vertical dependence of the horizontal flow field. The type of boundary conditions, vertical confinement of the flow, and vertical gradients in the forcing inevitably lead to such vertical variations in experimentally realised shallow flows. For the linear array of vortices configuration subject to a strong forcing (case III), the combined effect of vertical confinement and magnetic field are the cause of a z -dependent horizontal velocity field which results in the development of 3D motionsⁱⁱ.

The experimentally and numerically obtained time evolution of the horizontal and vertical kinetic energy for case III are displayed in Figs. 5.8(a) and (b), respectively. In Fig. 5.8(a), a buildup of E_H is seen (after an initial

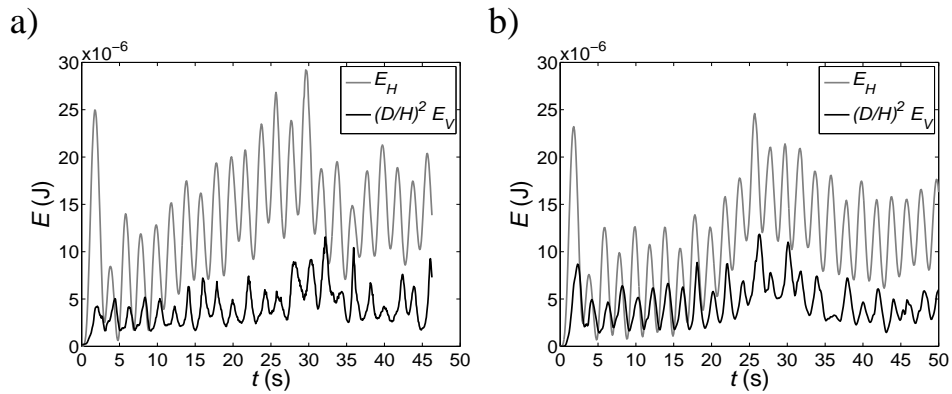


Figure 5.8 – Experimentally (a) and numerically (b) obtained time evolution of the kinetic energies E_H and E_V for case III.

peak) until approximately $t = 30$ s, after which a substantially lower value is observed, which remains approximately constant. A quasi-periodicity of E_H and E_V is seen with a period of 2 s (the flow field has a temporal response equal to the forcing period, due to the definition of E_H and E_V this becomes 2 s). The energy contained in the vertical motion remains approximately constant. Comparison of these experimentally obtained horizontal and vertical kinetic energies with the numerically obtained ones, i.e.,

ⁱⁱThe previously considered case I (weak forcing), represents an anomaly in the sense that the dipolar vortices do not propagate (and therefore remain above the magnets) and are continuously subjected to the influence of the electromagnetic forcing which introduces the downwelling inside the vortex cores.

Figs. 5.8(a) and (b) reveals a good resemblance, although the second peak value in E_H occurs slightly earlier in time for the simulation, at around $t = 25$ s. The magnetic field (and thus the Lorentz force) is known up to a multiplicative factor in the numerical simulations. This factor is determined by matching the numerically observed maximum vorticity at a certain time instant with the corresponding experimental one (see Section 2.3.1). As this matching is not exact, such minor differences between the experimental and numerical kinetic energy evolution result.

One could be tempted to conclude that the flow behaviour is quite two-dimensional based on the small amount of energy contained in the vertical motion as compared to the horizontal ones. Locally, however, the magnitude of the vertical motion exceeds the horizontal one significantly (approximately a factor of two). This locality is lost in global quantities such as E_V and E_H .

Case IV, which is identical to case III but with an offset in the time-periodic forcing [i.e., $I = 2.5 + 2.5 \sin(2\pi t/T)$ A] shows a similar flow behaviour as case III. The flow is dominated by advection, and a consistent mean flow is present (see App. A for characteristic snapshots of case IV).

5.3.3 Strong forcing with wall: Case IIIw

Case IIIw corresponds to the same situation as previously discussed except now a lateral wall is present. Characteristic snapshots of this case are presented in Fig. 5.9. A periodic generation of dipoles is seen, which propagate away from the lateral wall, as illustrated in Fig. 5.9(a). Exactly half a forcing period later, this pattern is repeated at the adjacent magnet position. Production of oppositely signed vorticity at the no-slip wall is seen in Figs. 5.9(b) and (d). Note that the dipoles do not propagate out of the field of view, as they decay quite rapidly.

When comparing this case IIIw with the corresponding case without a lateral wall, it is seen that the horizontal length scale is reduced with approximately a factor of two [cf. Figs. 5.9(a) and 5.5(a)]. The production of vorticity during the initial flow evolution is proportional to $\partial B_z / \partial x$, where B_z is the vertical component of the magnetic field. Vorticity is therefore produced predominantly at the edges of the disk-shaped magnet where $|\partial B_z / \partial x|$ attains its maximum. With a lateral wall present, the vorticity is no longer generated at the edges of the magnet $\pm 0.5D$ at $y = 0$, but at some value $y > 0$ where these edges are closer together, thus reducing the

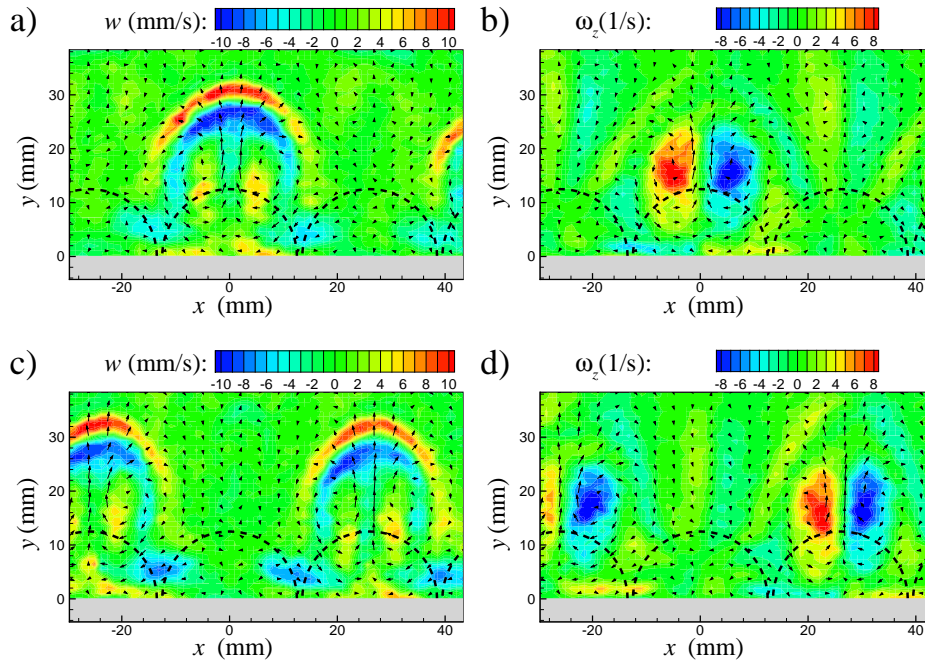


Figure 5.9 – Experimentally obtained snapshots of case IIIw showing (a) the vertical velocity w in colour/shades and (b) the vertical vorticity ω_z in colour/shades at $t = 10.5$ s (phase 2). Vectors indicate the horizontal velocity field. The magnet locations are denoted by the dashed semi-circles. The lateral no-slip wall is located at $y = 0$. (c,d) same as (a,b) except now for $t = 12.5$ s (phase 0).

size of the dipole. A second effect that may also play a role in the smaller

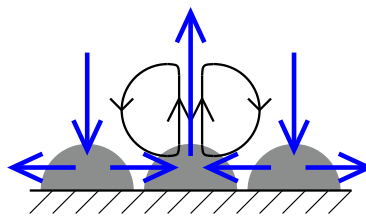


Figure 5.10 – Schematic of the influence of the lateral wall on the size of the dipolar vortex: a converging flow near the lateral wall which causes the smaller dipole size. Magnets are denoted by the gray semi-circles, the induced flow is indicated with blue arrows.

dipole size is that because of the presence of the lateral wall, locally a con-

verging flow is created, which squeezes the dipole, hence reducing its size [see Fig. 5.10]. When a lateral wall is absent, the locally converging flow is not present.

The numerically obtained velocity and vertical vorticity for case IIIw are presented in Fig. 5.11(a) and 5.11(b), respectively. A striking resemblance is seen with the upper row of Fig. 5.9. However, the vertical vorticity gener-

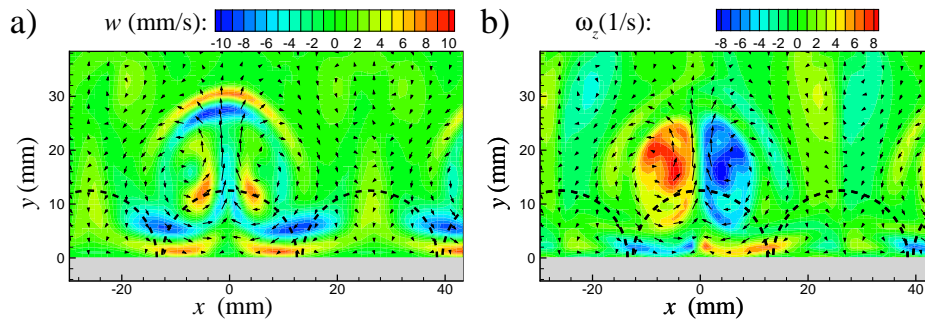


Figure 5.11 – Numerically obtained snapshots of case IIIw showing (a) the vertical velocity w in colour/shades and (b) the vertical vorticity ω_z in colour/shades at $t = 10.5$ s. Vectors indicate the horizontal velocity field. The magnet locations are denoted by the dashed semi-circles. The lateral no-slip wall is located at $y = 0$.

ated near the lateral wall is much more pronounced and significantly larger than in the experiment. This is attributed to the averaging effect of gradients in the velocity field (and therefore also vorticity ω_z) inside correlation windows by the SPIV technique [71]. A qualitative difference between the experiment and simulation is the presence of a concave meniscus of the fluid at the lateral wall in the former. The influence of this meniscus was tested with an experiment where no detergent was added to the fluid: this resulted in no appreciable difference with the experiments where detergent was added.

In Fig. 5.12 two vertical slices are displayed of the in-plane ω_x vorticity component for case IIIw. The vertical plane defined by $x = 5$ mm is chosen such that it cuts approximately through one of the vortex cores. The two snapshots correspond to two succeeding extrema in the forcing, as then there is locally strong forcing near the wall. In Fig. 5.12(a) the vorticity distribution is shown when the forcing is directed in the positive y -direction. The bottom boundary layer and the positive ω_x patch at the front side of the dipole (at $y \approx 18$ mm) are clearly visible. Furthermore, near the lateral wall (the blue patch at $y \approx 4$ mm) a vorticity patch of high-amplitude ω_x can be recognised, indicating strong motion away from

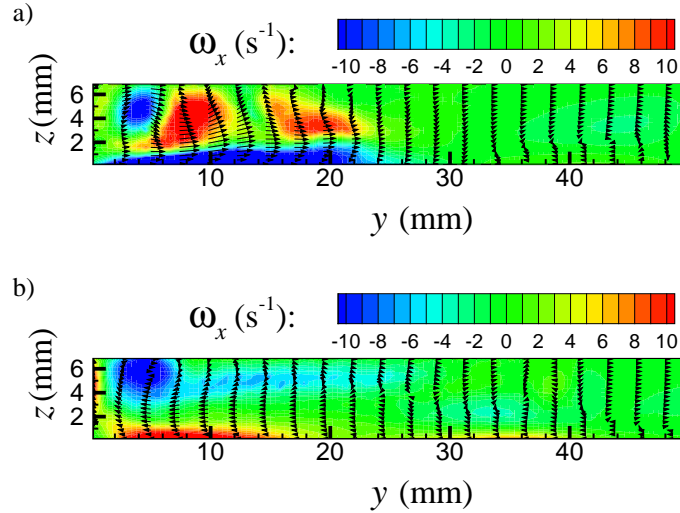


Figure 5.12 – Numerically obtained snapshots of vertical slices (defined by $x = 5$ mm) of the horizontal vorticity component ω_x (colour) and in-plane velocity vectors of case IIIw for (a) $t = 13.5$ s (phase 1) and (b) $t = 15.5$ s (phase 3).

the wall at the surface. In the second snapshot of Fig. 5.12, the flow field is presented when the forcing is directed in the negative y -direction, i.e., towards the lateral wall. A negative ω_x vorticity patch (blue) is observed at approximately $y = 4$ mm, once again indicating motion away from the lateral wall at the surface. It turns out that locally near the wall, a diverging flow field is present at the surface. Furthermore, a thin patch of high amplitude is present almost at the wall at $y = 0$.

Additional simulations, where the lateral wall was set to a stress-free boundary condition as opposed to the above described no-slip lateral wall, returned quantitatively similar results. However, thin high-amplitude ω_x vorticity patches at the lateral wall resulting from the no-slip boundary condition are not seen anymore in the stress-free wall simulation.

In Fig. 5.13 the time evolution of the kinetic energies contained in the vertical and horizontal flow components are presented. Contrary to the numerical result, the experimentally obtained E_H slightly decays in time. The simulations where the lateral wall was set to be stress-free resulted in a similar quantitative evolution of these kinetic energies (not shown) as obtained with a lateral no-slip wall.

Case IVw (see App. A for characteristic snapshots), which is identical to

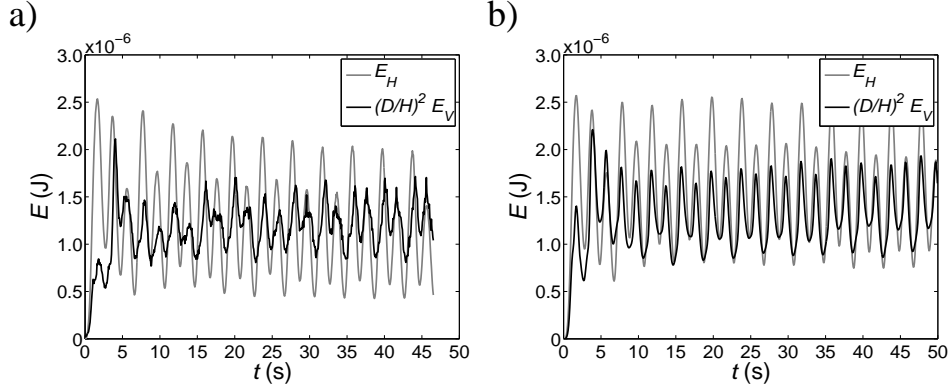


Figure 5.13 – Experimentally (a) and numerically (b) obtained time evolution of the kinetic energies E_H and E_V for case IIIw.

case IIIw but with an offset in the forcing [i.e., $I = 2.5 + 2.5 \sin(2\pi t/T)$ A], shows initially a jet-like flow with dipolar vortices superimposed. Already after the second forcing the temporal periodicity is lost for this case and vortex-vortex and vortex-wall interactions are observed (see second row of Fig. A.5 in App. A).

5.3.4 Influence of the lateral wall: averaged kinetic energy

To study the influence of the lateral wall in a more quantitative way, an “average” kinetic energy e is considered, i.e.,

$$e(y) = \frac{1}{(T_{end} - T_{begin})} \cdot \int_{T_{begin}}^{T_{end}} \frac{1}{L} \int_0^L \frac{1}{2} (u^2 + v^2 + w^2) dx dt, \quad (5.2)$$

evaluated at mid-depth of the fluid layer ($z = 3.5$ mm). This kinetic energy is spatially averaged in the x -direction (i.e., parallel to the lateral wall in case IIIw) and temporally averaged over the entire recording time T_{end} (in most practical situations T_{begin} can be set to zero). This kinetic energy e thus provides information on how the kinetic energy is distributed as a function of the y -direction. In Fig. 5.14 the quantity e is plotted for (a) case I and (b) case III. For the lower forcing situation [case I, see Fig. 5.14(a)] e is symmetrically distributed around $y = 0$ and confined to the region $|y| < D$. In Fig. 5.14(b) the average kinetic energy e for case III is presented, which is fairly symmetric around $y \approx 0$. The peak value e_{\max} is significantly higher,

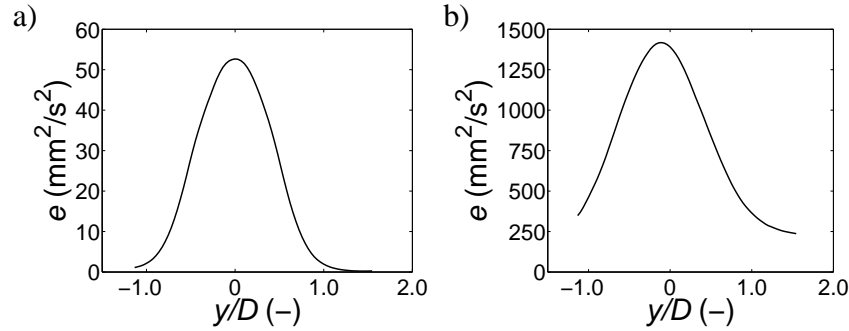


Figure 5.14 – Experimentally obtained average kinetic energy $e(y)$ for (a) Case I, (b) case III.

i.e., 25 times as compared to case I, which corresponds to the squared ratio of the maximum current strength of case III and case I.

With the lateral wall present a significant reduction of e_{\max} is observed [cf. Fig. 5.15(a) and Fig. 5.14(b)] as a result of the dissipation near the lateral no-slip wall. Furthermore, $e(y)$ now shows two distinct peaks. The first peak results from the strong boundary-layer motion near the lateral wall and the second from the dipole that propagates away from this wall. In Fig. 5.15(b) the phased average kinetic energy e' is presented, i.e., taking

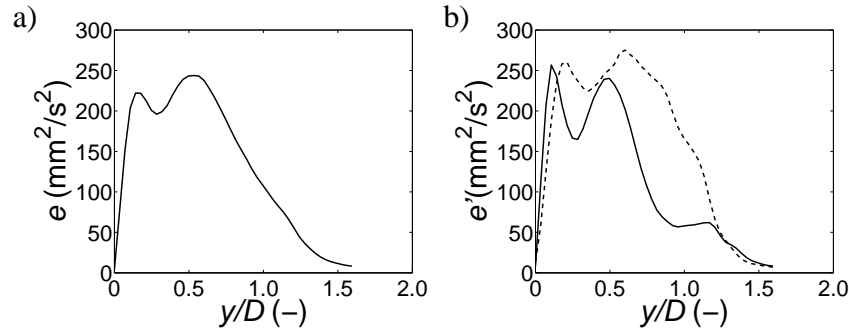


Figure 5.15 – Experimentally obtained (a) average kinetic energy e for case IIIw and (b) phase-averaged kinetic energy e' for case IIIw. In the latter figure, the solid and dashed line indicate phase 1 and phase 0, respectively.

into account the phase of the forcing current I . This phase average kinetic

energy e' is computed as

$$e'(y) = \frac{1}{N_{ph}} \sum_i \left[\frac{1}{L} \int_0^L \frac{1}{2} (u_i^2 + v_i^2 + w_i^2) dx \right] \quad i = 1, \dots, N_{ph}, \quad (5.3)$$

where N_{ph} denotes the number of sample sets of the considered phase. The generation of the dipole near the wall is indicated by the solid line (phase 1, see Fig. 5.1), afterwards the dipole starts to propagate away from the wall. The dashed line illustrates the transport of kinetic energy away from the wall (during phase 0). Numerically obtained averaged kinetic energies e' (not shown) showed quantitative similar results.

For case IIIw, the dipole dissipates before it propagates out of the field of view. Therefore, the dissipation length is smaller than 35 mm. Also a theoretical estimate can be made of the dissipation length ℓ_α , based on the bottom friction coefficient α and the characteristic advection speed of the dipole \mathcal{U}_{adv} , i.e., $\ell_\alpha = \mathcal{U}_{adv}/\alpha$. This theoretical dissipation length (≈ 50 cm) turns out to be much larger than the experimentally observed dissipation length. It is assumed that 3D motions and the continuously time-varying forcing are the cause of this lower value of the dissipation length in the experiments and numerical simulations, thus once again underlining the substantially more complex 3D flow dynamics in the thin fluid layer.

5.3.5 Degree of two-dimensionality for the linear array of vortices

In a similar way as in the previous chapters, the ratio q ($=E_V/E_H$) is used to quantify the importance of vertical motion. In Fig. 5.16 the experimentally obtained q -ratios are presented for the different cases. For the cases I and Iw, q is displayed in Fig. 5.16(a). Besides the average low value of q , peaks with a period of 2 s are present in the evolution which correspond to the instants where E_H attains its minima. Apart from the peaks, it is seen that the kinetic energy ratio is higher when a lateral wall is present. In Fig. 5.16(b) the q -ratio is presented for case II and case IIw. With a mean flow present, resulting from the electrical current offset [$I = 0.5 + 0.5 \sin(2\pi t/T)$], the average value of the q -ratio is slightly below the corresponding ones in Fig. 5.16(a). Only at later stages of the evolution an oscillatory response of the kinetic energy ratio q is seen. Figure 5.16(c) shows the results for case III and IIIw. Noticeable is that the situation with the presence of a

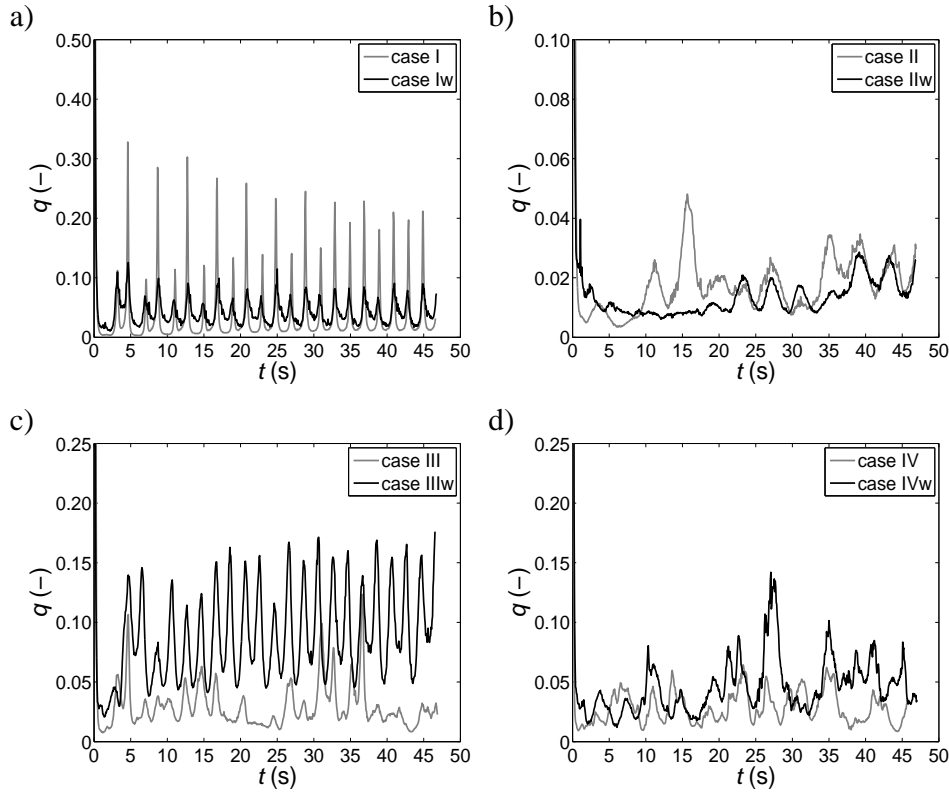


Figure 5.16 – Experimentally obtained evolution of the kinetic energy ratio q for (a) cases I and Iw [$I=0.5 \sin(2\pi t/T)$ A], (b) cases II and IIw [$I = 0.5 + 0.5 \sin(2\pi t/T)$ A], (c) cases III and IIIw [$I = 2.5 \sin(2\pi t/T)$ A], and (d) cases IV and IVw [$I = 2.5 + 2.5 \sin(2\pi t/T)$ A].

lateral wall (case IIIw) is much more 3D than without a wall. A periodic response of 2 s is observed of the flow in the q -ratio. For the case with the high forcing with offset, i.e., case IV and IVw, the q -ratio is depicted in Fig. 5.16(d). With a wall present the q -ratio is slightly higher than without wall.

Generally, it can be concluded that for the cases without a forcing offset (the left column of Fig. 5.16), there is a significant increase of the kinetic energy ratio q when a lateral wall is present. When a forcing offset is present, as shown in the right column of Fig. 5.16, there is no significant difference between the situation with or without a lateral wall. The forcing offset creates a consistent mean flow ($E_H \gg 0$) which dominates over the (local)

influence of the lateral wall. Due to the presence of a mean flow, also the average values of q are lower than without a forcing offset. However, for the cases without a forcing offset (left column of Fig. 5.16), a significant increase of the kinetic energy ratio q is observed for the cases with and without a lateral wall (i.e., approximately 4 times higher with a wall present).

5.4 Tracer transport by a linear array of vortices

In the preceding section, it was seen that inside the fluid (locally) strong vertical motions are present in all of the considered cases. In this section the effect of this three-dimensionality on the transport of tracers is studied numerically. Special attention is paid to the influence of a lateral wall on the dispersion behaviour of the near-wall flow.

5.4.1 Dispersion at low Reynolds number; case I

In order to study the transport properties of the linear array of vortices, passive tracer particles were released at $t = 0$ on a uniform planar grid (i.e., $-25 \leq x \leq 25$ mm and $-25 \leq y \leq 25$ mm comprising of 10,600 particles) at the free surface of the fluid layer. Note that the particles are bound to this free surface as there the vertical velocity is identically zero. Figure 5.17 displays snapshots of the tracers distribution for case I (i.e., a weakly forced flow dominated by viscosity). Bands of higher concentration of particles are seen to be formed in regions where the surface flow is convergent, see Fig. 5.17(a). During the early stages of the flow evolution, there is on average a diverging flow inside the vortex cores, as can be observed by a depletion of particles. However, at later stages of the flow evolution, the flow inside the vortex cores is (on average in time) converging due to the local downwelling of the fluid and a large part of the particles thus concentrate there. This is illustrated in Fig. 5.17(b), where approximately 88% of the initially released particles is now concentrated in the two vortex cores. Despite the low Reynolds number of the flow and small magnitude of the vertical velocity component, a drastic effect is seen of the 3D structure of the flow on tracer transport at the surface.

The origin of this depletion or agglomeration of particles is illustrated in Fig. 5.18. This figure shows a side view of the flow near the free sur-

face. When there is downwelling underneath the free surface, the flow field at the surface must be convergent (note that the full 3D velocity field is incompressible and therefore divergence-free, however, at the surface the horizontal velocity field is in general not divergence-free). Particles are advected by this locally converging flow, however, the particles are bound to the surface as w is identically zero there. Therefore, an accumulation of particles is expected in regions where $\nabla_H \cdot \mathbf{v} < 0$. The opposite happens in diverging flow regions, where $\nabla_H \cdot \mathbf{v} > 0$, particles are transported away from diverging regions and typically a depletion is observed there.

5.4.2 Influence of 3D motion; case III

In Fig. 5.19 the numerically obtained distribution of particles that were initially released at the free surface is presented for case III at $t = 12.5$ s. These particles were released at the free surface on a uniform grid (i.e., $-52 \leq x \leq 52$ mm and $-50 \leq y \leq 50$ mm consisting of 21,200 particles), and subsequently advected by the velocity field at the surface. Already during the first forcing period, the formation of band-like structures is seen, which coincide with regions of converging flow ($\nabla_H \cdot \mathbf{v} < 0$). After the first forcing period the majority of the particles is concentrated in these band-like structures, which align with the propagation direction of the dipoles (i.e., in the y -direction). At later stages of the evolution, there is also considerable advection of these band-like structures in the x -direction. Comparison of Fig. 5.19 with Fig. 5.17(b) reveals a striking influence of the forcing protocol on the dispersion of particles at the surface.

Figure 5.20 shows numerically obtained snapshots of particles which are initially released at mid-depth of the fluid layer for case III; these particles are thus advected by all three-components of the velocity field. In the snapshot of Fig. 5.20(a), taken just after the onset of the forcing, one clearly sees the positions of the two vortex cores as these are characterized by downward motion. Soon after, the particles are dispersed over the entire height of the fluid layer, as illustrated in Fig. 5.20(b). Later in time, also considerable transport in the x - and y -directions is observed.

This rapid vertical mixing of the particles is quantified in Fig. 5.21. Here, the standard deviation of the particle z -locations, denoted by σ_z , is

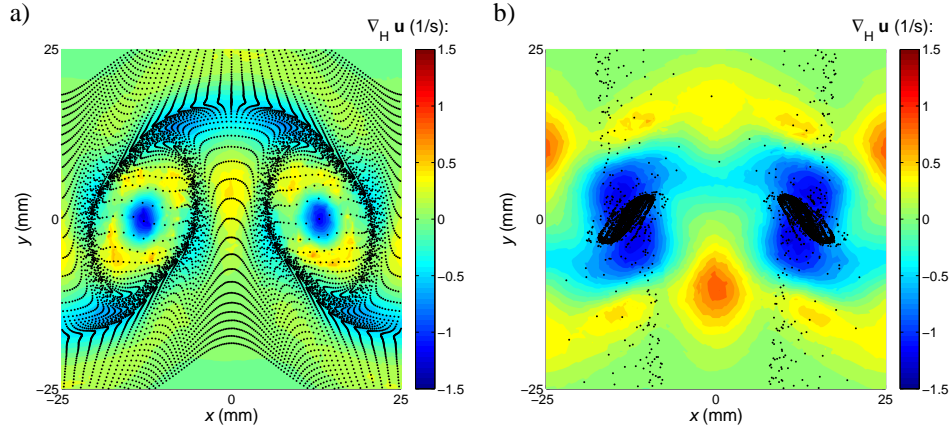


Figure 5.17 – Numerically obtained snapshots of the tracer distribution at (a) $t = 4.0$ s (i.e., $t = T$) and (b) $t = 26.0$ s (i.e., $t = 6.5T$) for case I. Colours represent the divergence of the horizontal components of the velocity field at the free-surface and black dots indicate the positions of the tracer particles.

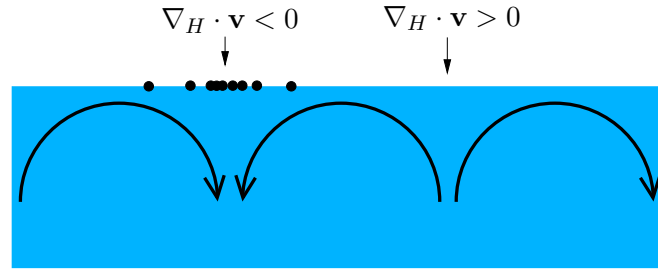


Figure 5.18 – Schematic sideview of the flow near the free surface. With black arrows the flow field underneath the surface is indicated and black dots represent passive particles. Diverging regions ($\nabla_H \cdot \mathbf{v} > 0$) are characterized by depletion of particles whereas converging regions ($\nabla_H \cdot \mathbf{v} < 0$) by a agglomeration of particles.

defined as

$$\sigma_z = \left[\frac{1}{N} \sum_{i=1}^N (z_i - \bar{z})^2 \right]^{1/2}. \quad (5.4)$$

The arithmetic mean is implied by \bar{z} and N denotes the total number of particles. This standard deviation σ_z is a measure of the vertical dispersion of the initial horizontal plane of particles. Note that z_i and \bar{z} in (5.4) are made non-dimensional with the fluid depth H . All particles are ini-

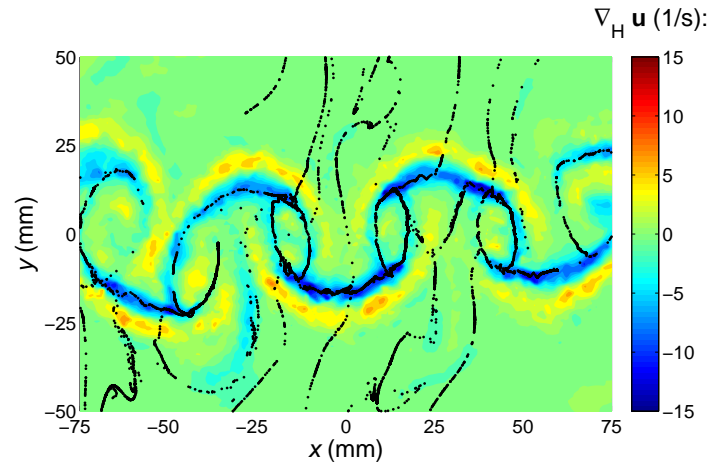


Figure 5.19 – Numerically obtained snapshot of the tracer distribution released on the free surface at $t = 12.5$ s (i.e., $t = 3.125T$) for case III. Colours represent the divergence of the horizontal components of the velocity field at the free-surface and black dots indicate the positions of the passive massless particles.

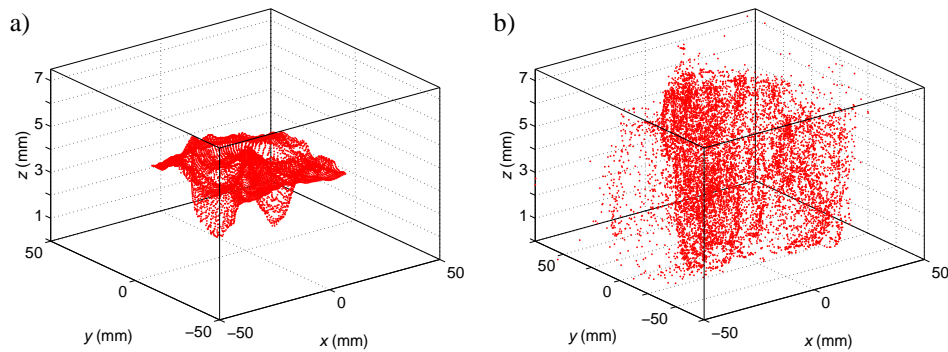


Figure 5.20 – Numerically obtained snapshots of the tracer distribution at (a) $t = 1.0$ s and (b) $t = 10.0$ s resulting from case III. The particles (indicated with red dots) are initially released on a uniform grid ($-25 \leq x \leq 25$ mm and $-25 \leq y \leq 25$ mm consisting of 10,600 particles) at mid-depth of the fluid layer, i.e., $z = 3.5$ mm.

tially at mid-depth of the fluid layer; the standard deviation is thus zero at $t = 0$. A sharp increase of σ_z is seen hereafter, indicating strong vertical displacement of these particles with respect to their initial position. It can easily be shown that randomly distributed particles (over the com-

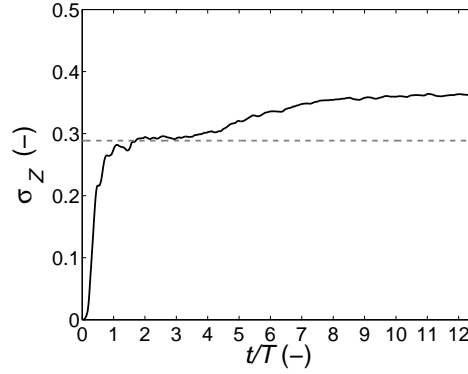


Figure 5.21 – Numerically obtained (normalised) standard deviation of the vertical particle position σ_z for case III, initially release at mid-depth of the fluid layer. Time t is made nondimensional with the forcing period T . The dashed line indicates the value of the standard deviation for a random particle distribution in the vertical direction: $\sqrt{1/12}$ (≈ 0.29).

plete fluid height) have a standard deviation value of $\sqrt{1/12}$ (≈ 0.29). Already after one forcing period, the particles have experienced such substantial vertical advection that σ_z has (approximately) an std-value of a random distribution. This value of $\sqrt{1/12}$ is even exceeded, and σ_z seems to asymptotically approach a value of approximately 0.36. At later times of the evolution, particles approach the bottom and free surface and some higher particle concentrations are observed near these boundaries (e.g., at the symmetry plane of a dipole some particles are deposited close to the bottom and surface, where w is very small), leading to higher values of σ_z than that of a random distribution. Note that an upper bound of σ_z is 0.5, corresponding to the situation that half of the particles are at the bottom and the remaining at the surface.

To investigate the influence of the 3D structures inside the shallow fluid layer on motion at the free surface, tracers advected by a purely 2D flow are also considered. This 2D simulation is similar to case III with zero thickness of the fluid layer. The Lorentz force at mid-depth of the fluid layer is used to drive the flow and a linear friction term $-\alpha \mathbf{v}$ is added in order to account for bottom friction (the value of the bottom friction coefficient α was based on the theoretical value for a fluid height of 7 mm). In a similar way as before, the particles are initially released on a uniform grid, now spanning the complete domain. In Fig. 5.22 the particle distribution obtained from

this 2D simulation is presented at $t = 18.0$ s. Clearly, the passive particle distribution is homogeneous and, during advection of the particles by this purely 2D flow, remains homogeneous for the complete time integration. This is in sharp contrast to the (surface) particles advected by the 3D flow field, where band-like structures were seen to rapidly develop (see, e.g., Fig. 5.19). The origin of this difference in particle distribution is obviously related to the divergence of the (horizontal) velocity field, which is by definition zero in the 2D case and non-zero in the 3D case. Note that in the regions of high vorticity of the 2D simulation, the particle concentration is slightly less than outside these high vorticity regions. This is due to a slight inaccuracy associated with the numerical integration of the particle paths (in rotation-dominated regions). It does not result from the flow dynamics. Figure 5.23 shows a schematic of an axisymmetric vortex, illustrated by the circular streamlines. Exact integration of a particle path should result in closed circular paths as by definition the velocity is the tangent of the streamline. Numerical integration of the velocity field yields the particle path, for simplicity here, obtained as $\mathbf{x}_{t+1} = \mathbf{x}_t + \mathbf{v}\Delta t$. In contrast to the exact integration, the new position lies on a different streamline (the radius increased), where in general the velocity is smaller when considering a vortex. After many integration steps an outward spiralling particle path thus results. This numerical inaccuracy can be minimised by decreasing the integration time steps (assuming that the spatial resolution is sufficient). It was checked that further decreasing the numerical time steps resulted in minor differences in the obtained particle paths. Note that this effect can be significant in the purely 2D flow simulations where the streamlines should be closed. In the 3D simulations this error is negligible (as compared to, e.g., $\nabla_H \cdot \mathbf{v} \neq 0$ at the surface).

Another qualitative difference between the 2D simulation and the corresponding 3D one, is the lower dissipation experienced by the flow in the 2D simulation. This is visible when comparing, e.g., the maximum vorticity of the 2D simulation is approximately 20 s^{-1} and for the 3D simulation a value of approximately 15 s^{-1} is observed. Apparently, the vertical profile of the 3D flow is more complex than that of a simple Poiseuille-like vertical structure, as was assumed with the bottom friction coefficient in the 2D simulation.

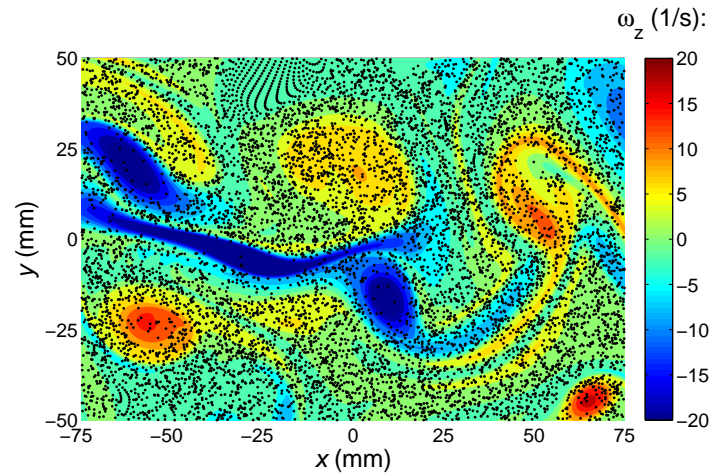


Figure 5.22 – Numerically obtained snapshot of the tracer distribution (initially released on a uniform grid) at $t = 18.0$ s for the 2D simulation. Colours represent the magnitude of the vorticity and black dots indicate the positions of the passive massless particles.

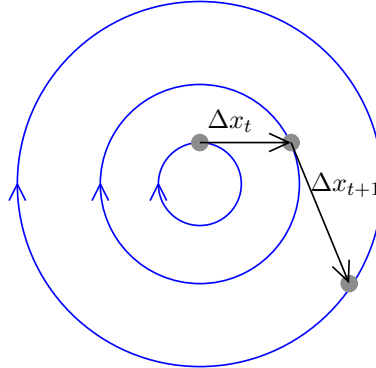


Figure 5.23 – Schematic illustration of a vortex and the outward spiralling motion as a result of a numerical inaccuracy in the particle-path integration.

5.4.3 Influence of the lateral wall; case IIIw

To investigate the influence of the lateral wall on near-wall mixing, case IIIw is now considered. Figure 5.24 shows two snapshots of the tracer distribution advected by this flow. These particles are released at $t = 0$ on a uniform grid at the surface. Already at $t = 2.0$ s, almost all particles are removed

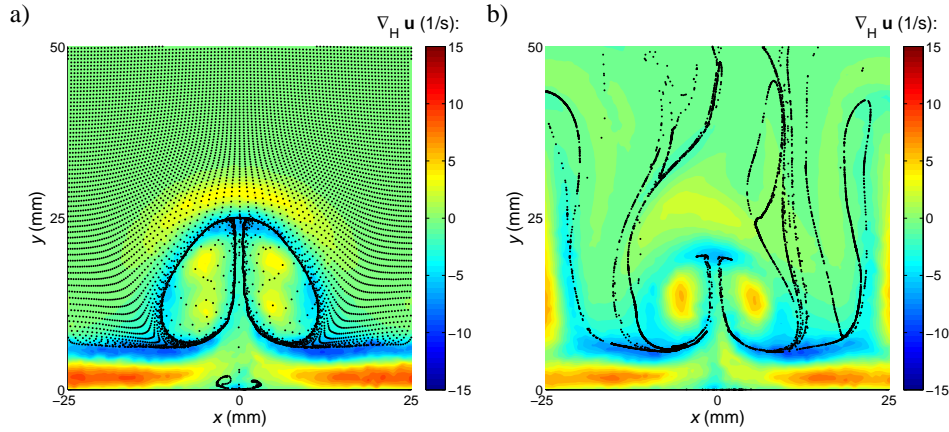


Figure 5.24 – Numerically obtained snapshots of the tracer distribution at (a) $t = 2.0$ s (i.e., $t = 0.5T$) and (b) $t = 14.0$ s (i.e., $t = 3.5T$) for case IIIw. Colours represent the divergence of the horizontal components of the velocity field at free-surface and black dots indicate the positions of the passive massless particles at the surface.

from the region near the lateral wall [see Fig. 5.24(a)] due to the locally diverging flow $\nabla_H \cdot \mathbf{v} > 0$ near the wall. This effect was already hinted at by the negative ω_x vorticity patch (near the surface) at approximately $y = 4$ mm in the snapshots of Fig. 5.12. Again, bands of enhanced particle concentrations are seen in converging regions. The two vortex patches are demarcated by closed loops of particles. Already after a few forcing periods, see Fig. 5.24(b), elongated filament-like structures where particles agglomerate can be recognised.

Figure 5.25 presents the particles distribution at (a) $t = 1.3$ s and (b) $t = 20.0$ s, initially released at mid-depth of the fluid layer. Soon after the forcing is switched on, strong vertical motions are created locally near the lateral wall. In less than one forcing period, particles close to the wall are displaced almost over the complete height of the fluid layer, whereas further away from the lateral wall the particles remain unaffected [see Fig. 5.25(a)]. This is caused by the locally strong vertical motion near the lateral wall, but also because the characteristic horizontal size of the dipole is smaller when a lateral wall is present (as explained in Sect. 5.3.3). Soon afterwards, the initial horizontal plane of particles has been advected over the complete height with enhanced particle concentrations near the bottom which coincide with the symmetry axis of the generated dipoles (i.e., at $x \approx -25$ mm,

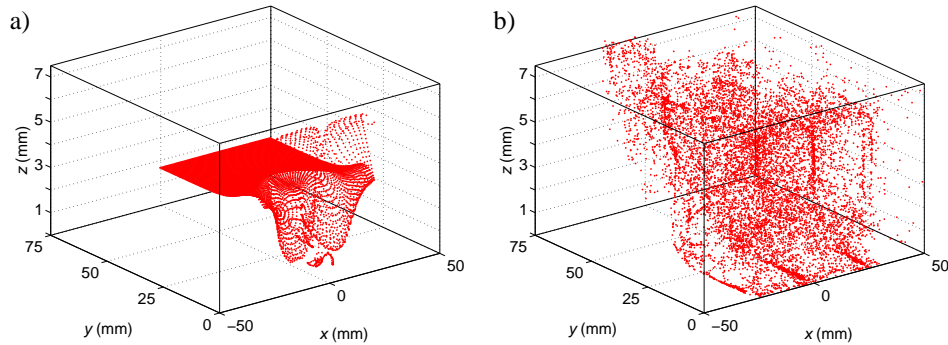


Figure 5.25 – (Colour online) Numerically obtained snapshots of the tracer distribution at (a) $t = 1.3$ s (i.e., $t = 0.325T$) and (b) $t = 20.0$ s (i.e., $t = 5T$) resulting from case IIIw. The particles (indicated with red dots) are initially released on a uniform grid ($-25 \leq x \leq 25$ mm and $0 \leq y \leq 50$ mm consisting of 10,600 particles) at mid-depth of the fluid layer, i.e., $z = 3.5$ mm.

$x = 0$, and $x \approx 25$ mm). Near the free surface, such higher concentrations are less pronounced as the magnitude of the horizontal velocity components does not approach zero there (in contrast to the situation at the bottom).

For the simulation where the lateral wall was set to a stress-free boundary condition, the particles evolution turns out to be qualitatively similar to that seen for the case of a no-slip wall, as depicted in Fig. 5.25. A quantitative difference is that the particles near the lateral wall are advected even faster in the vertical direction in the stress-free wall case (i.e., the enhanced tangential velocities near the lateral wall as opposed to a no-slip wall where the velocity goes to zero). This close similarity suggests that it is the impermeability of the lateral wall that is important in the advection of passive tracers.

As the wall affects the particle transport close to the wall, it is interesting to see what happens when particles are released close to this lateral wall. For this purpose, particles are periodically released near the wall (at $y = 0.5$ mm) at discrete timestepsⁱⁱⁱ, i.e., every 1.5 s at mid-depth of the fluid layer. In Fig. 5.26 two snapshots are presented of the particle distribution when released at the wall. Figure 5.26(a) shows a snapshot at $t = 1.5$ s, revealing a line of newly released particles at $z = 3.5$ mm, together with the particles that were released at $t = 0$. The latter particles have clearly

ⁱⁱⁱThe choice of 1.5 s was empirically determined: shorter than the forcing period of 4 s, however, not releasing the particles continuously at the same phase of the forcing.

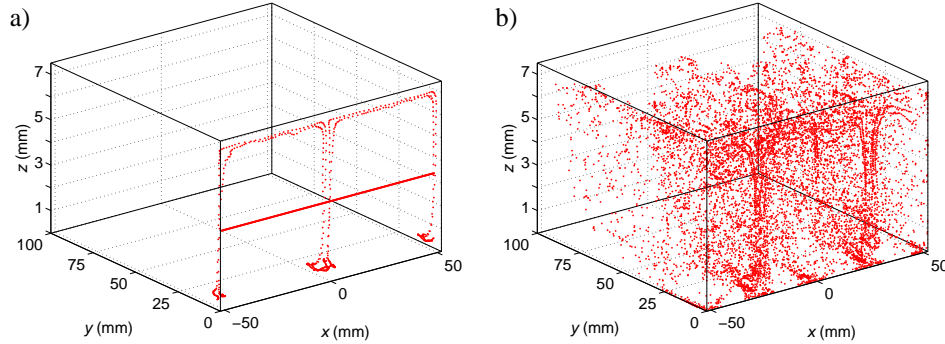


Figure 5.26 – (Colour online) Numerically obtained snapshots of the tracer distribution at (a) $t = 1.5$ s (i.e., $t = 0.375T$) and (b) $t = 20.0$ s (i.e., $t = 5T$) resulting from release of particles at the lateral wall. The particles (indicated with red dots) are released every 1.5 s at mid-depth of the fluid layer.

experienced significant advection in the vertical direction. Near the bottom and the free surface, these particles are subsequently advected away from the wall. At later times, see Fig. 5.26(b), a fairly homogeneous distribution over the fluid depth is seen together with some regions near the bottom of higher particle concentrations.

To quantify the tendency of the particles to quickly homogenise in the vertical direction, the σ_z of the particle z -locations is considered. The time evolution of σ_z for case IIIw (i.e., with the no-slip wall boundary condition) is shown graphically in Fig. 5.27(a). Qualitatively, a similar evolution is seen as for case III (cf. Fig. 5.21). However, a slightly lower increase of σ_z is seen in the initial stage for $t/T < 1.0$ as further away from the wall the particles remain at their initial position. Moreover, σ_z approximately attains its asymptotic value of 0.36 already at $t/T = 4.0$. This value, higher than the value for random vertically dispersed particle positions, results from the enhanced particle concentrations near the bottom and surface, which sets in more rapidly with a lateral wall present.

Figure 5.27(b) displays the standard deviation σ_z when the particles are released at the no-slip wall (solid line) and stress-free wall (dashed black line). Well before $t/T = 1.0$, the σ_z attains a value indicating significant vertical displacement from the initial position. Every 1.5 s a jump in σ_z is seen, resulting from a new release of particles. Furthermore, qualitatively the same evolution is seen for the no-slip wall and stress-free wall, although a slightly higher value of σ_z is attained for the stress-free wall case. This

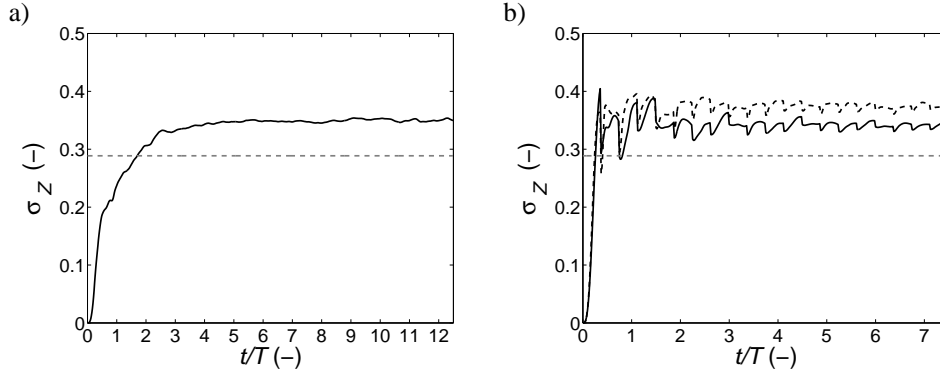


Figure 5.27 – Numerically obtained (normalised) standard deviation σ_z of the vertical particle positions of case IIIw for (a) initially released at mid-depth of the fluid layer on a horizontal plane, and (b) released very close to the lateral wall. In this second figure the dashed black line corresponds to case IIIw where the lateral wall was set to a stress-free boundary condition. Time t is made nondimensional with the forcing period T . The gray dashed line indicates the value of the standard deviation for a random particle distribution (in the vertical direction).

close resemblance confirms again that the impermeability of the lateral wall is more important rather than the no-slip condition. Comparison of Fig. 5.27(b) with 5.27(a) shows that indeed the influence of the lateral wall is limited to the region close to this wall.

In a similar way as was done for the case without wall, also 2D simulations were performed for the case with a lateral wall present. When the particles were released initially on a uniform grid, their distribution remained approximately homogeneous in time as was already seen for case III (see Fig. 5.22). For the case where the particles were released periodically near the wall (every 1.5 s), the resulting particle distribution at $t = 8.0$ s is shown in Fig. 5.28(a). The particles are stripped from the wall, advected in between the two vortices that form dipoles, and subsequently wrapped around these dipole. Hereafter, these particles are transported back towards the wall in the tails of the dipoles, i.e., the particles are approximately confined to the region $y < 3D$. Moreover, it is noticeable that the outer dipoles have started to influence the system. In the second snapshot of Fig. 5.28, the particle distribution is displayed at $t = 29.0$ s. The majority of the particles remain close to the wall. For the 3D case, it was seen that close to the wall the flow field is diverging (see Fig. 5.24) and no particles were seen in the region near the wall. Furthermore, the time-periodic response that

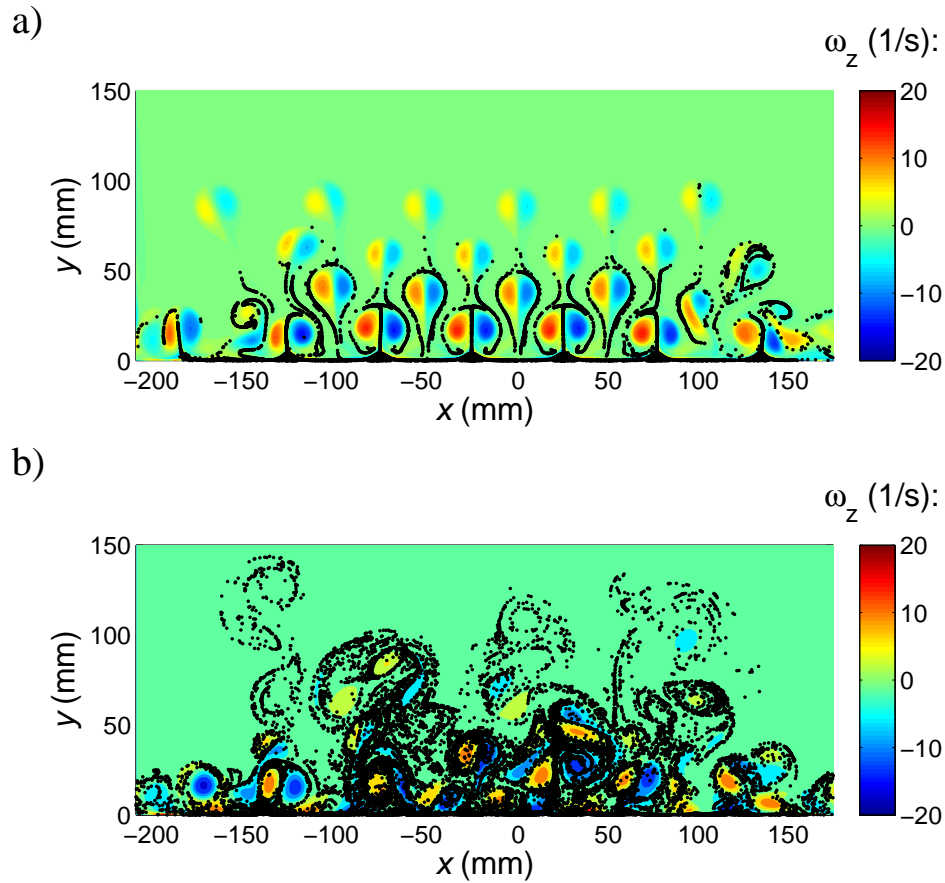


Figure 5.28 – Numerically obtained snapshot of the tracer distribution (periodically released at $y = 0.5$ mm near the lateral wall) at (a) $t = 8.0$ s (i.e., $t = 2T$) and at (b) $t = 29.0$ s (i.e., $t = 7.25T$) for the 2D simulation. For clarity, only 50% of the particles are shown in the latter snapshot. Colours represent the magnitude of the vorticity and black dots indicate the positions of the passive massless particles.

was seen for the complete 3D simulation of case IIIw is not seen in the 2D simulation. As was already noted before, the 2D simulation experience less dissipation due to the oversimplified linear friction term enabling the outer dipoles to propagate further and subsequently influence the complete flow system.

5.5 Conclusions

The 3D structure of a linear array of vortices has been investigated. Contrary to the investigation of a single dipole, now also vortex-vortex and vortex-wall interaction are present. Emphasis was put on the qualitative influence of the continuous time-varying forcing to generate the flow and the consequence of the presence of a lateral wall on the flow dynamics and dispersion properties. Specific choices were made for the parameter regime that was considered in these experiments (such as forcing protocol, magnet positions, and position of the lateral wall). Therefore, this chapter was more of an exploratory, qualitative nature.

For the weak forcing case I, the flow responded periodically to the external forcing. Due to the magnet arrangement an array of dipolar vortices was created that was chained together, and in combination with the rather low Reynolds number these dipoles did not propagate. Increasing the forcing strength resulted in an advection-dominated flow (case III) and the periodic response of the flow was broken. With a lateral wall situated on top of the magnets (case IIIw), a substantially lower Reynolds number was observed and the flow response was again periodic. As was also observed in the previous chapters, the vertical motions are very localized and can even significantly exceed the magnitude of the horizontal components (approximately a factor of two).

The development of 3D motion can be related to a vertical dependence of the horizontal flow field, as explained in chapter 3. The type of boundary conditions, vertical confinement of the flow, and vertical gradients in the forcing inevitably lead to such vertical variations in the experiments. Furthermore, the 2D flow simulations with linear friction term experienced less dissipation than the simulations of the corresponding 3D flow. The vertical profile of the 3D flow field was more complex than that of a simple Poiseuille-like vertical structure, as was assumed with the linear friction term in the 2D simulations.

The influence of the 3D motions and the presence of a lateral wall on the transport of tracers was investigated numerically. For lower Reynolds number values (case I), it was seen that, despite weak vertical motions, the tracer transport at the free surface was drastically influenced. After just a few forcing periods, approximately 90% of the particles agglomerate in the vortex cores. When the forcing strength was increased (case III), the flow was dominated by advection and the formation of elongated filament-like

structures where particles congregate was observed. This is furthermore in sharp contrast to the purely 2D case, where an approximately homogeneous distribution of particle pertains throughout the flow evolution. Releasing particles at a horizontal plane at mid-depth of the fluid revealed rapid vertical mixing of the 3D flow. Already after one forcing period the particles were almost mixed homogeneously over the full depth of the fluid layer.

Releasing particles at the free surface with a lateral wall present, resulted in patch-like regions that were depleted of particles as well as long elongated filament-like regions where particles agglomerate. Locally the wall introduces strong vertical motions, which affect the transport of particles. To illustrate this, particles were periodically released very close to the lateral wall. Well within the first forcing period, such released particles were dispersed over the complete fluid depth. Furthermore, additional numerical simulations with the lateral wall set to be stress-free were performed. The close resemblance of the particle transport with a no-slip and stress-free wall suggests that it is not the no-slip condition but rather the impermeability of this wall that is important in this rapid dispersion near the lateral wall.

CHAPTER 6

Conclusions

The work described in this thesis is part of a larger research program “Two-Dimensional Turbulence” of the “Stichting voor Fundamenteel Onderzoek der Materie (FOM)”. Within this research program specific aspects of two-dimensional (2D) turbulence were investigated, like the spectral properties of 2D turbulence [63], the influence of lateral confinement on the evolution of 2D flows [43], the three-dimensionality during dipole-wall collisions as well as the development of meandering streams in decaying quasi-2D turbulence [15]. These previous studies comprise of both numerical and experimental investigations.

The canonical laboratory setup to validate theoretical and numerical results on 2D turbulence is the shallow fluid layer setup. It is commonly assumed that the limited fluid depth restricts the flow to behave quasi-2D. However, contrary to the theory and numerical simulations on 2D turbulence, the experimental realisations are never quasi-2D but contain rather strong three-dimensional (3D) circulating flows. The causes of 3D motions and the influence of deviations from two-dimensionality in such flows remains a surprisingly much neglected issue in the relevant literature on (quasi) two-dimensional turbulence experiments.

The aim of this thesis was to investigate the influence of boundary and initial conditions on the development of 3D motion inside shallow fluid layers. This was studied by means of detailed experimental investigations on shallow fluid layers and complemented by 3D numerical simulations of the Navier-Stokes equation describing flows in such layers. The numerical sim-

ulations include a realistic modelling of the magnetic field to simulate the electromagnetic forcing.

The first experimental configuration that was considered is a dipolar vortex in a single shallow-fluid layer. A dipolar vortex was chosen as it is one of the most fundamental vortex structures in 2D turbulence and it can be conveniently created utilising electromagnetic forcing. The experimental results showed that significant and remarkably complex 3D structures and vertical motions occur throughout the flow evolution, i.e., during and after the forcing. Examples of such 3D motions are the frontal circulation structure and the oscillating up- and downward motion inside the vortex cores. The numerical simulations were shown to be in excellent agreement with the experimental results.

Based on the experimental and numerical results, several possible sources for the generation of 3D motion have been considered, e.g., surface deformations, bottom friction, and the way the flow is generated (i.e., electromagnetic forcing). Surface deformations were shown to be of minor importance in the experiments (based on the smallness of the Froude number), which was confirmed by simulations where the generation of surface deformations was excluded. Furthermore, additional simulations, with the bottom taken stress-free instead of the no-slip boundary condition, have demonstrated that the no-slip bottom is not the primary actor in generating 3D motion in a shallow layer of fluid. Lastly, the influence of the electromagnetic generation of the dipole was studied using an artificial initialisation of the numerical simulations with a columnar Lamb-like dipole structure (having a purely horizontal flow field that is divergence-free, with a Poiseuille-like vertical structure). The result showed that a thus initialised flow evolved with qualitatively similar 3D flow structures as observed in the laboratory experiments. Therefore, the observed three-dimensionality is not a result of the 3D electromagnetic forcing but rather due to the flow dynamics itself.

The development of 3D motion inside the dipole was related to a vertical dependence of the horizontal flow field. The type of boundary conditions, vertical confinement of the flow, and vertical gradients in the forcing inevitably lead to such vertical variations in experimentally realised shallow flows.

The quasi-two-dimensionality of the flow was quantified by adopting the ratio of “horizontal” to “vertical” kinetic energies, the normalized horizontal divergence, and a measure of the relaxation to a Poiseuille-like profile.

An important observation was that, although the relative magnitude of the vertical velocity as compared to the horizontal flow components decreases for decreasing fluid depth, the vertical profile of the horizontal flow relaxes rather slowly to a Poiseuille-like profile, i.e., not faster than the bottom friction time scale. Furthermore, the vertical motions are very localized in space and can even significantly exceed the magnitude of the horizontal components.

The second experimental configuration that was investigated, focused on the 3D structures of a dipolar vortex in a stable two-layer fluid setup. This two-layer configuration was believed to be a significant improvement over the single-layer setup in the sense of shielding the upper layer from the bottom, and hence suppressing any bottom friction-induced vertical motion. Remarkably, the experimental results, supported by the numerical simulations, showed to a large extent the same 3D structures and evolution as observed for the single-layer dipole. With the aid of the numerical simulations it was indirectly shown that the development of the frontal circulation is related to deformations of the internal interface, in contrast with the single-layer dipole where the development of the frontal circulation structure is directly related to the no-slip boundary condition at the bottom wall.

Indicators for quasi-2D flow behaviour, i.e., the ratio of kinetic energy contained in the vertical motion to that contained in the horizontal motion and the normalized horizontal divergence, showed a similar evolution and quantitative behaviour as that observed for the same dipolar flow in a shallow single fluid-layer. Based on the observations of the kinetic energy ratio, the two-layer configuration does not provide a significant improvement over the single-layer setup.

Dispersion characteristics in shallow flow setups have often been studied by following tracer particles at the free surface. However, such measurement configurations neglect the possible 3D flow structure and its influence on the dispersion of particles at the free surface. Therefore, passive tracer transported on the free surface of the two-layer dipole configuration was investigated. The tracer dispersion at the free surface showed the emergence of distinct narrow bands of particles, which are related to the non-zero divergence of the horizontal velocity field. As incompressible 2D flow is by definition divergence-free, such narrow bands do not develop in the purely 2D case.

The last experimental configuration that was considered was a linear

array of vortices near a lateral wall. As opposed to the previous two experimental configurations, now also dipole-dipole and dipole-wall interactions may take place. Furthermore, in this experimental configuration several continuously time-periodic forcing protocols were utilised. For the strong forcing cases, the flow was dominated by advection and dipole-dipole interactions were present whereas for weak forcing the dipoles did not propagate due to the combined effect that the dipoles are chained together and the rather low Reynolds number.

The influence of 3D motions and the presence of a lateral wall on the dispersion of particles was investigated numerically. In general, when the particles are released at the free surface they tend to agglomerate in regions where the horizontal flow field is convergent. For the weak forcing cases the majority of the particles concentrated in the vortex cores. When the forcing strength was increased, the formation of elongated filament-like structures where particles congregate was observed. This behaviour is in sharp contrast to the performed numerical simulations of purely 2D flows, which by definition are divergence-free. Releasing particles on a horizontal plane at mid-depth of the fluid revealed rapid vertical mixing due to the 3D flow. Already after one forcing period the particles were almost mixed homogeneously over the height of the fluid layer.

For the situation with a lateral wall present, enhanced vertical motions were observed near this wall. As the influence of the wall is very local, the dispersion of particles that were periodically released close to the wall was studied. Well within the first forcing period, such released particles were dispersed over the entire fluid column. Furthermore, additional numerical simulations with the lateral wall set to be stress-free were performed. The close resemblance of the particle transport with a no-slip and stress-free wall suggests that not the no-slip condition but rather the impermeability of the wall is relevant in this rapid vertical dispersion near the lateral wall.

Since the vortex dipole can be considered as a generic flow structure in 2D turbulence, the conclusions of the present study may apply more generally to experimental realizations of 2D turbulence, both for the decaying and the forced case. It is generally assumed that a shallow fluid layer behaves 2D solely based on the small aspect ratio. The results described in this thesis clearly indicate that caution is needed when interpreting such experimental realisations to validate theory and numerical simulations on 2D turbulence.

Although the shallow fluid layer configuration considered in this thesis

and geophysical flows have geometrical confinement in common as an actor in quasi-two-dimensionalising the flow, extrapolation of the results to geophysical flows is not straightforward. The large-scale dynamics of geophysical flows like the Earth's atmosphere and oceans are highly influenced by background rotation (and to a lesser extent by vertical stratification), whereas background rotation is absent in the shallow fluid configuration that was considered in this thesis. However, on smaller scales where background rotation is not dominant and also density stratification is not important, the results might contribute to our understanding of the dynamics of quasi-2D coherent structures emerging in rivers or estuarine flows. The dynamics of such large-scale structures, whose dimensions are much larger than the thickness of the fluid layer but small so that background rotation is not important, is an interesting topic for future research.

APPENDIX **A**

Experiments on linear array of vortices

This appendix contains snapshots obtained from experiments of the linear array of vortices not explicitly presented in Chapter 5. The snapshots are chosen such that some of the characteristic flow phenomena can be seen. For the experimental details the reader is referred to Sect. 5.2.

Case Iw: weak forcing with lateral wall

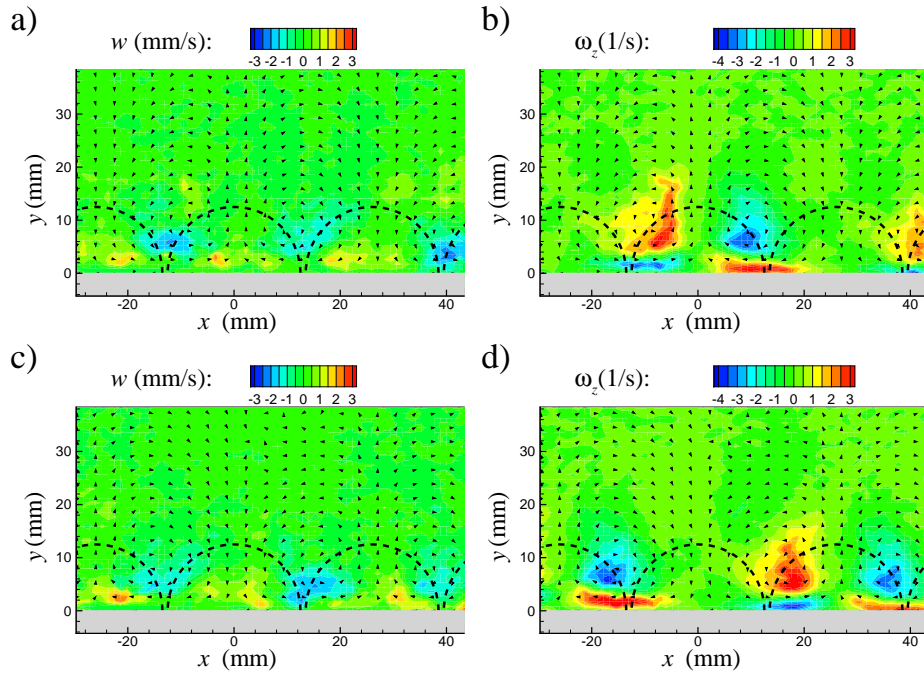


Figure A.1 – Experimentally obtained snapshots of case Iw showing (a) the vertical velocity w in colour/shades and (b) the vertical vorticity ω_z in colour/shades at $t = 26.0$ s. Vectors indicate the horizontal velocity field. The magnet locations are denoted with the dashed semi-circles. The lateral no-slip wall is located at $y = 0$. (c,d) same as (a,b) except now for $t = 28.0$ s. A quasi-periodic response is observed, with weak downward motion inside the vortex cores. At the lateral wall, oppositely signed vorticity ω_z is produced.

Case II: weak forcing with offset

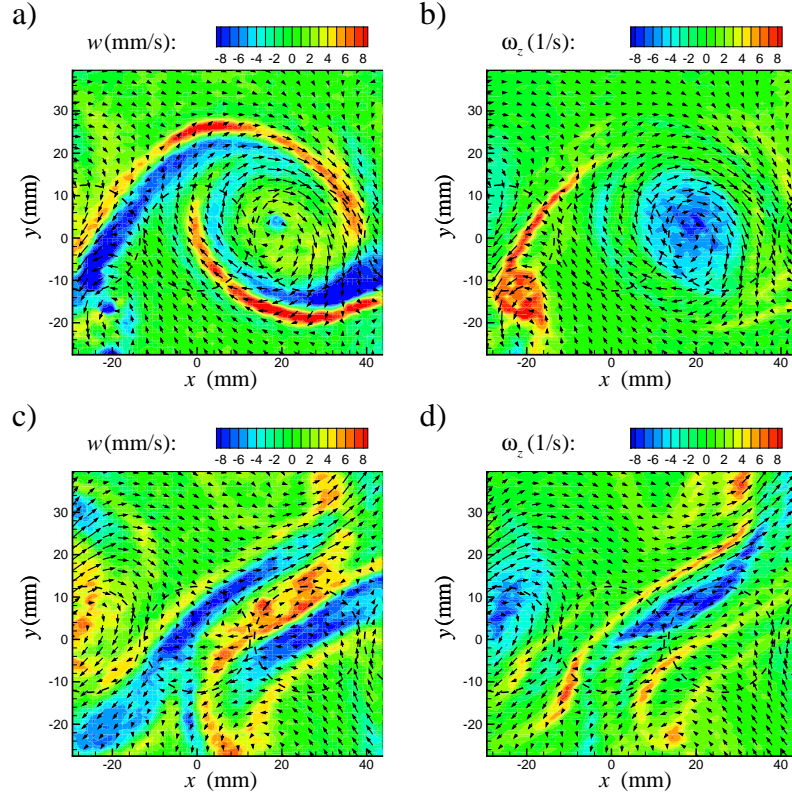


Figure A.2 – Experimentally obtained snapshots of case II. Vectors indicate the horizontal velocity field. The magnet locations are denoted with the (dashed) circles. Vertical velocity (a) and ω_z vorticity (b) in colour/shades at $t = 27.0$ s. (c) and (d) same as (a) and (b) but now for $t = 35.5$ s. As a result of the forcing offset, a mean flow is created which at approximately $t = 10.0$ s loses its time periodicity (in the field of view). Hereafter, the generation of dipolar-like structures is seen above the magnets.

Case IIw: weak forcing with offset and lateral wall

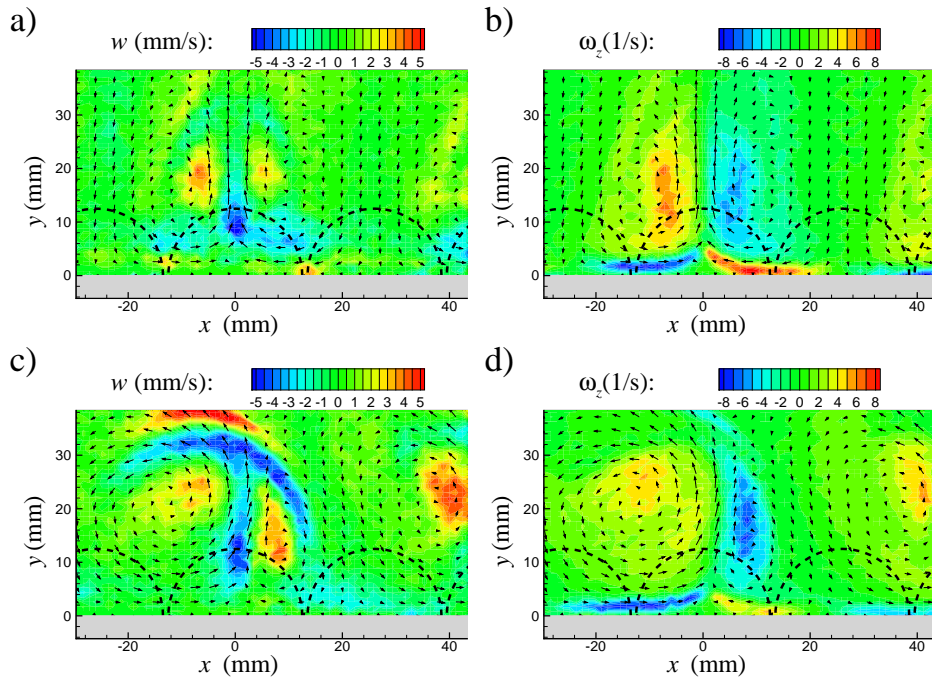


Figure A.3 – Experimentally obtained snapshots of case IIw showing (a) the vertical velocity w in colour/shades and (b) the vertical vorticity ω_z in colour/shades at $t = 10.1$ s. Vectors indicate the horizontal velocity field. The magnet locations are denoted with the dashed semi-circles. The lateral no-slip wall is located at $y = 0$. (c,d) same as (a,b) except now for $t = 26.8$ s. As a result of the forcing offset, a jet-like flow develops where, superimposed, the generation of dipoles is observed. After approximately $t = 20.0$ s slight distortions are present, which persist until the end of the measurement

Case IV: strong forcing with offset

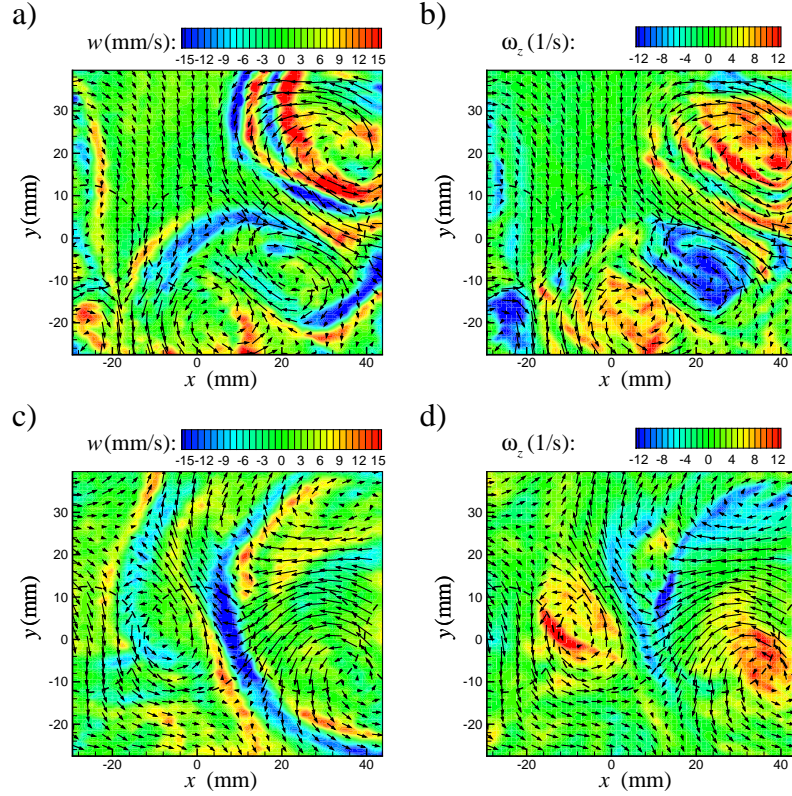


Figure A.4 – Experimentally obtained snapshots of case IV. Vectors indicate the horizontal velocity field. The magnet locations are denoted with the dashed circles. Vertical velocity (a) and ω_z vorticity (b) in colour/shades at $t = 7.0$ s. (c) and (d) same as (a) and (b) but now for $t = 32.0$ s. Already during the first forcing period, the symmetry of the flow breaks. Despite the offset on the forcing, no jet-like flow structure can be recognised. Occasionally the generation of dipolar-like vortices is observed near the magnets, as well as band-like structures being rapidly swept through the field of view.

Case IVw: strong forcing with offset and lateral wall

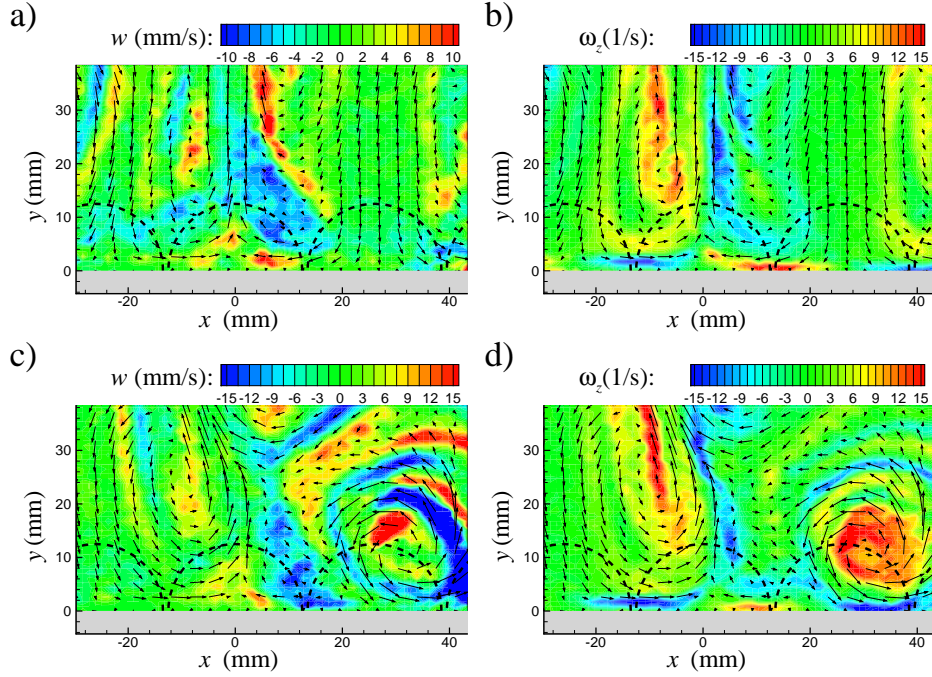


Figure A.5 – Experimentally obtained snapshots of case IVw showing (a) the vertical velocity w in colour/shades and (b) the vertical vorticity ω_z in colour/shades at $t = 6.3$ s. Vectors indicate the horizontal velocity field. The magnet locations are denoted with the dashed semi-circles. The lateral no-slip wall is located at $y = 0$. (c,d) same as (a,b) except now for $t = 34.3$ s. The formation of jet-like structures with superimposed on that dipolar structures can be recognised. Already during the second forcing period, the symmetry of the flow breaks. Hereafter, occasionally dipolar structures can be observed, that propagate away from the wall.

Bibliography

- [1] Y.D. Afanasyev. Experiments on instability of columnar vortex pairs in rotating fluid. *Geophys. Astrophys. Fluid Dyn.*, 96: 31–48, 2002.
- [2] R.A.D. Akkermans, A.R. Cieslik, L.P.J. Kamp, R.R. Trieling, H.J.H. Clercx, and G.J.F. van Heijst. The three-dimensional structure of an electromagnetically generated dipolar vortex in a shallow fluid layer. *Phys. Fluids*, 20: 116601–1–15, 2008.
- [3] R.A.D. Akkermans, L.P.J. Kamp, H.J.H. Clercx, and G.J.F. van Heijst. Intrinsic three-dimensionality in electromagnetically driven shallow flows. *Europhys. Lett.*, 83: 24001–1–6, 2008.
- [4] R.A.D. Akkermans, L.P.J. Kamp, H.J.H. Clercx, and G.J.F. van Heijst. Three-dimensional flow in electromagnetically driven two-layer fluids. *Phys. Rev. E*, (submitted, 2009).
- [5] T. Astarita and G. Cardone. Analysis of interpolation schemes for image deformation methods in PIV. *Exp. Fluids*, 38: 233–243, 2005.
- [6] U.T. Bödewadt. Die Drehströmung über festem Grunde. *Z. Angew. Math. Mech.*, 20: 241–253, 1940.
- [7] G. Boffetta. Energy and enstrophy fluxes in the double cascade of 2D turbulence. *J. Fluid Mech.*, 589: 253–260, 2007.
- [8] G. Boffetta, A. Celani, S. Musacchio, and M. Vergassola. Intermittency in two-dimensional Ekman-Navier-Stokes turbulence. *Phys. Rev. E*, 66: 026304–1–4, 2002.
- [9] G. Boffetta, A. Celani, and M. Vergassola. Inverse energy cascade in two-dimensional turbulence: Deviations from Gaussian behavior. *Phys. Rev. E*, 61: R29–R32, 2000.

-
- [10] G. Boffetta, A. Cenedese, S. Espa, and S. Musacchio. Effect of friction on 2D turbulence: An experimental study of the direct cascade. *Europhys. Lett.*, 71: 590–596, 2005.
- [11] G. Boffetta and I.M. Sokolov. Statistics of two-particle dispersion in two-dimensional turbulence. *Phys. Fluids*, 14: 3224–3232, 2002.
- [12] N.F. Bondarenko, M.Z. Gak, and F.V. Dolzhanskiy. Laboratory and theoretical models of a plane periodic flow. *Izv. Akad. Nauk. SSSR, Fiz. Atmos. Okeana*, 15: 1017–1026, 1979.
- [13] C.H. Bruneau and H. Kellay. Experiments and direct numerical simulations of two-dimensional turbulence. *Phys. Rev. E*, 71: 046305–1–5, 2005.
- [14] G.F. Carnevale, J.C. McWilliams, Y. Pomeau, J. Weiss, and W.R. Young. Evolution of vortex statistics in two-dimensional turbulence. *Phys. Rev. Lett.*, 66: 2735–2737, 1991.
- [15] A.R. Cieslik. *Three-dimensionality of shallow flows*. PhD thesis, Eindhoven University of Technology, Eindhoven (2009).
- [16] A.R. Cieslik, R.A.D. Akkermans, L.P.J. Kamp, H.J.H. Clercx, and G.J.F. van Heijst. Dipole-wall collision in a shallow fluid. *Eur. J. Mech. B/Fluids*, 28: 397–404, 2009.
- [17] A.R. Cieslik, L.P.J. Kamp, H.J.H. Clercx, and G.J.F. van Heijst. Meandering streams in a shallow fluid layer. *Europhys. Lett.*, 85: 54001–1–6, 2009.
- [18] H.J.H. Clercx and G.J.F. van Heijst. Energy spectra for decaying 2D turbulence in a bounded domain. *Phys. Rev. Lett.*, 85: 306–309, 2000.
- [19] H.J.H. Clercx and G.J.F. van Heijst. Two-dimensional Navier-Stokes turbulence in bounded domains. *App. Mech. Rev.*, 62: 020802–1–25, 2009.
- [20] H.J.H. Clercx, G.J.F. van Heijst, and M.L. Zoetewij. Quasi-two-dimensional turbulence in a shallow fluid layer: The role of bottom friction and fluid layer depth. *Phys. Rev. E*, 67: 066303–1–9, 2003.
- [21] COMSOL Multiphysics COMSOL AB. Tegnérgatan 23, SE-111 40 Stockholm, Sweden. (<http://www.comsol.com>).

-
- [22] Y. Couder. Two-dimensional grid turbulence in a thin liquid-film. *J. Physique Lett.*, 45: L353–L360, 1984.
- [23] S. Coudert and J.P. Schon. Back-projection algorithm with misalignment corrections for 2D3C stereoscopic PIV. *Meas. Sci. Technol.*, 12: 1371–1381, 2001.
- [24] S.D. Danilov, F.V. Dolzhanskii, V.A. Dovzhenko, and V.A. Krymov. An advanced investigation of interaction of allocated quasi-two-dimensional vortices. *Chaos*, 6: 297–308, 1996.
- [25] S.D. Danilov and D. Gurarie. Quasi-two-dimensional turbulence. *Usp. Fiz. Nauk*, 170: 921–968, 2000.
- [26] F.V. Dolzhanskii, V.A. Krymov, and D.Yu. Manin. An advanced experimental investigation of quasi-two-dimensional shear flows. *J. Fluid Mech.*, 241: 705–722, 1992.
- [27] F.V. Dolzhanskiy. Effect of external friction on the stability of plane-parallel flows in a homogeneous incompressible liquid. *Izv. Akad. Nauk. SSSR, Fiz. Atmos. Okeana*, 23: 262–268, 1987.
- [28] M. Duran-Matute, L.P.J. Kamp, R.R. Trieling, and G.J.F. van Heijst. Inertial oscillations in a confined monopolar vortex subjected to background rotation. *Phys. Fluids*, 21: 116602–1–13, 2009.
- [29] M. Duran-Matute, L.P.J. Kamp, R.R. Trieling, and G.J.F. van Heijst. Scaling of decaying shallow axisymmetric swirl flows. *J. Fluid Mech.*, 648: 471–484, 2010.
- [30] R. Fjørtoft. On the Changes in the Spectral Distribution of Kinetic Energy for Two-Dimensional Non-Divergent Flow. *Tellus*, 5: 225–230, 1953.
- [31] T. Fournel, S. Coudert, C. Fournier, and C. Ducottet. Stereoscopic particle image velocimetry using telecentric lenses. *Meas. Sci. Technol.*, 14: 494–499, 2003.
- [32] T. Fournel, J.M. Lavest, S. Coudert, and F. Collange. Self-calibration of PIV video cameras in Scheimpflug condition. In M. Stanislas, J. Westerweel, and J. Kompenhans, editors, *Particle Image Velocimetry: Recent Improvements*, pages 391–405, 2004.

-
- [33] U. Frisch. *Turbulence*. Cambridge University Press, 1995.
- [34] U. Frisch and P.-L. Sulem. Numerical Simulation of the Inverse Cascade in Two-Dimensional Turbulence. *Phys. Fluids*, 27: 1921–1923, 1984.
- [35] E.A. Gak and G.R. Rik. Kinetic motion of ions in aqueous solutions of strong electrolytes as influences by constant magnetic fields. *Dokl. Akad. Nauk. SSSR*, 175: 856, 1967.
- [36] H.P. Greenspan. *The Theory of Rotating Fluids*. Cambridge University Press, Cambridge, 1969.
- [37] J.D. Jackson. *Classical Electrodynamics*. Wiley, New York, 1999.
- [38] B. Jüttner, D. Marteau, P. Tabeling, and A. Thess. Numerical simulations of experiments on quasi-two-dimensional turbulence. *Phys. Rev. E*, 55: 5479–5488, 1997.
- [39] G.H. Jirka. Large scale flow structures and mixing processes in shallow flows. *J. Hydraulic Res.*, 39: 567–573, 2001.
- [40] M.-C. Jullien, P. Castiglione, and P. Tabeling. Experimental observation of Batchelor dispersion of passive tracers. *Phys. Rev. Lett.*, 85: 3636, 2000.
- [41] M.-C. Jullien, P. Castiglione, and P. Tabeling. Intermittency of a passive tracer in the inverse energy cascade. *Phys. Rev. E*, 64: 035301–1–4, 2001.
- [42] M.-C. Jullien, J. Paret, and P. Tabeling. Richardson Pair Dispersion in Two-Dimensional Turbulence. *Phys. Rev. Lett.*, 82: 2872–2875, 1999.
- [43] G.H. Keetels. *Fourier spectral computation of geometrically confined two-dimensional flows*. PhD thesis, Eindhoven University of Technology, Eindhoven (2008).
- [44] G.H. Keetels, H.J.H. Clercx, and G.J.F. van Heijst. On the origin of spin-up processes in decaying two-dimensional turbulence. *Eur. J. Mech. B/Fluids*, 29: 1–8, 2009.

-
- [45] H. Kellay and W.I. Goldburg. Two-dimensional turbulence: A review of some recent experiments. *Rep. Prog. Phys.*, 65: 845–894, 2002.
- [46] H. Kellay, X.L. Wu, and W.I. Goldburg. Experiments with turbulent soap films. *Phys. Rev. Lett.*, 74: 3975–3978, 1995.
- [47] R.N. Kieft, K.R.A.M. Schreel, G.J.A. van der Plas, and C.C.M. Rindt. The application of a 3D PTV algorithm to a mixed convection flow. *Exp. Fluids*, 33: 603–611, 2002.
- [48] B.J. Kim and H.J. Sung. A further assessment of interpolation schemes for window deformation in PIV. *Exp. Fluids*, 41: 499–511, 2006.
- [49] R.H. Kraichnan. Inertial ranges in two-dimensional turbulence. *Phys. Fluids*, 10: 1417–1423, 1967.
- [50] P.K. Kundu. *Fluid Mechanics*. Elsevier, Amsterdam, 2004.
- [51] S. Lardeau, S. Ferrari, and L. Rossi. Three-dimensional direct numerical simulation of electromagnetically driven multiscale shallow layer flows: Numerical modeling and physical properties. *Phys. Fluids*, 20: 127101–1–17, 2008.
- [52] N.J. Lawson and J. Wu. Three-dimensional particle image velocimetry: experimental error analysis of a digital angular stereoscopic system. *Meas. Sci. Technol.*, 8: 1455–1464, 1997.
- [53] D.K. Lilly. Numerical simulation of two-dimensional turbulence. *Phys. Fluids*, S2, 12: 240–249, 1969.
- [54] L.C. Lin, M. Ozgoren, and D. Rockwell. Space-time development of the onset of a shallow-water vortex. *J. Fluid Mech.*, 485: 33–66, 2003.
- [55] E. Lindborg. Can the atmospheric kinetic energy spectrum be explained by two-dimensional turbulence? *J. Fluid Mech.*, 388: 259–288, 1999.
- [56] E. Lindborg. Comment on “Turbulence-Condensate Interaction in Two Dimensions”. *Phys. Rev. Lett.*, 102: 149401, 2009.
- [57] H-G. Maas, A. Grün, and D. Papantoniou. Particle Tracking in three-dimensional turbulent flows - Part I: Photogrammetric determination of particle coordinates. *Exp. Fluids*, 15: 133–146, 1993.

-
- [58] S.R. Maassen, H.J.H. Clercx, and G.J.F. van Heijst. Decaying quasi-2D turbulence in a stratified fluid with circular boundaries. *Europhys. Lett.*, 46: 339–345, 1999.
- [59] S.R. Maassen, H.J.H. Clercx, and G.J.F. van Heijst. Self-organization of quasi-two-dimensional turbulence in stratified fluids in square and circular containers. *Phys. Fluids*, 14: 2150–2169, 2002.
- [60] D. Marteau, O. Cardoso, and P. Tabeling. Equilibrium states of 2-dimensional turbulence: An experimental study. *Phys. Rev. E*, 51: 5124–5127, 1995.
- [61] B.K. Martin, X.L. Wu, W.I. Goldburg, and M.A. Rutgers. Spectra of decaying turbulence in a soap film. *Phys. Rev. Lett.*, 80: 3964–3967, 1998.
- [62] C.D. Meinhart, S.T. Wereley, and J.G. Santiago. A PIV algorithm for estimating time-averaged velocity fields. In *Proceedings of Optical Methods and Image Processing in Fluid Flow, 3rd ASME/JSME Joint Fluids Engineering Conference*, 1999.
- [63] D. Molenaar. *Forced Navier-Stokes flows on a bounded two-dimensional domain*. PhD thesis, Eindhoven University of Technology, Eindhoven (2004).
- [64] L. Onsager. Statistical Hydrodynamics. *Nuovo Cimento*, 6: 279–287, 1949.
- [65] S. Ott and J. Mann. An experimental investigation of the relative diffusion of particle pairs in three-dimensional turbulent flow. *J. Fluid Mech.*, 422: 207–223, 2000.
- [66] J. Paret, M.-C. Jullien, and P. Tabeling. Vorticity statistics in the two-dimensional enstrophy cascade. *Phys. Rev. Lett.*, 83: 3418–3421, 1999.
- [67] J. Paret, D. Marteau, O. Paireau, and P. Tabeling. Are flows electromagnetically forced in thin stratified layers two-dimensional? *Phys. Fluids*, 9: 3102–3104, 1997.
- [68] J. Paret and P. Tabeling. Experimental observation of the two-dimensional inverse energy cascade. *Phys. Rev. Lett.*, 79: 4162–4165, 1997.

-
- [69] A.K. Prasad. Stereoscopic particle image velocimetry. *Exp. Fluids*, 29: 103–116, 2000.
- [70] A.K. Prasad and R.J. Adrian. Stereoscopic particle image velocimetry applied to liquid flows. *Exp. Fluids*, 15: 49–60, 1993.
- [71] M. Raffel, C.E. Willert, and J. Kompenhans. *Particle Image Velocimetry: a Practical Guide*. Springer, Berlin Heidelberg New York, 1998.
- [72] M. Rivera, P. Vorobieff, and R.E. Ecke. Turbulence in flowing soap films: Velocity, vorticity, and thickness fields. *Phys. Rev. Lett.*, 81: 1417–1420, 1998.
- [73] M.K. Rivera and R.E. Ecke. Pair dispersion and doubling time statistics in two-dimensional turbulence. *Phys. Rev. Lett.*, 95: 194503, 2005.
- [74] L. Rossi, S. Bocquet, S. Ferrari, J.M. Garcia de la Cruz, and S. Lardeau. Control of flow geometry using electromagnetic body forcing. *Int. J. Heat Fluid Flow*, 30: 505–513, 2009.
- [75] M. Rossi. Of vortices and vortical layers: an overview. In *Vortex Structure and Dynamics*, Lecture Notes in Physics. Springer, Berlin, 2000.
- [76] M.A. Rutgers. Forced 2D turbulence: Experimental evidence of simultaneous inverse energy and forward enstrophy cascades. *Phys. Rev. Lett.*, 81: 2244–2247, 1998.
- [77] M.P. Satijn, A.W. Cense, R. Verzicco, H.J.H. Clercx, and G.J.F. van Heijst. Three-dimensional structure and decay properties of vortices in shallow fluid layers. *Phys. Fluids*, 13: 1932–1945, 2001.
- [78] F. Scarano, L. David, M. Bsibsi, and D. Callaud. S-PIV comparative assessment: image dewarping + misalignment correction and pinhole + geometric back projection. *Exp. Fluids*, 39: 257–266, 2005.
- [79] K.R.A.M. Schreel, G.A.J. van der Plas, and R.N. Kieft. Accuracy of a 3D particle tracking velocimetry method. In *Proceedings of the 9th International Symposium on Flow Visualisation*, 2000.

-
- [80] M. G. Shats, H. Xia, and H. Punzmann. Spectral condensation of turbulence in plasmas and fluids and its role in low-to-high phase transitions in toroidal plasma. *Phys. Rev. E*, 71: 046409–1–9, 2005.
- [81] M.G. Shats, H. Xia, H. Punzmann, and G. Falkovich. Suppression of turbulence by self-generated and imposed mean flows. *Phys. Rev. Lett.*, 99: 164502–1–4, 2007.
- [82] L.M. Smith and V. Yakhot. Bose Condensation and Small-Scale Structure Generation in a Random Force Driven 2D Turbulence. *Phys. Rev. Lett.*, 71: 352–355, 1993.
- [83] S.M. Soloff, R.J. Adrian, and Z.C. Liu. Distortion compensation for generalized stereoscopic particle image velocimetry. *Meas. Sci. Technol.*, 8: 1441–1454, 1997.
- [84] J. Sommeria. Experimental study of the two-dimensional inverse energy cascade in a square box. *J. Fluid Mech.*, 170:139–168, 1986.
- [85] D. Sous, N. Bonneton, and J. Sommeria. Turbulent vortex dipoles in a shallow water layer. *Phys. Fluids*, 16: 2886–2898, 2004.
- [86] D. Sous, N. Bonneton, and J. Sommeria. Transition from deep to shallow water layer: formation of vortex dipoles. *Eur. J. Mech. B/Fluids*, 24: 19–32, 2005.
- [87] P. Tabeling. Two-dimensional turbulence: a physicist approach. *Phys. Rep.*, 362: 1–62, 2002.
- [88] P. Tabeling, S. Burkhart, O. Cardoso, and H. Willaime. Experimental study of freely decaying 2-dimensional turbulence. *Phys. Rev. Lett.*, 67: 3772–3775, 1991.
- [89] W.S.J. Uijttewaal and G.H. Jirka. Grid turbulence in shallow flows. *J. Fluid Mech.*, 489: 325–344, 2003.
- [90] H.J.H. Clercx van A.H. Nielsen. Vortex statistics for turbulence in a container with rigid boundaries. *Phys. Rev. Lett.*, 85: 752–755, 2000.
- [91] L.J.A. van Bokhoven, R.A.D. Akkermans, H.J.H. Clercx, and G.J.F. van Heijst. Triangulation based stereoscopic PIV algorithm with misalignment correction. Technical Report R-1746-D, TU/e, 2009.

-
- [92] G.J.F. van Heijst and H.J.H. Clercx. Laboratory modeling of geophysical vortices. *Annu. Rev. Fluid Mech.*, 41: 143–164, 2009.
- [93] G.J.F. van Heijst, H.J.H. Clercx, and D. Molenaar. The effects of solid boundaries on confined two-dimensional turbulence. *J. Fluid Mech.*, 554: 411–431, 2006.
- [94] G.J.F. van Heijst and R.C. Kloosterziel. Tripolar vortices in a rotating fluid. *Nature*, 338: 569–571, 1989.
- [95] H.J.H. Clercx van S.R. Maassen and G.J.F. van Heijst. Spontaneous spin-up during the decay of 2D turbulence in a square container with rigid boundaries. *Phys. Rev. Lett.*, 80: 5129–5132, 1998.
- [96] M.G. Wells and H.J.H. Clercx van G.J.F. van Heijst. Vortices in oscillating spin-up. *J. Fluid Mech.*, 573: 339–369, 2007.
- [97] J. Westerweel. Fundamentals of digital particle image velocimetry. *Meas. Sci. Technol.*, 8: 1379–1392, 1997.
- [98] J. Westerweel, D. Dabiri, and M. Gharib. The effect of a discrete window offset on the accuracy of cross-correlation analysis of digital PIV recordings. *Exp. Fluids*, 23: 20–28, 1997.
- [99] J. Westerweel and F. Scarano. Universal outlier detection for PIV data. *Exp. Fluids*, 39: 1096–1100, 2005.
- [100] J. Westerweel and J. van Oord. Stereoscopic PIV measurements in a turbulent boundary layer. In M. Stanislas, J. Kompenhans, and J. Westerweel, editors, *Particle Image Velocimetry: Progress towards Industrial Application*, pages 459–478, 2000.
- [101] B. Wieneke. Stereo-PIV using self-calibration on particle images. *Exp. Fluids*, 39: 267–280, 2005.
- [102] C. Willert. Stereoscopic digital particle image velocimetry for application in wind tunnel flows. *Meas. Sci. Technol.*, 8: 1465–1479, 1997.
- [103] H. Xia, H. Punzmann, G. Falkovich, and M.G. Shats. Turbulence-condensate interaction in two dimensions. *Phys. Rev. Lett.*, 101: 194504–1–4, 2008.

- [104] W. Zang and A.K. Prasad. Performance evaluation of a Scheimpflug stereocamera for particle image velocimetry. *Appl. Optics*, 36: 8738–8744, 1997.

Summary

3D STRUCTURES AND DISPERSION IN SHALLOW FLUID LAYERS

Many experiments have been performed in electromagnetically driven shallow fluid layers to study two-dimensional (2D) turbulence. The shallowness of the fluid layer is commonly assumed to ensure 2D dynamics. However, contrary to the theory and numerical simulations on 2D turbulence, the experimental realisations are never purely 2D. For example, laboratory setups are bounded by a no-slip bottom and stress-free surface, which implies a vertical gradient. Surprisingly, deviations from two-dimensionality in such shallow fluid setups have hardly received any attention.

The aim of this thesis was to investigate the influence of boundary and initial condition on the development of three-dimensional (3D) motion inside shallow fluid layers. For this purpose, a dipolar vortex was considered as the canonical coherent structure in the shallow fluid layer. The dipolar vortex is one of the most elementary vortex structures in 2D turbulence. Such a vortex structure can be conveniently created by electromagnetic forcing. The first two configurations that have been investigated are the dipolar vortex in a shallow one- and two-fluid layer situation. The latter (stably stratified) two-layer setup was assumed to be an improvement with respect to the single layer configuration. Finally, the following shallow-fluid layer experiment has been considered: a periodically forced linear array of vortices near a lateral wall. All measurements have been performed with Stereoscopic Particle Image Velocimetry, providing the three-component velocity field on a horizontal plane inside the fluid layer. Furthermore, all these experiments were complemented by 3D numerical simulations of the Navier-Stokes equation.

Based on the experimental and numerical results, the necessary condi-

tion for development of 3D motion in such shallow fluids was determined to be a vertical variation of the horizontal velocity field. Inside the two individual vortex cores an oscillating up- and downward motion was seen, as well as a spanwise vortex in front of the dipole. Free-surface deformations were proven to be of minor importance in generating 3D motions. Furthermore, friction exerted by the no-slip bottom and the flow initialisations were shown not to be primary actors in generating the observed complex and persistent 3D motions. Surprisingly, the 3D flow evolution of the dipole in the two-layer configuration evolved in a similar way as already seen in the single-layer setup. Contrary to statements in literature, the so-called frontal circulation was also observed in the two-layer configuration. The emergence of this structure has a different origin, however, it resulted from baroclinic vorticity production at the internal interface instead of a propagating motion over the solid bottom of the single-layer dipole. Based on the comparison of the ratio of kinetic energy (contained in the vertical and horizontal flow components) between the single- and two-layer fluid, the two-layer fluid is not an improvement over the single-layer configuration.

For the linear array of vortices, the influence of 3D motion and the presence of a lateral wall on the passive tracer transport was investigated. It was observed that particles released at the free surface form long filament-like structures related to the surface flow being convergent, in contrast with the purely 2D numerical simulations where the velocity field is by definition divergence-free and a more homogeneous particle distribution remained throughout the time evolution. Particles released at mid-depth of the fluid illustrated the efficient vertical mixing: already after one forcing period the particles were almost dispersed homogeneously over the full depth of the fluid layer. With the presence of a lateral wall this rapid vertical dispersion is even further enhanced in the near-wall region.

In summary, this thesis reveals the intrinsic three-dimensional flow behaviour of shallow fluid layers. Furthermore, experiments with a linear array of vortices illustrate the influence of the three-dimensional flow field and lateral walls on the dispersion of passive tracers. All the experimental and numerical results indicate that the interpretation of such experiments as two-dimensional realisations should be done with caution.

Samenvatting

Om tweedimensionale (2D) turbulentie te bestuderen zijn er door diverse onderzoeksgroepen experimenten verricht in horizontale, ondiepe vloeistoflagen. Hierbij wordt vaak verondersteld dat als gevolg van de geringe laagdikte de verticale snelheden veel kleiner zijn dan de horizontale snelheidscomponenten en de beweging dus hoofdzakelijk horizontaal is. Echter, in tegenstelling tot theorie en numerieke simulaties van 2D turbulentie zijn experimentele realisaties nooit exact 2D. Verrassend genoeg hebben deze afwijkingen van tweedimensionaliteit in deze laboratorium experimenten nauwelijks aandacht gekregen in de literatuur.

Het doel van dit onderzoek is het bestuderen van de invloed van rand- en beginvoorwaarden op de ontwikkeling van drie-dimensionaliteit in dunne vloeistoflagen. Hiervoor is een enkele dipolaire wervel beschouwd omdat deze één van de meest elementaire wervelstructuren vormt van 2D turbulentie. De stroming kan hierbij worden opgewekt door middel van elektromagnetische forcering: de interactie van een door de elektrolytische vloeistof lopende elektrische stroom en een magneet veld (van een permanente magneet) resulteert in een Lorentz-kracht die de vloeistof in beweging brengt. Bij toepassing van een enkele schijfvormige magneet kan men eenvoudig een dipolaire wervelstructuur genereren. Drie typen experimenten zijn uitgevoerd. De eerste twee bestaan uit een enkele dipolaire wervel in een vloeistof bestaande uit een enkele of dubbele vloeistoflaag. Van de tweelagen configuratie werd aangenomen dat deze een verbetering zou zijn ten opzichte van de configuratie met een enkele laag. Het derde experiment is een lineaire rij van wervels nabij een laterale wand. Snelheidsmetingen zijn uitgevoerd met stereoscopische Particle Image Velocimetry welke de drie snelheidscomponenten in een horizontaal vlak binnen in de vloeistoflaag kan meten. De experimenten zijn gecombineerd met driedimensionale (3D) numerieke simulaties van de Navier-Stokes vergelijking.

De noodzakelijke conditie voor het ontstaan van 3D stroming in dunne horizontale vloeistoflagen is bepaald met behulp van de experimenten en simulaties: een verticale gradiënt van het horizontale snelheidsveld. Een oscillerende op- en neergaande beweging werd waargenomen in de twee individuele wervel kernen van de dipool, alsmede een rolstructuur aan de voorzijde van de dipool. Een aantal aspecten kon worden uitgesloten als zijnde primaire oorzaken voor de ontwikkeling van drie-dimensionaliteit, te weten: deformaties van het vrije oppervlak, bodemwrijving, en initialisatie van de vloeistofstroming. De 3D structuur van de stroming in de twee-lagen vloeistof blijkt een verrassend hoge gelijkenis te vertonen met de stroming in een enkele vloeistoflaag. In tegenstelling tot observaties in de literatuur, is de rolstructuur aan de voorzijde van de dipool ook aanwezig in de twee-lagen experimenten. Echter, het ontstaan van deze structuur heeft een andere oorsprong: deze resulteert als gevolg van barocliene vorticieteitsproductie in tegenstelling tot een translerende beweging van de dipool over de bodem in de enkele vloeistoflaag. Als men de ratio van kinetische energie van de verticale en horizontale beweging beschouwt, is de twee-lagen configuratie geen verbetering ten opzichte van de enkele vloeistoflaag.

Voor de lineaire rij van wervels is de invloed van 3D stroming en de aanwezigheid van een laterale wand op het transport van passieve deeltjes onderzocht. Deeltjes losgelaten aan het vrije oppervlak vertonen de neiging om lange filament-achtige structuren te ontwikkelen als gevolg van het niet divergentie-vrij zijn van het horizontale stromingsveld aan het vrije oppervlak. Voor het zuiver 2D geval ziet men daarentegen een min of meer homogene verdeling van de deeltjes tijdens de volledige tijdsevolutie. Deeltjes losgelaten op halve hoogte in de vloeistoflaag illustreren de efficiëntie van verticale dispersie: na een forceringsperiode zijn de deeltjes over de volledige vloeistofhoogte gemengd. De aanwezigheid van een laterale wand versnelt dit mengproces in de regio nabij de wand.

Samenvattend, dit proefschrift toont de intrinsieke 3D structuur van de stroming in dunne vloeistoflagen aan. Laboratoriumexperimenten met een lineaire rij van wervels nabij de wand illustreren de invloed van drie-dimensionaliteit van de stroming en de aanwezigheid van een laterale wand op dispersie van passieve deeltjes. De laboratoriumexperimenten en numerieke simulaties geven aan dat voorzichtigheid geboden is bij de interpretatie van deze experimenten als tweedimensionale realisaties.

Promotiecommissie

Samenstelling promotiecommissie:

Prof. dr. ir. K. Kopinga	TU Eindhoven, voorzitter
Prof. dr. ir. G.J.F. van Heijst	TU Eindhoven, promotor
Prof. dr. H.J.H. Clercx	TU Eindhoven, promotor
Dr. ir. L.P.J. Kamp	TU Eindhoven, copromotor
Prof. dr. ir. W.S.J. Uijttewaal	TU Delft
Prof. dr. J.J. Rasmussen	Technical University of Denmark
Prof. dr. ir. A.A. van Steenhoven	TU Eindhoven
Prof. dr. ir. G. Ooms	TU Delft & J.M. Burgerscentrum

Dankwoord

Via deze weg wil ik een aantal mensen bedanken die direct of indirect hebben bijgedragen tot het tot stand komen van dit boekje:

Als eerste wil ik mijn promotoren GertJan van Heijst en Herman Clercx, en copromotor Leon Kamp bedanken voor hun begeleiding die uiteindelijk heeft geleid tot dit proefschrift.

Stichting FOM, TU Eindhoven en het J.M. Burgerscentrum ben ik erkentelijk voor de geboden financiële ondersteuning.

Verder wil ik Wim Uijttewaal, Jens Juul Rasmussen, Gijs Ooms, Anton van Steenhoven en Klaas Kopinga bedanken voor hun bereidheid om zitting te nemen in mijn promotiecommissie, en voor de beoordeling van mijn proefschrift.

Ad Holten voor de technische ondersteuning met betrekking tot lasers en computers, welke erg belangrijk is geweest. Met het bedanken van Ad, dank ik ook de overige technici, (oud-)collega promovendi en stafmedewerkers van de WDY groep. In het bijzonder noem ik Werner (meer dan 4 jaar mijn kamergenoot) en Laurens (voor de plezierige samenwerking die geleid heeft tot de operationele SPIV techniek). Lorenzo and Daniel for the, among others, more than 500 daily fruit breaks.

Ik dank mijn familie en vrienden voor de steun in de afgelopen jaren.

Curriculum vitae

- March 13, 1978** : Born in Etten-Leur, The Netherlands
- 1990 – 1995** : HAVO,
Katholieke Scholengemeenschap Etten-Leur
- 1995 – 1996** : HTS Werktuigbouwkunde (Propedeuse),
Hogeschool West-Brabant, Breda
- 1996 – 2004** : MSc Aerospace Engineering,
Delft University of Technology
- 2005 – 2010** : PhD candidate,
Vortex Dynamics and Turbulence,
Department of Applied Physics,
Eindhoven University of Technology
- 2010 –** : Scientific staff member,
Institute of Aerodynamics and Flow Technology,
Department of Technical Acoustics,
German Aerospace Center (DLR)

